Lappeenrannan teknillinen yliopisto

Lappeenranta University of Technology

Lasse Laurila

ANALYSIS OF TORQUE AND SPEED RIPPLE PRODUCING NON-IDEALITIES OF FREQUENCY CONVERTERS IN ELECTRIC DRIVES

Acta Universitatis
Lappeenrantaensis
188

ABSTRACT

Lasse Laurila

Analysis of torque and speed ripple producing non-idealities of frequency converters in electric drives

Electric motors driven by adjustable-frequency converters may produce periodic excitation forces that can cause torque and speed ripple. Interaction with the driven mechanical system may cause undesirable vibrations that affect the system performance and lifetime. Direct drives in sensitive applications, such as elevators or paper machines, emphasize the importance of smooth torque production.

This thesis analyses the non-idealities of frequency converters that produce speed and torque ripple in electric drives. The origin of low order harmonics in speed and torque is examined. It is shown how different current measurement error types affect the torque. As the application environment, direct torque control (DTC) method is applied to permanent magnet synchronous machines (PMSM).

A simulation model to analyse the effect of the frequency converter non-idealities on the performance of the electric drives is created. The model enables to identify potential problems causing torque vibrations and possibly damaging oscillations in electrically driven machine systems. The model is capable of coupling with separate simulation software of complex mechanical loads. Furthermore, the simulation model of the frequency converter's control algorithm can be applied to control a real frequency converter.

A commercial frequency converter with standard software, a permanent magnet axial flux synchronous motor and a DC motor as the load are used to detect the effect of current measurement errors on load torque.

A method to reduce the speed and torque ripple by compensating the current measurement errors is introduced. The method is based on analysing the amplitude of a selected harmonic component of speed as a function of time and selecting a suitable compensation alternative for the current error. The speed can be either measured or estimated, so the compensation method is applicable also for speed sensorless drives.

The proposed compensation method is tested with a laboratory drive, which consists of commercial frequency converter hardware with self-made software and a prototype PMSM. The speed and torque ripple of the test drive are reduced by applying the compensation method. In addition to the direct torque controlled PMSM drives, the compensation method can also be applied to other motor types and control methods.

ACKNOWLEDGEMENTS

Lappeenranta

10.9.2004   *Lasse Laurila*

CONTENTS

NOMENCLATURE

Letters

B	magnetic flux density
d	thickness
D	damping coefficient
e	travelling wave
e'	reflected wave
e_0	total voltage at the end of a cable
f_1	fundamental frequency
f_{sl}	slot harmonic frequency
$\boldsymbol{F}$	force
H	magnetic field strength
i_a, i_b, i_c	actual phase currents
Δi	current error
$\Delta i_a, \Delta i_b, \Delta i_c$	offset errors of phase current measurement
Δi_{AD}	quantization error
i_{am}, i_{bm}, i_{cm}	measured phase currents
$\boldsymbol{i}_s$	stator current vector
i_{sd}, i_{sq}	direct and quadrature axis components of the stator current
i_{sdm}, i_{sqm}	measured direct and quadrature axis components of the stator current
$\boldsymbol{i}_{serror}$	stator current error vector
$\boldsymbol{i}_{serror,cw}$	clockwise rotating component of stator current error vector
i_{sx}, i_{sy}	stator currents in stator reference frame
i_D, i_Q	direct and quadrature axis damper winding currents
I	current
ΔI	deviation of current
$I_{a,corr}, I_{c,corr}$	correction terms of the phase currents
I_{actual}	actual current
I_C	control current
$I_{measured}$	measured current
I_P	primary current

I_{PN}	rated primary current
I_S	secondary current
J_L	load inertia
J_M	motor inertia
k_a, k_b, k_c	gain errors of phase current measurement
k_{gain}	gain coefficient of voltage measurement
$k_{\psi corr}$	correction coefficient of the stator flux linkage estimate
K_{sh}	spring coefficient (stiffness)
l	length
L	inductance
L_{md}, L_{mq}	direct and quadrature axis magnetizing inductances
L_{sd}, L_{sq}	direct and quadrature axis stator inductances
n	number density of charge carriers, number of harmonic
N	number of samples
N_{sl}	number of slots
N_P	number of primary turns
N_S	number of secondary turns
q	number of slots per pole
q	elementary charge, $1.6021773 \cdot 10^{-19}$ C
R	resistance
R_0	closing impedance of a cable
R_H	Hall coefficient
R_M	measurement resistance
R_s	stator resistance
S_A, S_B, S_C	switching states
t	time
t_{dead}	dead-time
t_{delay}	time delay
$\boldsymbol{t}_e$	estimated electric torque
$t_{e,error}$	torque estimation error
$t_{e,errormax}$	maximum value of torque estimation error
$t_{e,ref}$	torque reference
t_{on}	turn-on time

t_{off}	turn-off time
Δt	sampling time
Δt_e	torque ripple
$T(t)$	instantaneous torque
T_{av}	average torque
T_e	motor torque
T_L	load torque
T_R	rated torque
$u_{a,loss}$, $u_{b,loss}$, $u_{c,loss}$	voltage losses due to power electronic switches
$\boldsymbol{u}_s$	stator voltage vector
u_{sA}, u_{sB}, u_{sC}	estimated stator phase voltages
u_{sd}, u_{sq}	direct and quadrature axis components of the stator voltage
U	voltage
$U_{a,dead}$	voltage error in one phase due to dead-time
U_{dead}	voltage error due to dead-time
U_C	control voltage
U_{DC}	DC-link voltage
U_{DCmeas}	measured DC-link voltage
ΔU_{DC}	total measurement error of DC-link voltage
$\Delta U_{DCoffset}$	offset voltage of the measured DC-link voltage
U_d	forward voltage drop of the freewheeling diode
U_H	Hall voltage
U_{sat}	saturation voltage drop of the switching device
$\boldsymbol{v}$	velocity
V_M	output voltage of Hall effect transducer
w	width
Z	cable impedance

Greek Letters

α	error angle
$\Delta\omega$	speed ripple
γ	angle between current vector and d-axis
θ	angle

θ_r	rotor angle
ω	angular speed
$\omega(t)$	instantaneous speed
$\hat{\omega}_n(t)$	amplitude of n:th harmonic component of speed signal
ω_{av}	average speed
ω_{est}	estimated speed
ω_{max}	maximum value of speed ripple
ω_R	rated speed
ω_0	natural resonant frequency
ω_1	electrical angular velocity of the rotor
ψ_{PM}	permanent magnet flux linkage
ψ_s	stator flux linkage
ψ_{sd}, ψ_{sq}	direct and quadrature axis stator flux linkages
ψ_{sdi}, ψ_{sqi}	stator flux linkage dq-axis components estimated in current model
$\psi_{s,\,ref}$	stator flux linkage reference
ψ_{sx}, ψ_{sy}	stator flux linkage x- and y-axis component (in stator reference frame)
$\psi_{sxi,}\, \psi_{syi}$	stator flux linkage xy-components estimated in current model
$\psi_{sxu,}\, \psi_{syu}$	stator flux linkage xy-components estimated in voltage model
$\psi_{sx,\,corr}$	stator flux linkage x-axis component correction term
$\psi_{sy,\,corr}$	stator flux linkage y-axis component correction term

Acronyms

AC	alternating current
A/D	analogue to digital
ADC	analogue-to-digital converter
AFPMSM	axial flux permanent magnet synchronous motor
As	arsenide
DC	direct current
DSP	digital signal processing
DTC	direct torque control
emf	electromotive force
FIR	finite impulse response
FOC	field orientated control

Ga	gallium
IGBT	insulated gate bipolar transistor
Im	imaginary
In	indium
LPF	low pass filter
mmf	magnetomotive force
NdFeB	neodymium iron boron
PM	permanent magnet
PMAC	permanent magnet alternating current
PMSM	permanent magnet synchronous motor
PWM	pulse width modulation
Re	real
Sb	antimony
Si	silicon
UPS	uninterruptible power supply

1   INTRODUCTION

Traditionally, torsional vibration problems have arisen in application categories where either the driven load imposes periodic or impulsive loading into the rotating system or the driving motor produces periodic or impulsive forces into the rotating system (Sheppard 1988). The development of adjustable-frequency drives has created another potential for torsional vibration problem. Motors driven by adjustable-frequency drives may produce periodic excitation forces that can cause excessive torsional vibration.

Inverter drives bring their own characteristics to mechanical systems. Feedback loop and semiconductor control create additional excitations, which are transformed through the electric actuator to the mechanical system. These combined with possible mechanical resonances may cause acoustic noise and vibration problems and thus impair the usability and the lifetime of the equipment. For example, inverters feed almost all motor drives in new paper machines, elevators and cranes. Direct drives in sensitive applications, such as elevators or paper machines, emphasize the importance of smooth torque production. In high-grade elevators the demand for low torque ripple may even be as low as 0.5 % of the rated torque, when the motor is considered.

In this thesis the main attention on torque harmonics is on the harmonic components appearing at low frequencies. These harmonics can be harmful if their frequencies lie at natural frequencies of the mechanical system consisting of a motor, a shaft, couplings and load. Because of the high inertia of the load, high frequencies are assumed negligible.

The aim of this thesis is to study and clarify the torsional vibrations caused by a frequency converter in electrically driven machine systems. Being a part of a larger project - divided into several parts, this work has its main focus on the inverter part of the system, whereas a minor emphasis is put on the motor and the mechanical load. Previously, the vibration model of the motor part has been published in (Kurronen 2003).

The significance of the different vibration sources of the frequency converter on the entire system is to be found. Another goal is to find possible compensation methods for the vibrations caused by the frequency converter. From the industrial point of view, during the project, the

interest was to find reasons for the first ten harmonics of torque empirically observed in industrial applications.

Simulation is an effective tool in the design and troubleshooting of electrically driven machine systems. The simulations enable one to identify potential problems that cause torque vibrations and possibly damaging oscillations in electrically driven machine systems. Another benefit is that the reasons for existing vibrations in such multidisciplinary system can be found by simulating the system with different non-idealities of the system parts.

The main objective in the simulation part of this work is to propose a simulation model of the electric drive that uses existing software on the market, is simple, computationally fast, easily configurable, reasonably accurate and allows investigation with wide variation of system parameters. In this work, initially, a simulation model of the frequency converter was developed to be coupled with simulation software of the mechanical load. The simulation model of the frequency converter takes into account some non-idealities of the frequency converter and the interaction of these with the load is studied. Furthermore, the simulation model of the frequency converter control was applied to a real frequency converter.

Experimentally, two setups were used to verify the effects of different vibration sources. Firstly, a commercial frequency converter with standard software, a permanent magnet axial flux synchronous motor and a DC motor as the load were used to research the effect of current measurement errors on load torque. Secondly, the feasibility of a proposed stator current measurement error compensation method was verified experimentally with the second setup consisting of another commercial frequency converter with self-made control algorithm, a permanent magnet synchronous motor and a DC motor as the load.

1.1   Importance of smooth torque and speed production

Smooth or rippleless torque and speed are important factors in many different applications of electrically driven machine systems. The harmful effects of torsional vibrations can be classified as: 1) excessive wear and even damage to the system, 2) interruption of production, 3) reduction of the process quality and 4) increased acoustic noise.

Torsional excitations are required to produce damaging oscillations. These excitations may be of an impulsive or periodic nature and may occur on a transient or steady state operation. The amount of component damage is cumulative with each oscillation or stress cycle (Sheppard 1988). Torsion analysis is recommended for adjustable speed electrical power drive systems, especially in cases where risk of resonance exists between the inertia of the motor and the inertia of the driven equipment. If, for example, within the electromagnetic torque (air gap torque) of a motor, any frequency components below 100 Hz can be expected to exceed 1 % of the nominal torque in a steady state or during start-up, the risk of resonance is significant. (IEC 61800-4:2002.)

In some industrial applications, such as the rolling mill drive systems, the mechanical part of the drive has a very low natural resonance frequency because of the large roll inertia and the long shaft. The shaft length may be over 10 m in some large systems including the gearbox and the spindle. The motor speed and the load speed can be very different in a transient state, which is often initiated by an abrupt change of the reference and/or the load. Due to the speed difference the shaft is excited in a torsional vibration with the shaft carrying high peak torque. Continuously varying stresses in the shaft can cause fatigue phenomena of the shaft material, which may result in a disastrous accident. This torsional vibration has a neqative influence on the quality of the rolled material and the stability of the drive system (Ji 1995). In machine tool applications torque ripple leaves visible patterns in high-precision machined surfaces (Holtz 1996). In air handling units torsional resonance may cause fatigue failures of wheel-shaft-rotor assemblies (Zeng 2001).

In servo drives the accuracy and repeatability of the position servo performance is deteriorated due to torque vibrations. In applications, such as the position control of a robot and the speed control of a conveyor belt, torque pulsations are highly undesirable and must be eliminated. Since the direct drive motor without a reduction gear has to operate at low speeds, the effect of torque pulsation becomes particularly undesirable. (Cho 1994.)

In paper machines continuous production and the quality of the paper are important factors. This requires accurate speed control. One manufacturer guarantees that for induction machines the static speed accuracy is better than ± 0.01 % of the maximum speed, when a tachometer is used. Without the tachometer, the guaranteed static speed accuracy is 10 % of the slip, which

typically corresponds to ± 0.1 % of the maximum speed of a medium-sized motor. A typical dynamic accuracy is ± 0.1 % of the maximum speed with some specified restrictions on the supply voltage and frequency fluctuation, load torque, resonance frequency and load inertia. (Tiainen 2003.) According to IEC 61800-4 standard the deviation band under steady state conditions can not be used to specify items which are not related with the steady state control performance (for example torque pulsation or the speed ripple caused by load torque or motor torque pulsation) (IEC 61800-4:2002).

From the end user's point of view, rippleless torque and speed can be seen as quality factors. For example, in elevators, a vibration-free elevator is sensed as riding comfort. The vertical vibration of a lift car is an important topic, because the riding comfort of passenger mainly depends on it. In addition to the elevator mechanical part, the driving motor acts as the vibration source of the lift car. Voltage and current harmonics in the motor supply produce the torque ripple of the motor torque. If the elevator mechanical system has a low resonant frequency and the motor speed control has a low bandwidth for passenger comfort, this phenomenon is more serious (Choi 2000). The elimination of the motor torque ripple is essential for the riding quality. The vibration of the lift car is also a source of acoustic noise. As with the elevators, quietness and smoothness are required also for propulsion and vehicle motors.

1.2   Permanent magnet motors in different applications

Permanent magnet synchronous motors (PMSM) offer efficiency advantages over induction machines when employed in variable speed drives. Since much of the excitation in the PMSM is provided by the magnets, the PMSM will have smaller losses associated with the magnetizing component of the stator current. The stator current may be almost purely torque producing in a PMSM drive while in an induction machine drive there is always a large magnetisation current present. Due to the synchronous operation of the PMSM, rotor losses are greatly reduced. The application of the PMSMs for low speed operation in direct drives is an economic alternative for the induction motors with gearboxes. Since the speed of the direct drive PMSMs is lower than the speed of the induction motors with the gearboxes, the risk of torque harmonics appearing at the mechanical resonances is increased in the speed range of normal operation.

Permanent magnet motors have been used for decades in low-power applications such as servo drives and domestic appliances. Recently, the PMSM drives have been developed further and are used in industrial applications requiring high torque at low speed. PMSM drives are replacing standard induction motors with gearboxes in, for example, paper industry. From the industrial point of view, the driving forces of technological development in electrical machines suit well for the permanent magnet motors. Increasing demand for wind power generators, special motors for marine, traction and offshore has created new growing markets for electrical machines. In these applications permanent magnet motors can offer a lot of advantages in comparison with conventional motors. Permanent magnet motors respond well to future customer values (environmental values, performance and operational values, new applications), because of their high efficiency, high power density, reliability, new materials etc. (Waltzer 2002.)

The permanent magnets are made of neodymium iron boron (NdFeB). Standard induction motors, designed to run at 750-3000 rpm, are not particularly well suited for low speed operation. Normally gearboxes are used to reduce the speed from, for example, 1500 rpm to 600 rpm, as in Fig. 1.1 a). A gearbox takes up space and needs maintenance as well as considerable quantities of oil. Eliminating the gearbox saves space and installation costs, as only one piece of foundation for the driving machinery is needed, Fig. 1.1 b). The length and weight of the drive can be reduced from 3500mm/2500 kg to 1040 mm/860 kg. (Ikäheimo 2002.)

a)

b)
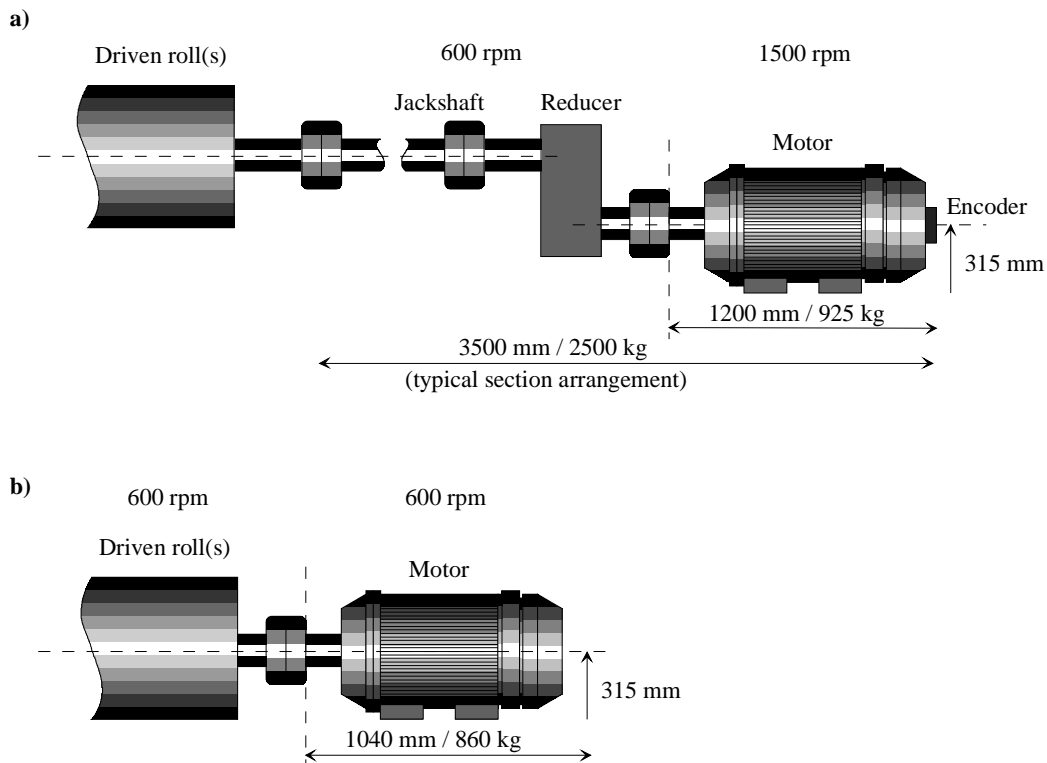
Figure 1.1 The interface of motor and driven roll. a) Conventional drive and b) gearless PMSM drive
(Waltzer 2002).

Another advantage with eliminating gearboxes is the improved efficiency of the drive. Gear-boxes usually have a rated efficiency. The power out of a gearbox is not equal to the power put into it. Considering that power is made up of speed by torque, one of the two must lost. With the meshing of the gears it is not possible to lose speed, so the efficiency rating of a gearbox relates to torque. Dynamic friction causes loss of torque while gears are turning and static friction causes loss of torque at all times. The inertia of gears causes loss of some torque during acceleration. With gearboxes some position may be lost if there exists backlash in the gears, that is, the gears do not mesh perfectly. Friction and backlash between gears may vary, if there is any eccentricity between the gears, which can also lead to vibration problems.

In addition to the above-mentioned permanent magnet synchronous radial motor, another type of permanent magnet motor is well replacing conventional motor drives. Axial flux permanent magnet synchronous motors (AFPMSM) are used in applications where only small space is available for the motor, such as in elevators. Again, a gearless AFPMSM drive of 95 rpm re-places a conventional solution using a 1500-rpm induction motor.

1.3 Definition of torque ripple

The basic task of an electric motor is to generate the torque needed to accelerate and drive a load over a specific range of speed. In steady state, the appropriate torque needed to keep the motor running at constant speed is called the average torque. However, due to the non-idealities of the electric motor, supply current and mechanical load, this torque may contain harmonics. When a PMSM is rotating at a given speed, torque components superimposed on the average torque are called torque ripple. Various methods to define the size of torque ripple are presented in (Cai 2000). The normalized instantaneous torque ripple T_{ripple} is defined here as

$$T_{\text{ripple}} = \frac{T(t) - T_{\text{av}}}{T_{\text{R}}},$$

(1.1)

where $T(t)$ is the instantaneous torque, T_{av} is the average torque and T_{R} is the rated torque. Torsional vibration is the periodic speed oscillation of the rotating system components. The speed oscillation may be defined by the normalized speed ripple, which is defined in the similar way as the torque ripple as

$$\omega_{\text{ripple}} = \frac{\omega(t) - \omega_{\text{av}}}{\omega_{\text{R}}},$$

(1.2)

where $\omega(t)$ is the instantaneous speed, ω_{av} is the average speed and ω_{R} is the rated speed.

1.4 Generation of torque ripple due to the components of an electric drive – a review

The origins of the torque ripple in electrically driven machine systems can be separated into three components: motor, frequency converter and mechanical load. These three components are reviewed briefly in this chapter as an introduction to the vibration sources in electrically driven machine systems. An in-depth analysis of the frequency converter as a vibration source follows in the later chapters, starting from the chapter 2.

1.4.1 Motor (PMSM)

In permanent magnet motors a torque ripple may be present, causing negative effects such as vibrations, noise, positioning errors and non-uniform movement at low speed. Careful design of

the permanent magnets, rotor and stator magnetic circuit geometry is needed, but still it is difficult to reach absolutely ripple-less torque. Sophisticated motor design typically produces torque ripple in the range of 0.5 % of the rated torque in permanent magnet machines with small number of slots per pole and phase (Kurronen 2003). Contributions to the torque ripple are briefly discussed in the following.

Mutual torque

Mutual torque includes the main torque and the harmonic torques, which are produced by interactions between the PM field and the armature fields due to phase currents (Cai 2000). This is the dominant torque production mechanism in most permanent magnet synchronous motors.

Reluctance torque

The interaction of the current magnetomotive forces with the angular variation in the rotor magnetic reluctance results in reluctance torque (Jahns 1996). The reluctance torque is produced by the self-inductance variation of the phase windings when the magnetic circuits of direct- and quadrature axes are unbalanced. This is inherent for salient pole rotors or interior mounting magnets (Cai 2000). PMSMs with surface magnets generate almost no reluctance torque.

Cogging torque

The rotor has the tendency to align with the stator at positions where the permeance of the magnetic circuit is locally maximized (Borghi 1998). The interaction of the rotor magnetic flux and angular variation in the stator magnetic reluctance generate pulsating torque components. Stator excitation is not involved in cogging torque production (Jahns 1996). Cogging may not be totally eliminated in machines using stator slots. Slot-less machines need air-gap windings and the magnetic air-gap becomes long causing low air-gap flux density and may thus usually be used only in high-speed machines.

Residual torque pulsations occur at a slot harmonic frequency

$$f_{sl} = \omega N_{sl} \ ,$$
(1.3)

which increases as the mechanical speed ω increases. N_{sl} is the number of slots. (Holtz 1996.)

Rotor eccentricity

Rotor eccentricity is always present and creates some adverse phenomena – such as circulating currents in the rotor. In permanent magnet synchronous machines, however, the rotor eccentricity is not as difficult a phenomenon as in, e.g., in induction machines where the air-gap is short.

System Asymmetries

Parameters of a three-phase machine differ from phase to phase, because of the design and construction of the windings. If, for example, the stator resistance differs in one phase from the resistance of the two other phases, the amplitudes of the stator currents are not equal.

Reduction of torque ripple by motor design

To achieve smooth torque production, proper motor design is required to approach ideal characteristics of a motor. Generally, the stator mmf-harmonics may be minimised by increasing the number of slots per pole q. Using short pitch windings is also advantageous. The overall minimum for stator harmonics is reached by selecting the relative width of the coil span as 5/6 of the pole pitch. Unfortunately, q must be larger than unity to be able to use short pitch windings. Often, in low-speed direct drive PMSMs there is no room for large values of q. The cogging may be minimised by selecting the permanent magnet shape and width correctly. Skewing also dampens the cogging effects as well as the stator mmf harmonics created torque ripples because it reduces the variation of reluctance seen by the rotor magnets and hence the cogging torque.

1.4.2   Converter

Frequency converters used in variable-frequency controllers produce three-phase voltages or currents that are not purely sinusoidal and contain higher frequency components that are harmonics of the fundamental frequency. The presence of time-harmonics in the stator excitation results in a pulsating torque component (Mohan 1995). Perturbations induced by power electronic devices, non-ideal measurement systems and digital controllers can create additional excitations, which are transformed through the electric actuator to the mechanism.

1.4.3   Mechanical load

Gears, shafts, eccentricities, blades, bearings, couplings, different misalignments etc. create mechanical vibration in the systems. The popular cardan-shaft creates speed vibrations even if a

slightest misalignment is present in the installation (Sopanen 2003). Even in cases of correct installation the cardan creates torque vibration due to the centre-shaft speed oscillation.

The general differential equation of rotating motion may be given as

$$T_e = J\frac{d\omega}{dt} + D\omega + T_L,$$ (1.4)

where T_e is the motor torque, J is the inertia of the system, ω is the angular speed, D is the damping coefficient due to friction and T_L is the load torque. This equation may be used in cases of rigid systems. Torsional vibrations, however, occur in the so-called two-mass system, which is the simplest method of describing oscillatory mechanics.

Torsional vibration involves the transfer of power between two or more connected rotating masses. A simple system is comprised of the motor, coupling and the load. Fig. 1.2 introduces a two-mass model, where two rotating masses are connected by a shaft. The inertias of the two masses and the torsional spring constant of the connecting shaft have a natural frequency of vibration at which the two masses tend to oscillate in opposition to one another (Merril 1994a). The equivalent block diagram is shown in Fig. 1.3.
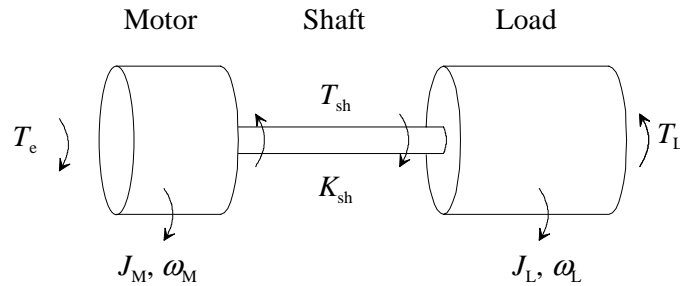

Figure 1.2   Two-mass model of a mechanical system. T_e is the motor torque, J_M is the motor inertia, ω_M is the motor angular speed, T_{sh} is the shaft torque, K_{sh} is the spring coefficient (stiffness), J_L is the load inertia, ω_L is the load speed and T_L is the load torque (Ji 1995).
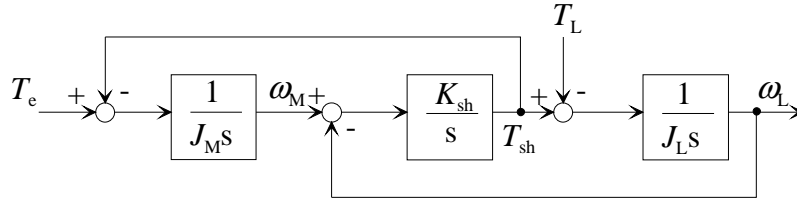
Figure 1.3 Block diagram of the two-mass model (Ji 1995). The dynamic equations of the two-mass model are given in Appendix A.

The natural resonant frequency of the system is

$$\omega_0 = \sqrt{K_{sh}\left(\frac{1}{J_M} + \frac{1}{J_L}\right)}. \tag{1.5}$$

The natural frequencies are constant, but the excitations change with motor-inverter speed. When the exciting frequency approaches the natural frequency of the system, the risk of torsional resonance appears. In that situation resonance amplification will occur and system damage may result, if the torsional excitation can feed energy into the vibration mode. Resonance amplifies the magnitude of the oscillation and the resulting stresses. Shaft stresses are shear stresses, when transmitting torque between rotating elements. On large machines, resonant stresses may exceed the endurance limit of the shaft material, resulting in finite shaft life in fatigue (Merril 1994b). In Finnish paper machine industry oscillating torques have broken several cardans driving large paper machine cylinders (Erkkilä 2002).

Eq. (1.5) indicates that large systems, which have large inertias, generally produce low natural frequencies. Smaller systems, which have relatively small inertias and stiff components, generally produce higher natural frequencies.

Other system excitations may be produced by mechanical components. Coupling misalignment and lateral vibration will produce torsional excitations. The magnitudes are generally small but will also occur at multiples of shaft speed. (Sheppard 1988.)

A rolling mill drive example

At no load situation the motor and the roll rotate at the same speed, Fig. 1.4 a). Application of a load torque to the roll first slows down the speed of the roll. If the spindle is perfectly rigid, the

motor speed also slows down at the same rate simultaneously. In this situation no torsion occurs.

a) No load.   b) Application of a load.
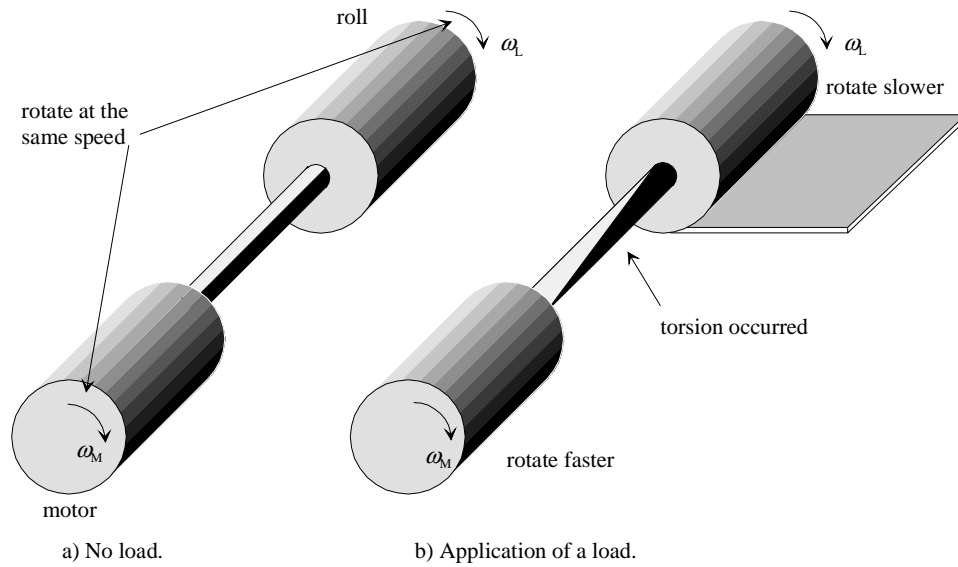
Figure 1.4 Torsion on the shaft of a rolling mill.

Short spindles, i.e. those with lengths comparable to their diameters, cause little problem of the torsional vibration. Longer spindles, as compared with their diameter have a resilient property and a rather low resonant frequency and can cause the drive train to exhibit oscillatory behaviour. The flexibility of the spindle retards the travel of torque along the spindle to the motor. The motor speed, therefore, remains constant immediately after the load torque application and deviates from the roll speed. A difference in their speeds results and causes torsion on the spindle, Fig. 1.4 b). Once the spindle is distorted, vibration results due to the "spring property" of the spindle and lasts a long time. (Naitoh 1996.)

1.5   Permanent magnet synchronous machine model

The stator of a permanent magnet synchronous machine has a conventional three-phase winding, and the rotor can have magnets mounted on the surface of the rotor, or there can be magnets buried inside the rotor (interior magnets). The two-axis form of stator voltage equations in rotor reference frame for an ideal synchronous machine are

$$u_{sd} = R_s i_{sd} + \frac{d\psi_{sd}}{dt} - \omega_1 \psi_{sq}, \tag{1.6}$$

$$u_{sq} = R_s i_{sq} + \frac{d\psi_{sq}}{dt} + \omega_1 \psi_{sd}, \tag{1.7}$$

where u_{sd} and u_{sq} are the direct and quadrature axis components of the stator voltage, R_s is the stator resistance, i_{sd} and i_{sq} are the direct and quadrature axis components of the stator current, ψ_{sd} and ψ_{sq} are the direct and quadrature axis components of the stator flux linkage and ω_1 is the electrical angular velocity of the rotor (Vas 1992). The stator flux linkage rotor co-ordinate components are

$$\psi_{sd} = L_{sd} i_{sd} + \psi_{PM}, \tag{1.8}$$

$$\psi_{sq} = L_{sq} i_{sq}, \tag{1.9}$$

where L_{sd} and L_{sq} are direct and quadrature axis stator inductances and ψ_{PM} is the constant flux linkage produced by the permanent magnets. The stator and rotor reference frames are illustrated in Appendix B.

When buried magnets are used, $L_{sd} \neq L_{sq}$, and the electromagnetic torque also contains a reluctance torque. In the absence of damper windings, the electromagnetic torque produced in the PMSM with interior magnets is

$$t_e = \frac{3}{2} p \left[\psi_{PM} i_{sq} + \left(L_{sd} - L_{sq} \right) i_{sd} i_{sq} \right], \tag{1.10}$$

where p is the number of the pole-pairs (Vas 1998). The term $(L_{sd} - L_{sq}) i_{sd} i_{sq}$ is due to the saliency of the rotor. This is the reluctance torque. When the saliency $L_{sd} - L_{sq}$ is large, it may be a good idea to use a nonzero i_{sd} in order to maximize the torque production for a given stator current modulus by utilizing the reluctance torque (Harnefors 1998).

With surface-mounted magnets, $L_{sd} = L_{sq}$, and equation (1.10) is simplified to

$$t_e = \frac{3}{2} p \psi_{PM} i_{sq}. \tag{1.11}$$

Torque is then produced by the quadrature axis current i_{sq}. The desired electromagnetic torque is achieved with minimum stator current when $i_{sd} = 0$. Using only the quadrature component of the stator current results easily in a low $\cos\varphi_1$ for the drive depending on the value of magnetizing inductance L_{mq}.

1.6 Functional principle of the DTC

In this thesis the direct torque control (DTC) is used as the control method both in simulations and laboratory tests and thus the operating principle of the DTC is described briefly. In principle the DTC is a hysteresis control of the stator flux linkage and the torque that directly selects one of the six non-zero and two zero discrete voltage vectors of the inverter. The principal operation of the DTC is shown as a block diagram in Fig. 1.5.
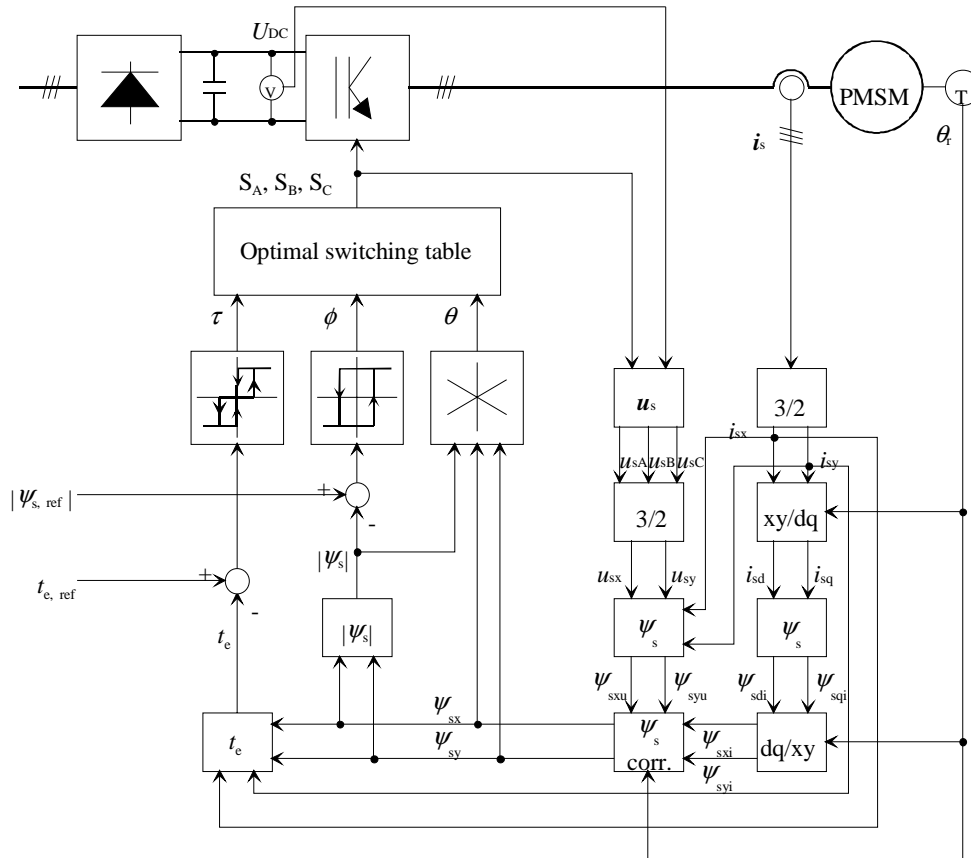

Figure 1.5   The principal operation of the direct torque control (Luukko 1998). The rotor angle measurement is included in the figure, although it could also be estimated.

1.6.1 Voltage model

The stator flux linkage vector $\boldsymbol{\psi}_s$ is estimated on every control cycle (25 μs) as

$$\boldsymbol{\psi}_s = \int \left(\boldsymbol{u}_s - \boldsymbol{i}_s R_s \right) \mathrm{d}t \, , \tag{1.12}$$

where $\boldsymbol{u}_s$ is the estimated stator voltage vector, $\boldsymbol{i}_s$ is the measured stator current vector and R_s is the stator resistance (Vas 1998; Luukko 1998). The voltage model is suitable for fast transients, but at very slow speeds some additional correction is needed to adjust the flux linkage estimation. The determination of $\boldsymbol{i}_s$ in stator co-ordinates is presented in Appendix B. The instantaneous estimated electric torque $\boldsymbol{t}_e$ of the machine is

$$\boldsymbol{t}_e = \frac{3}{2} p \boldsymbol{\psi}_s \times \boldsymbol{i}_s \, . \tag{1.13}$$

The estimated instantaneous electric torque is easily compared with a reference value to achieve a fast torque control. At the same time, the stator flux linkage is compared with the reference value to ensure sufficient magnetization of the motor.

In conventional DTC, the torque comparator is used to select whether the inverter output voltage vector should be a torque-increasing vector or a torque-reducing vector. The appropriate vector is then applied for the duration of the sampling period. At low speed the torque increasing vectors are very effective at increasing the torque, whereas the torque reducing vectors are less effective. In contrast, at high rotor speeds, the torque-increasing vectors are less effective, whereas the torque reducing vectors are more effective. The result of this is that, at low speed, the torque tends to make a considerable excursion above the maximum torque hysteresis limit. At high speed the torque tends to make a considerable excursion below the minimum torque hysteresis limit. (Bird 1997.)

1.6.2 Current model

In addition to the stator flux linkage estimation by (1.12), a better control is achieved if an additional flux linkage correction is applied. One possible method is to calculate the stator flux linkage by using the measured phase currents and the inductances, which are a priori knowledge. In the rotor reference frame the direct and quadrature axis components of the flux linkage are

$$\psi_{\text{sd}} = L_{\text{sd}} i_{\text{sd}} + L_{\text{md}} i_{\text{D}} + \psi_{\text{PM}} \qquad (1.14)$$

and

$$\psi_{\text{sq}} = L_{\text{sq}} i_{\text{sq}} + L_{\text{mq}} i_{\text{Q}} , \qquad (1.15)$$

where L_{sd} and L_{sq} are the direct and quadrature axis stator inductances, L_{md} and L_{mq} are the direct and quadrature axis magnetizing inductances, i_{D} and i_{Q} are the dirext and quadrature axis damper winding currents and ψ_{PM} is the flux linkage of the permanent magnets.

One drawback of the current model is that the rotor angle θ_{r} is needed because of the coordinate transformation from stator to rotor reference frame. Another drawback is the change of inductance values during transients, which causes an error during the transients. Also the estimation of the damper winding currents i_{D} and i_{Q} reduces the accuracy of the current model during transients. In steady state the current model is valid and it is used to prevent the stator flux linkage from drifting during a long time period.

1.6.3 Stator flux linkage estimation problems

The performance of the DTC drive using equation (1.12) depends on the accuracy of the estimated stator flux linkage, and these depend on the accuracy of the measured currents and voltages. Errors may occur in the measured stator currents and voltages due to the following factors: magnitude errors due to conversion factors and gain, offsets in the measurement system, quantization errors in the digital system, etc. Furthermore, an accurate value for the stator resistance is important. The stator resistance has to be adapted to motor winding temperature changes for accurate flux estimation. At low frequencies the integration can become problematic because the stator voltages become very small and are dominated by the ohmic voltage drop. The voltage drop of the inverter must also be considered at low frequencies. (Vas 1998.)

1.6.4 Stator flux linkage eccentricity correction

For the stator flux linkage eccentricity correction Niemelä (1999) introduced a useful method, Fig. 1.6. The method is designed to be carried out during several electric periods. First, the scalar product of the estimated stator flux linkage and the measured stator current is calculated. The scalar product is then low pass filtered. The correction terms $\psi_{\text{sx, corr}}$ and $\psi_{\text{sy, corr}}$ of the stator

flux linkage are formed as a product of the difference of the calculated and low pass filtered scalar product and the components of the stator flux linkage estimate.·

$$\psi_{sx,corr} = k_{\psi corr} \left[\psi_{s,est} \cdot i_s - \left(\psi_{s,est} \cdot i_s \right)_{filt} \right] \psi_{sx,est} \qquad (1.16)$$

and

$$\psi_{sy,corr} = k_{\psi corr} \left[\psi_{s,est} \cdot i_s - \left(\psi_{s,est} \cdot i_s \right)_{filt} \right] \psi_{sy,est} , \qquad (1.17)$$

where $k_{\psi corr}$ is the correction coefficient of the stator flux linkage estimate.
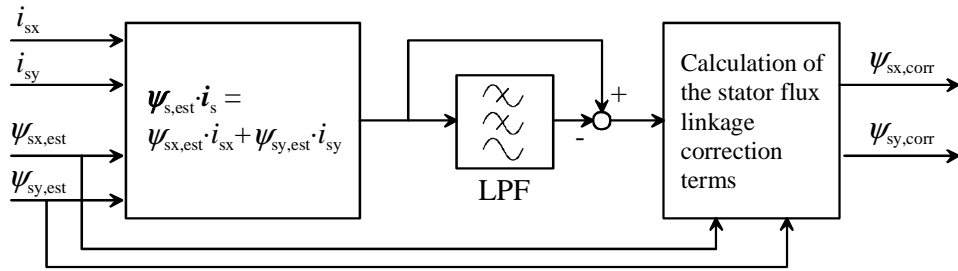

Figure 1.6 Formation of the correction terms of the stator flux linkage (Niemelä 1999).

This stator flux linkage eccentricity correction method introduced by Niemelä (1999) is applied in the simulation model presented further on in this thesis. The stator flux linkage eccentricity correction method will obtain centric stator flux linkage, but the speed and torque ripple still remain. The stator flux linkage eccentricity correction method improves the situation, but does not eliminate the speed and torque ripple completely.

1.6.5   Effect of torque and flux hysteresis bands

Both the flux and torque hysteresis bands influence the inverter switching frequency, harmonic spectra, torque pulsation and the drive losses. Small flux hysteresis band leads to sinusoidal current waveforms and high switching frequency, which increases the switching losses. Distortion of the current waveform is small, and harmonic copper losses in the motor are low. The stator flux vector locus approaches a circle. Increasing the flux hysteresis band causes the stator flux linkage vector locus to form a hexagon, similar to a six-step inverter fed motor (Casadei 1994). Small torque hysteresis band leads to smooth torque, but increases the switching fre-

quency. The switching frequency must be guaranteed not to exceed its limit, which is determined by the thermal restriction of the power devices (Idris 2000). The torque band should be modified consequently in order to keep the total mean switching frequency below a value related to the cooling system (Monti 1998). Due to the hysteresis control of the flux linkage and torque, DTC results in a variable switching frequency and dispersed voltage and current harmonic spectra, which is generally regarded as less annoying noise source than PWM with constant frequency (Xu 2000).

1.7   Current sensing in electric drives

Motor drives and inverter power stages require a combination of current and voltage sensing and power device protection to achieve accurate and fail-safe operation. The following features are desirable in the current sensing device: high accuracy, low cost, high reliability and long life, small size and footprint area and safe optical isolation (galvanic isolation). For the accuracy, in detail, the following features are of major importance: response time, bandwidth, temperature stability, linearity and noise immunity. Requirements for drive performance, cost and size determine the designer's choice of current sensing. The methods of current measurement in high volume applications are mainly based on three choices: resistive shunt, current transformer and Hall effect based sensors. Each technology has its own trade-offs.

Resistive shunts offer low cost and small size, DC and AC current sensing, but add a voltage drop and traditionally do not provide isolation. Recently, however, isolation amplifier resistive current sensing has been introduced (Chew 2003). Typically, a low value resistor (0.25 mΩ to 50 mΩ) is inserted in series with the current conductor. An isolation amplifier measures the voltage across this shunt resistor. The shunt resistor should have low resistance (to minimize power dissipation), low inductance (to minimize di/dt induced voltage spikes) and reasonable tolerance (to maintain overall circuit accuracy). Smaller shunt resistances decrease power dissipation, while larger shunt resistances can improve circuit accuracy by utilizing the full input range of the isolated modulator. If the shunt resistance is reduced, the output voltage across the shunt is also reduced, which means that the offset and noise, which are fixed, become a larger percentage of the signal amplitude. If the sensed currents are large enough to cause significant heating of the shunt, the temperature coefficient of the shunt can introduce non-linearity due to the signal dependent temperature rise of the shunt.

Current transformers are also low cost and additionally provide isolation. They do not require external power, and exhibit no offset voltage at the zero current level. Under sinusoidal conditions the accuracy of current transducers consisting of traditional current transformers with a magnetic core can be very high, provided that the load applied to their output is close to the nominal value. When distorted waveforms are measured (typically because of the presence of power electronic components) these devices can be inadequate, owing to their non-linear behaviour caused by saturation and hysteresis phenomena. In addition, they are intrinsically unsuitable to measure DC components. (Locci 2001.)

Hall effect based sensors, both open and closed loop technology, provide isolation and frequency bandwidth from DC to high frequency AC (200 kHz), but have some limitations in offset voltage, linearity and temperature performance. In the following, the Hall effect sensors are the measurement method to be analysed, because of their wide application in current and voltage measurements in variable speed drives.

1.7.1 Hall effect sensor

Hall effect devices are thin plates of a conducting material, provided with four electrical contacts. A control or bias current is supplied via two of the contacts and the other two contacts are used for sensing, Fig. 1.7. If a magnetic field is applied to the device, the Hall voltage U_H is detectable between the sense contacts (Hall 1879). This phenomenon is utilised in current measurements. The primary current to be measured causes a change in the magnetic field in which a Hall device is located (Norton 1989). The material used for the thin plate was originally gold, but today Hall devices are made of semiconductors, such as GaAs, InSb, InAs or Si (Schott 1997; Costa 2001). The semiconductor type is specifically selected for the stated use (one having a high Hall constant, or Hall coefficient). Hall effect current sensors can be used for DC and AC measurements.
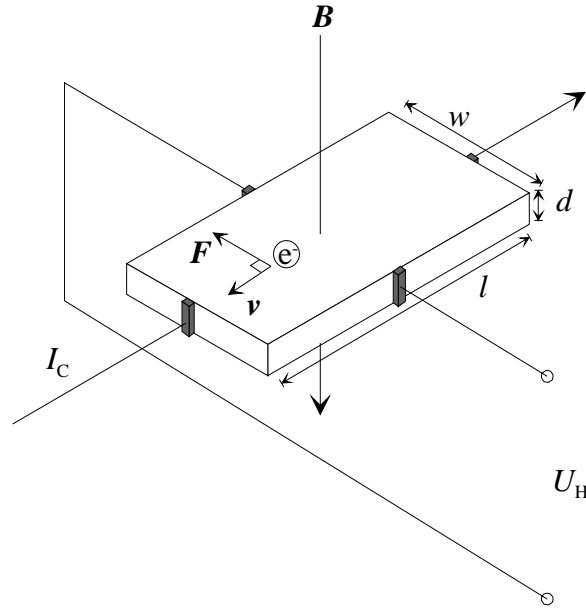
Figure 1.7 Hall-effect device. I_C is a constant control current, B is the magnetic flux density and U_H is the Hall voltage. A charged particle moving with velocity v experiences a Lorentz force F in a thin sheet of semiconducting material having thickness d, length l and width w.

In Fig. 1.7, when no magnetic field is present, current distribution in the thin sheet is uniform and no potential difference is sensed across the output. When a perpendicular magnetic field is present, as in Fig. 1.7, a Lorentz force is exerted on the current. This force changes the current distribution, resulting in a potential difference (Hall voltage) across the output. The Lorentz force describes the force F experienced by a charged particle with charge q moving with velocity v in a magnetic field B.

$$F = q(v \times B) \tag{1.18}$$

The amplitude of the Hall voltage is a function of the charge concentration (magnitude of the current) in the conducting element, the strength of the magnetic field, the type of material, and the dimensions of the element. For the arrangement in Fig. 1.7, with a magnetic flux density B perpendicular to the control current I_C, the Hall voltage can be expressed as

$$U_H = \frac{I_C B}{qnd} = \frac{R_H I_C B}{d} \tag{1.19}$$

where n is the number density of charge carriers [m^{-3}], d is the thickness of the thin sheet [m] and

$$R_\mathrm{H} = \frac{1}{qn} \qquad (1.20)$$

is the Hall coefficient for the material used. The unit of the Hall coefficient is [m^{3}C^{-1}], or, equivalently [VmA^{-1}T^{-1}] (volt metres per ampere tesla).

The Hall voltage may also be expressed in terms of the impressed potential U_C that drives the control current,

$$U_\mathrm{H} = \frac{\mu U_\mathrm{C} B w}{l}, \qquad (1.21)$$

where μ is the carrier mobility [Csm^{-1}], w is the sheet width and l is the sheet length. (Popović 1991.)

From the equations (1.19) and (1.21) it can be seen, that in order to get high values of Hall voltage, the Hall element material should have a low carrier density and the carriers should have high mobility. Since semiconductors have much smaller carrier concentrations than metals, they are preferred for Hall elements. Properties of some semiconductors are shown in table 1.1.

Table 1.1   Mobilities of electrons (μ) and carrier densities (n) in various intrinsic semiconductors at 300 K (Bar-Lev 1993; Shur 1990).

Material	μ [cm^{2}V^{-1}s^{-1}]	n [cm^{-3}]
Ge	3900	$2.4 \cdot 10^{13}$
Si	1450	$1.2 \cdot 10^{10}$
GaAs	8500	$2 \cdot 10^{6}$
InSb	80000	$\approx 10^{16}$
InAs	23000	$1.3 \cdot 10^{15}$

Unfortunately, Hall elements usually suffer from offset (due to misalignment of contacts, mechanical stresses in processing or packaging) and temperature dependence. Therefore, some sort of offset reduction or compensation method should be used (Choi 2002; Căruntu 2002).

The voltage output of the Hall element is very small (µV) and requires additional electronics to achieve useful voltage levels. When the Hall element is combined with the associated electronics, it forms a Hall effect sensor (or transducer). Two basic types of the Hall effect current transducer are used widely in industrial applications: open loop current transducer and closed loop current transducer.

1.7.2   Open loop current transducer

The magnetic flux created by the primary current I_P (current to be measured) is concentrated in a magnetic circuit and measured using a Hall device inserted in the gap of the flux concentrator, Fig. 1.8. The output from the Hall device is the voltage U_H proportional to the primary current.
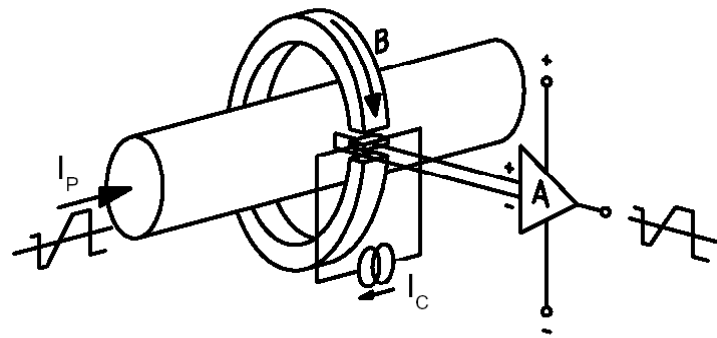

Figure 1.8   Open loop current transducer (Bürkel 1996). I_P is the primary current to be measured, B is the magnetic flux created by the primary current and I_C is the control current of the Hall element. The small output voltage of the Hall element is amplified.

The linearity of the open loop sensor is determined by the characteristics of the magnetic core and the Hall generator. Offset drift over temperature is determined primarily by the temperature sensitivity of the Hall generator. The flux concentrator is typically a ferrite or silicon-steel core. At excessive current, the core material will saturate. The sensor will no longer supply an increasing voltage output to increasing conductor field strength. After the excitation of the current sensor, a residual flux will be present in the core. This remanence will create a shift in the zero offset voltage level.

The linear region of the magnetisation curve of the magnetic circuit, Fig. 1.9, defines the measurable current range of the open loop transducer.
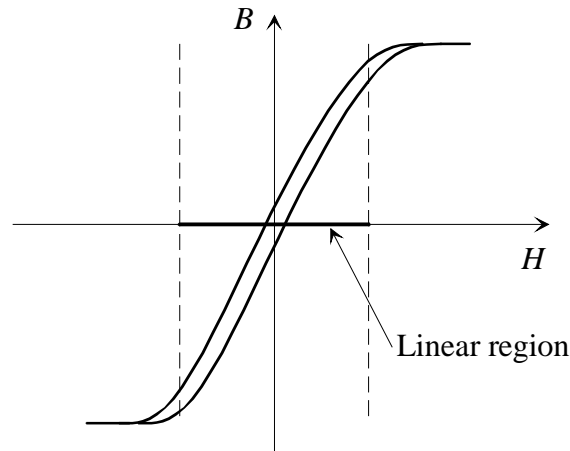

Figure 1.9 Magnetisation curve of the current transducer's magnetic circuit.

A large air-gap linearises the magnetic characteristics and reduces the remanent induction. However, this increases the flux leakage, which disturbs the Hall sensor output voltage (parasitic voltage induced in the connections). Costa (2001) claims that the accuracy of this kind of a current sensor is never better than 5 %. By integrating the Hall sensor, the amplifier and the correction circuits, the accuracy reaches 1 %. Split-core, clamp-on versions are also used for current measurement probes.

1.7.3   Closed loop current transducer

Hall effect closed loop current transducers are used in a number of industrial applications. Typical applications are frequency converters and three-phase drives, electric welding equipment, uninterruptible power supplies (UPS), electric vehicles and switching power supplies.

Closed loop current sensors are based on the principle of the Hall effect and the null balance method or zero magnetic flux method. The primary current, I_P, flowing through the conductor produces a magnetic field, which is detected by a Hall effect device and, via an electronic amplifier, is immediately balanced by injecting a current, I_S, into the secondary winding, Fig. 1.10. The magnetic flux from the secondary coil cancels out the flux from the primary to zero. The ampere-turns of the secondary is thus equivalent with the primary,

$$N_P I_P = N_S I_S . \qquad (1.22)$$

where N_P is the number of primary turns and N_S is the number of secondary turns.

The output from the current sensor is the balancing current, I_S, which should be a perfect image of the primary current reduced by the number of secondary turns N_S (typically 1000). This current can be expressed as a voltage passing it through a resistor R_M. A capacitor is often added to attenuate high distortion frequencies. Because of the zero magnetic flux method, the linearity of the closed loop transducers is better than the open loop transducers.
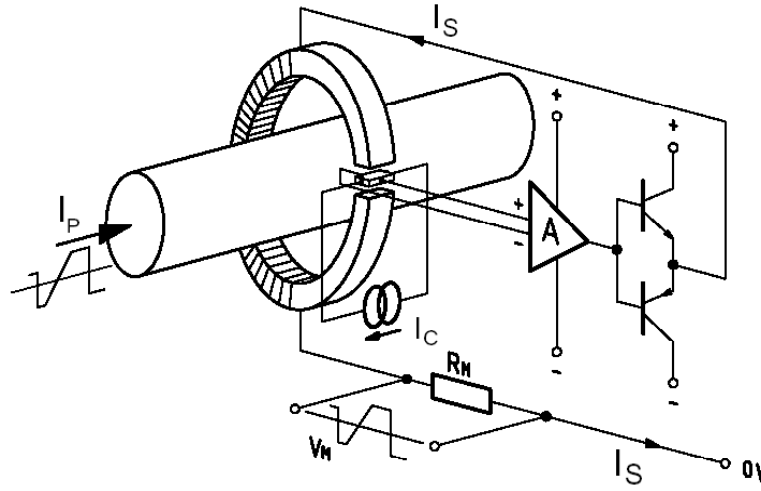

Figure 1.10 Closed loop current transducer (Bürkel 1996). I_P is the primary current to be measured, I_S is the secondary balancing current, I_C is the control current of the Hall element, R_M is a measurement resistor and V_M is the output voltage of the transducer.

Despite the null balance method, the output current of the closed loop transducer is not exactly zero when the primary current is zero. A small offset current from the operational amplifier and Hall effect sensor is present. This current is typically less than ±0.2 mA. The closed loop sensor also limits the magnitude of the current that can be sensed, since the device may only drive a finite amount of compensation current. Other drawbacks of the closed loop sensor are increased costs, larger size and increased supply current consumption.

Some converter manufacturers oversize their Hall effect closed loop transducers in order to avoid saturation of the transducer core by occasional inverter over-current. The sensor must be

oversized too, because the same sensor is used also during fault situations. Thus typically only 50 % of the rated value of a sensor is used during normal operation and the converter rated current is only 30 % of the sensor measuring range. This increases slightly the effect of current measurement errors since the accuracy of the Hall effect transducers is at its best towards the maximum end of the sensed range.

1.7.4 Closed loop voltage transducer

The Hall effect voltage transducers are based on the same principle as their current transducer counterpart. The main difference is in the primary circuit, which is made with a winding having a high number of turns. This provides the necessary ampere-turns for the creation of the primary induction, while having a low primary current. A resistance is connected in series with the primary winding. This resistance can be external or integrated into the transducer. A typical application of the Hall effect closed loop voltage transducers in electric drives is the monitoring of DC-link voltage in frequency converters.

1.8 Previous methods of torque ripple compensation

Active control schemes are used to modify the excitation to correct any of the non-ideal characteristics of the motor or its power supply. Many of these techniques apply active cancellation of the pulsating torque components, which would otherwise be generated using the classic sinusoidal current excitation waveforms. These techniques rely on a priori knowledge of the design parameters of the motor or the use of self-tuning mechanisms to adapt to the torque production characteristics of the machine. Pre-programming stator current excitations to cancel the ripples in the torque necessitates that these currents are computed off-line and are based on machine data measured on the test motor. Such methods are valid only to a particular machine. Moreover, they are sensitive to parameter changes due to variation in operating conditions.

Clenet (1993) determined the current supply wave shapes by finite element method for the compensation of the torque ripple of permanent magnet motors. The pre-calculated current waveforms were used to compensate electromagnetic torque ripple and cogging torque.

Barro (1997) proposed a torque ripple compensation of induction motors under field orientated control (FOC). A spectral torque ripple model was proposed where harmonics of the actual field

frequency were used to model the real ripple producing effects of the system. A ripple cancellation term was generated based on this model and parameter identification. This ripple cancellation term was injected into the torque control input of the FOC algorithm. The method required a torque sensor to obtain a compensation torque. The need for a torque sensor restricts the usefulness of this method. Choi (1998) proposed a torque ripple compensator, which calculated the compensation torque from speed information. The method required a speed sensor. The stability of the proposed scheme was dependent on proper compensation gains selections. Beccue (2003) even proposed adding a piezoelectric sensor to measure the effects of torque ripple harmonics in a brushless DC machine. The disturbances in machine housing were used as an indicator of torque ripple amplitude.

Lam (2001) proposed an iterative learning control scheme, which generates a compensation reference current based on the error between the desired and the actual currents. By augmenting this compensation current with the main reference current, the resultant current reduces periodic torque ripples. The learning control method was suitable to reduce periodic torque ripples. The rotor position was detected using an incremental encoder and the speed was estimated using a FIR filter. By using the iterative learning control method, the torque ripple was reduced, but not eliminated completely due to some properties of the algorithm presented.

1.9   Outline of the thesis

The work is divided in six chapters, the brief descriptions of which will be given in the following.

Chapter 1 gives an introduction to the torque vibration problems encountered in electric drives and the needs for smooth torque production. Relevant background information of the applied motor type, control method and sensor types prepares ground for the next chapters.

Chapter 2 gives an analysis of the effect of the converter non-idealities on the torque ripple.

Chapter 3 shows the developed simulation models used for the torque ripple analysis. The simulation model of the electric drive, including converter non-idealities, is presented. The coupled simulation model of the electric drive and the mechanical load is presented.

Chapter 4 deals with the detection and reduction of speed and torque ripple. A method to compensate current measurement errors is proposed.

Chapter 5 shows experimental results on some of the analysed and simulated converter non-idealities that produce torque ripple. First the effect of current measurement errors on torque ripple is shown. Then the compensation method of current measurement errors, introduced in chapter 4, is tested with a laboratory drive, which consists of a commercial frequency converter hardware with a self-made software and a prototype PMSM.

The last chapter gives the conclusions of the thesis.

1.10   The scope and the main scientific contributions of the thesis

The aim of this thesis is to study and clarify the torsional vibrations caused by an inverter in electrically driven machine systems. Being a part of a larger project – divided to several parts, this work has its main focus on the inverter part of the system, whereas the emphasis is minor on the motor and the mechanical load.

The significance of the different vibration sources of the inverter on the entire system is to be found. Another goal is to find possible compensation methods for the vibrations caused by the inverter. From the industrial point of view, during the project, the interest was to find reasons for the first ten harmonics of torque empirically observed in industrial applications.

The main objective in the simulation part of this work is to propose a simulation model of the electric drive that uses existing software on the market, is simple, computationally fast, easily configurable, reasonably accurate and allows investigation with wide variation of system parameters. In this work a simulation model of the inverter was generated to be coupled with simulation software of the mechanical load. The model enables to identify potential problems causing torque vibrations and possibly damaging oscillations in electrically driven machine systems. The model can be utilized in the design and troubleshooting of electrically driven machine systems. The model is capable of coupling with another simulation software of complex mechanical loads. Furthermore, the simulation model of the frequency converter's control algorithm can be applied to control a real frequency converter.

A method to compensate current measurement errors is proposed. The method is based on analysing the amplitude of a selected harmonic component of speed as a function of time and selecting a suitable compensation alternative for the current error. The speed can be either measured or estimated, so the compensation method is applicable also for speed sensorless drives. The compensation method was tested in both simulation and experimental environment. The method was found to reduce speed and torque ripple under the desired level. The speed ripple compensation method presented is suitable not only for the direct torque control method and PMSM used herein, but also for other control methods and motor types. Moreover, this method can be implemented by modifying only the software in an adjustable speed drive.

2   GENERATION OF TORQUE RIPPLE DUE TO NON-IDEALITIES OF THE CONVERTER

Several error sources related to the converter may cause torque ripple. Errors in the measured stator current and estimated voltage signals cause an error in the estimated stator flux linkage (1.12) and torque estimates (1.13) and, further on according to the characteristic properties of the control system, an error in the torque control producing harmonic torques (Laurila 2002b). The error sources to be considered in detail in the following are the current and voltage measurement errors, which seem to be the most important primary sources for poor torque quality in electric drives.

2.1   Current measurement errors

Measurement accuracy of current transducers depends on various factors such as electrical parameters or parameters linked to the environment conditions. Hall effect current transducers are commonly used in frequency converters for current measurement of the output phases. Factors determining the accuracy of Hall effect open loop current transducers at ambient temperature are: DC offset voltage at zero current, loop gain and linearity. Depending on the operating temperature offset drift and gain variation determine the accuracy. Factors determining the accuracy of Hall effect closed loop current transducers at ambient temperature are the DC offset current at zero current and non-linearity. Depending on the operating temperature the offset drift determines the accuracy. (Bürkel 1996.)

Typical rating of the accuracy of the open loop transducers is ±1 % and for the closed loop transducers ±0.5 %. However, industrial closed loop current sensors with ±1% accuracy are widely used. This overall accuracy rating usually takes into account the offset current, linearity and thermal drift, but may also exclude the offset current. The effects taken into account vary depending on the model or the manufacturer. The principal error types of a current transducer: offset error, gain error and non-linearity, are introduced in Fig. 2.1.
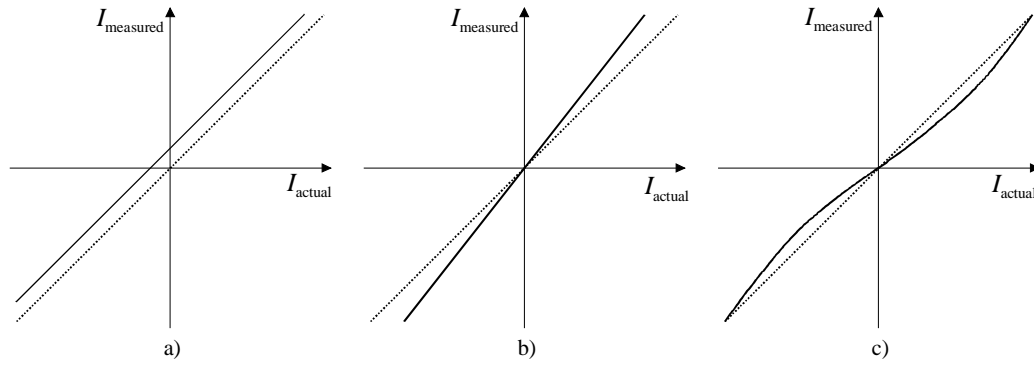
Figure 2.1   The principal error types of a current transducer: a) offset error, b) gain error and c) non-linearity. The dotted line corresponds to an ideal straight line and the solid line corresponds to the measured value.

2.1.1   Offset error

In an offset error the transfer function of the transducer is parallel to an ideal curve, but does not pass through the origin, as shown in Fig. 2.1 a). In an electric drive the stator currents are measured by current sensors and transduced into voltage signals, which are then transformed via low-pass filters and A/D converters to digital values, Fig. 2.2. DC offset in the measured current values is possible due to unbalanced power supply voltage of the current sensor and analogue devices in the current measurement path (Chung 1998; Antić 1994). In Fig. 1.10 the Hall voltage is amplified by an op-amp, then fed to a push-pull amplifier. Both of these amplifiers need a power supply, the unbalance of which causes an offset error. Another cause of the offset error is the magnetic offset due to the residual magnetism of the magnetic material used in the transducer. The value of the magnetic offset depends on the magnetisation state of the magnetic circuit. At high overload current conditions, when the magnetic circuit has been saturated, this error is maximum. (Bürkel 1996.)
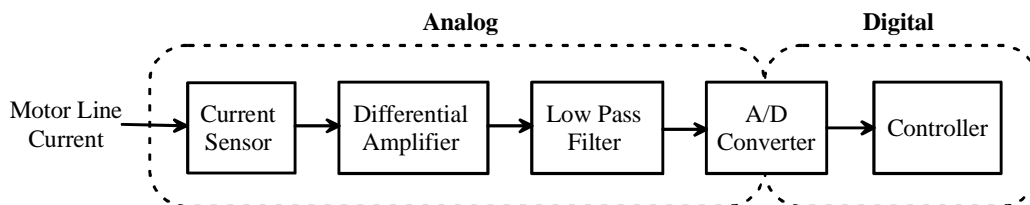

Figure 2.2 Current measurement path in an adjustable speed drive (Song 2000).

When the primary current exceeds approximately three times its nominal value, the secondary circuit can no longer compensate the magnetization originated by the primary winding. There-

fore, the core is magnetised and the magnetic flux follows a hysteresis loop. An additional DC offset component and non-linearity appear. (Cristaldi 2001.)

The current measurement error in the measured phase current is developed when the offset error in the current measurement path is added to the actual phase current. In practice, often only two motor phase currents are measured and the third phase current is calculated. The measured currents i_{am} and i_{bm} are

$$i_{am} = i_a + \Delta i_a \ , \tag{2.1}$$

$$i_{bm} = i_b + \Delta i_b \ , \tag{2.2}$$

$$i_{cm} = -(i_{am} + i_{bm}) = -(i_a + i_b) - (\Delta i_a + \Delta i_b) \ , \tag{2.3}$$

where i_a and i_b are the actual phase currents, and Δi_a and Δi_b are the DC offset values. Inserting the error values of the measured currents into the current vector determination

$$\boldsymbol{i}_s = \frac{2}{3}\left(i_a e^{j0} + i_b e^{j\frac{2\pi}{3}} + i_c e^{j\frac{4\pi}{3}} \right) , \tag{2.4}$$

the error vector can be calculated as:

$$\boldsymbol{i}_{serror} = \frac{2}{3}\left(\Delta i_a e^{j0} + \Delta i_b e^{j\frac{2\pi}{3}} + \left(-\Delta i_a - \Delta i_b \right) e^{j\frac{4\pi}{3}} \right) , \tag{2.5}$$

which will result in a stable error vector in the direction of $e^{j\alpha}$

$$\boldsymbol{i}_{serror} = i_{serror}\, e^{j\alpha} \ , \tag{2.6}$$

where

$$\alpha = \arctan\left(\frac{\Delta i_a + 2\Delta i_b}{\sqrt{3}\Delta i_a}\right) . \tag{2.7}$$

This is a stable error vector in the stationary co-ordinate system. If it is assumed that the stator flux linkage vector is not remarkably disturbed by the current model variations, but mainly maintains its circular locus, it produces with the stable current error vector a pulsating error torque at the fundamental frequency, when the stator flux linkage rotates at synchronous speed, Fig. 2.3.
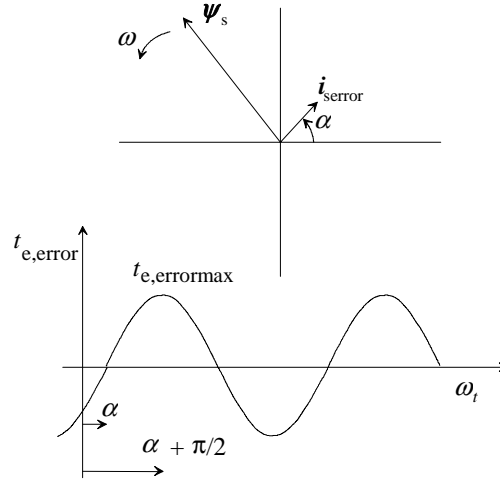

Figure 2.3   The stationary error vector i_serror produces a torque estimation error $t_\text{e,error}$ in the control system and will thus be compensated by the control. As a result, a torque ripple will be found.

To define the size of the torque ripple due to the offset error, the stator currents are examined in the following. In the rotor reference frame the measured currents i_sdm and i_sqm are

$$i_\text{sdm} = i_\text{sd} + \Delta i_\text{sd} \tag{2.8}$$

$$i_\text{sqm} = i_\text{sq} + \Delta i_\text{sq} \tag{2.9}$$

where i_sd and i_sq are the actual currents and Δi_sd and Δi_sq are the error components due to the DC offset currents superimposed on the actual current. The actual currents in rotor reference frame are

$$i_\text{sd} = i_\text{sx} \cos\theta + i_\text{sy} \sin\theta \tag{2.10}$$

$$i_{sq} = -i_{sx} \sin\theta + i_{sy} \cos\theta \tag{2.11}$$

where i_{sx} and i_{sy} are the stator currents in the stator reference frame

$$i_{sx} = i_a , \tag{2.12}$$

$$i_{sy} = \frac{1}{\sqrt{3}} i_a + \frac{2}{\sqrt{3}} i_b \quad \text{and} \tag{2.13}$$

$$\theta = 2\pi ft . \tag{2.14}$$

The error currents, due to DC offset, in rotor reference frame are

$$\Delta i_{sd} = \Delta i_{sx} \cos\theta + \Delta i_{sy} \sin\theta \quad \text{and} \tag{2.15}$$

$$\Delta i_{sq} = -\Delta i_{sx} \sin\theta + \Delta i_{sy} \cos\theta = -\Delta i_a \sin\theta + \frac{1}{\sqrt{3}} \left(\Delta i_a + 2 \cdot \Delta i_b \right) \cos\theta . \tag{2.16}$$

If for simplicity a surface-mounted PMSM is assumed ($L_{sd} = L_{sq}$), then for maximum torque per unit current $I_{sd} = 0$ and the torque is produced by the q-axis current as

$$t_e = \frac{3}{2} p \Psi_{PM} i_{sq} . \tag{2.17}$$

The estimated torque t_{e_est} will consist of the actual torque t_e and the superimposed ripple torque Δt_e

$$t_{e\_est} = t_e + \Delta t_e , \tag{2.18}$$

where the actual torque is

$$t_e = \frac{3}{2} p \Psi_{PM} i_{sq} \tag{2.19}$$

and the ripple torque is

$$\Delta t_e = \frac{3}{2} p \Psi_{PM} \Delta i_{sq} . \tag{2.20}$$

By substituting (2.16) into (2.20), the ripple torque can be obtained as

$$\Delta t_e = \frac{3}{2} p \psi_{PM} \left(-\Delta i_a \sin\theta + \frac{1}{\sqrt{3}}(\Delta i_a + 2 \cdot \Delta i_b)\cos\theta \right). \tag{2.21}$$

Let us consider a situation, where $3/2 \cdot p \cdot \psi_{PM} = 1$, and see the effect of different offset errors on the torque ripple component. If $\Delta i_a = 1\%$ and Δi_b varies, we get a series of torque ripple waveforms in Fig. 2.4. Maximum torque ripple is observed at $\Delta i_a = \Delta i_b = 1\%$ and is 4% peak to peak.
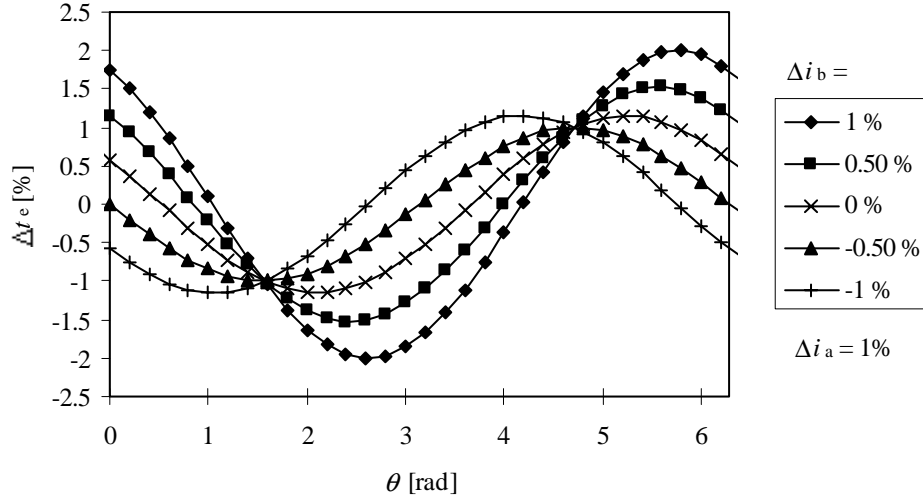
Figure 2.4 Torque ripple Δt_e in a permanent magnet motor due to offset in a-phase $\Delta i_a = 1\%$ and offset in b-phase, Δi_b, as a parameter. $\theta = \omega t$.

The torque ripple waveform shown in Fig. 2.4 follows the waveform of the q-axis error current, Δi_{sq}, when $\Delta i_a = 1\%$ and Δi_b is varied from 1% to –1%. Some other possible combinations of Δi_a and Δi_b and the resulting current ripple waveforms are given in Appendix C. When only two phase currents are measured, the amplitude of the torque ripple producing q-axis current can be derived as

$$\Delta \hat{i}_{sq} = \frac{2}{\sqrt{3}}\sqrt{\Delta i_a^2 + \Delta i_a \Delta i_b + \Delta i_b^2} \ . \tag{2.22}$$

If, for example, the absolute value of the offset errors is maximum 1 % in the two phases, the worst case happens when $\Delta i_a = \Delta i_b$. This results in ripple current amplitude $\Delta \hat{i}_{sq} = 2$ %. The frequency of the ripple is the same as the supply frequency.

In some cases the stator current is measured from all of the three phases. This gives an additional possibility for offset error in the third phase. When all three phase currents are measured, the amplitude of the torque ripple producing q-axis current is

$$\Delta \hat{i}_{sq} = \frac{2}{3} \sqrt{\Delta i_a^2 + \Delta i_b^2 + \Delta i_c^2 - \Delta i_a \Delta i_b - \Delta i_a \Delta i_c - \Delta i_b \Delta i_c} \ , \qquad (2.23)$$

where Δi_c is the offset error in c-phase. This time the worst case happens when the offset error of one phase has a different sign than the other two phases, for example, $\Delta i_a = \Delta i_b = 1\%$ and $\Delta i_c = -1$ %. This results in ripple current amplitude $\Delta \hat{i}_{sq} = 4/3 \approx 1.33$ %. Other combinations of Δi_a, Δi_b and Δi_c and the resulting current ripple waveforms are given in Appendix C.

2.1.2 Gain error

The output of a current sensor is scaled to fit the input range of an A/D converter. During the amplifying process a gain error is possible. The gain error produces a change in the slope of the transducer's transfer function, Fig. 2.1 b). The two measured currents i_{am} and i_{bm} may have gain errors k_a and k_b, as in

$$i_{am} = i_a (1 + k_a) , \qquad (2.24)$$

$$i_{bm} = i_b (1 + k_b) , \qquad (2.25)$$

$$i_{cm} = -(i_a + i_b) - (k_a i_a + k_b i_b) . \qquad (2.26)$$

Inserting, again, the error values of the measured currents into the current vector determination we get an error vector as:

$$\boldsymbol{i}_{serror} = \frac{2}{3} \left(k_a i_a e^{j0} + k_b i_b e^{j\frac{2\pi}{3}} + \left(-k_a i_a - k_b i_b \right) e^{j\frac{4\pi}{3}} \right) . \qquad (2.27)$$

As an example, it may be shown that if $k_b = 0$ and there exists only an error in the gain of phase a ($k_a \neq 0$), we get a pulsating current error vector that may be divided into a clockwise rotating and a counter clockwise rotating part. The former part produces with the counter clockwise rotating stator flux linkage estimate a pulsating torque having a double frequency with respect to the fundamental. This is shown in Fig. 2.5.
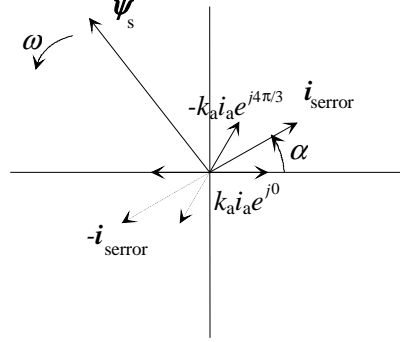

Figure 2.5 Pulsating error vector $\boldsymbol{i}_{serror}$ produced by gain error k_a in current measurement of phase a.

The error vector in this case will have its maximum at the time when i_a has its maximum and the error vector will be

$$\boldsymbol{i}_{serror}\left(t = 0\right) = \frac{2}{3}\left(k_a i_a e^{j0} - k_a i_a e^{j\frac{4\pi}{3}} \right) . \tag{2.28}$$

The error vector as a function of time is then

$$\boldsymbol{i}_{serror}\left(t\right) = \frac{2}{3}\left(\frac{\sqrt{3}}{2} k_a i_a e^{j\left(\frac{\pi}{6}+\omega t\right)} + \frac{\sqrt{3}}{2} k_a i_a e^{j\left(\frac{\pi}{6}-\omega t\right)} \right) . \tag{2.29}$$

The clockwise rotating component

$$\boldsymbol{i}_{serror,cw} = \frac{1}{\sqrt{3}} k_a i_a e^{j\left(\frac{\pi}{6}-\omega t\right)} \tag{2.30}$$

produces a torque component pulsating at a frequency twice the fundamental.

The error currents, due to the gain error, in the stator reference frame are

$$\Delta i_{sx} = k_a \sin \theta \, , \tag{2.31}$$

$$\Delta i_{sy} = \frac{1}{\sqrt{3}} k_a \sin \theta + \frac{2}{\sqrt{3}} k_b \sin\left(\theta - \frac{2\pi}{3}\right). \tag{2.32}$$

In the rotor reference frame the torque ripple producing q-axis current component due to gain error will be

$$\Delta i_{sq} = -k_a \sin^2 \theta + \frac{1}{\sqrt{3}}\left(k_a \sin \theta + 2k_b \sin\left(\theta - \frac{2\pi}{3}\right)\right)\cos \theta$$

$$= \frac{1}{\sqrt{3}}(k_a - k_b)\sin\left(2\theta + \frac{\pi}{3}\right) - \frac{1}{2}(k_a + k_b). \tag{2.33}$$

The waveforms of the torque ripple producing q-axis current component, Δi_{sq}, due to 1 % gain error in a-phase and gain error in b-phase, k_b, as a parameter, are shown in Fig. 2.6.
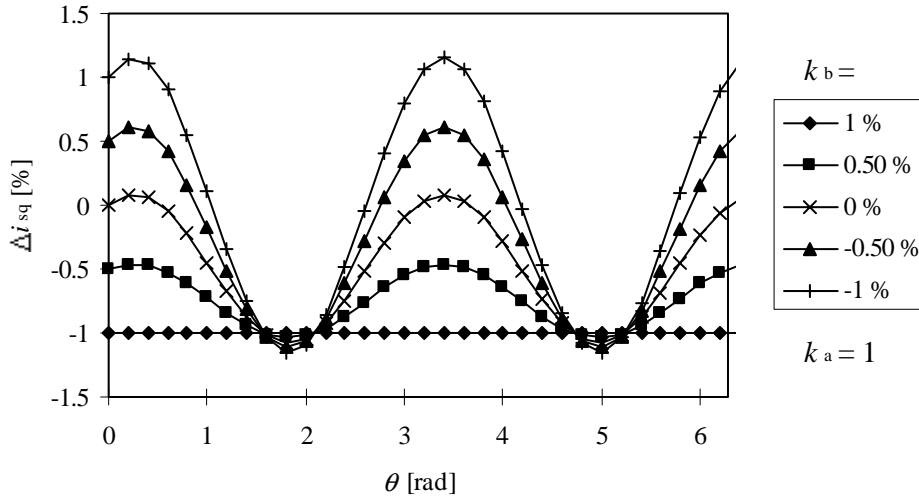
Figure 2.6   Torque ripple producing q-axis current component in a permanent magnet motor, Δi_{sq}, due to 1 % gain error in a-phase and gain error in b-phase, k_b, as a parameter.

Maximum error is observed, when $k_a = -k_b = 1\%$, and is $\Delta \hat{i}_{sq} = 2/\sqrt{3} \approx 1.15$ %. It is notice-able that, when $k_a = k_b$, the error vector is stable instead of oscillating at double the fundamental

frequency. This will not produce torque ripple, but it still produces an error in the torque esti-mate. With three phase current measurement the maximum error is observed, for example, when $k_a = -k_b = -k_c = 1\%$, and is $\Delta \hat{i}_{sq} = 2/3 \approx 0.66\%$. More waveforms of Δi_{sq} due to gain error with two and three phase current measurements are given in Appendix C.

In the offset and gain error cases shown above, with equal maximum current error levels, the offset error will produce higher torque ripple amplitude than the gain error. Furthermore, two phase current measurement will produce higher ripple amplitude than three phase current meas-urement. The torque ripple due to the gain error also exists on higher frequency than the torque ripple due to the offset error, whereupon the resulting torque ripple on the shaft may be lower because of the attenuation by the rotor inertia.

In both these cases the error takes place in the torque estimate. The control system tries to com-pensate for these errors and thus a real torque error in the motor is established in an opposite direction.

2.1.3   Non-linearity

Although an analogue output Hall sensor is considered to be linear over its span, in practice, no sensor is perfectly linear. Linearity indicates how straight the transfer function of the transducer is. For a linear device if $y_1 = f(x_1)$ and $y_2 = f(x_2)$, then $y_1 + y_2 = f(x_1 + x_2)$ (Göpel 1989). Non-linearity is generally expressed as the maximum deviation from the ideal current curve (Doebe-lin 1990). Typical rating for linearity of the open loop transducers is $\pm 0.5\%$ and the closed loop transducers ± 0.1 to 0.25%. However, this does not include information about the shape of the non-linear curve – it only tells the tolerance. For open loop current transducers with powdered iron toroid core the linearity and hysteresis is shown to be approximately 1% at current levels near zero (Emerald 1999). By using ferrite cores hysteresis is smaller than in powdered iron cores (Emerald 1998). Furthermore, non-linearity – "linearity error" – can be divided into two categories; "integral linearity error" and "differential non-linearity" (Coombs 1995).

An integral linearity error is a gradually increasing non-linearity error that becomes largest be-tween zero and half scale and then reduces towards full scale. The integral linearity errors will appear like gain errors, which vary throughout the measuring range, and are expressed as a per-centage of the reading representing the maximum error over the full range. (Coombs 1995.)

Differential non-linearities are linearity errors which cause abrupt reading changes for small changes in the input. These errors usually can occur anywhere throughout the full range of the analogue-to-digital converter (ADC) and usually appear like an offset or additional noise in the measurement reading. Differential linearity errors are expressed by a percentage of range error like offset voltages. If the differential linearity error is large enough, one or more quantized values may be missed and therefore never produced by the ADC. (Coombs 1995.)

One reason for the non-linearity is the already mentioned over-current situation. Another problem arises, when the transducer works over a reduced portion of its dynamic range. The amount of non-linearity increases dramatically when the current amplitude decreases. If the current level is very low with respect to the transducer measurement range, the non-linearity error may increase more than one order of magnitude above the nominal value. (Cristaldi 2001.)

2.2 Experiments on current measurement non-linearity

This chapter is based on experimental results on the current measurement non-linearity of a commercial current transducer.

2.2.1 Transfer function of a closed loop current transducer

The transfer function of a closed loop current transducer describes its output in terms of its input. Here the transfer function is expressed in terms of a graph instead of an equation. The transfer function used here expresses the relationship between the primary current I_P (input) and the secondary current I_S (output). In the experiment a LA55-P closed loop current transducer of 50 A rated current was used (LEM 1998).

2.2.2 DC measurements

An experimental setup was arranged to explore the shape of the non-linearity of a current transducer. The input of the transducer was a DC-current from a DC-power supply. 15 turns were turned around the coil to magnify the available current value from the supply (DC 0…10 A). The primary current was measured by FLUKE 89 IV true rms multimeter and the secondary current was transformed to a voltage signal across a resistor and measured by Agilent 34401A 6 ½ Digit Multimeter. The DC current was gradually increased from zero to the positive saturation level, then decreased, polarity reversed and increased to the negative saturation level etc.

The procedure was repeated for three cycles. Fig. 2.7 shows the output current of the transducer I_S versus the measured current I_P.
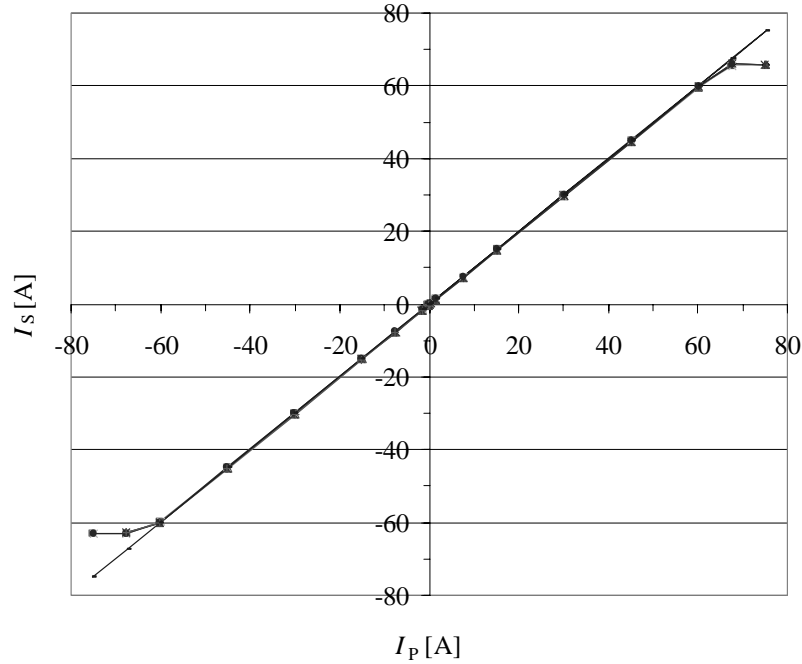

Figure 2.7   Output current of the transducer I_S versus the measured current I_P. The transducer seems to be quite linear at the +60…-60 A range on this rough scale.

The transducer begins to saturate after 60 amperes. This is due to the supply voltage capability of the transducer, because the output of the amplifier cannot exceed the limits imposed by the power supply. In fact, the amplifier begins to saturate before the limits of the power supply are reached. This saturation takes place in the amplifier and not in the Hall element. Therefore, large magnetic fields will not damage the Hall effect sensors, but rather drive them into saturation. Although the linearity of the current transducer may seem quite good according to Fig. 2.7, certain non-linearities still exist. The deviation of the measured output current I_S in the secondary circuit from the actual current I_P in the primary circuit is defined here as

$$\Delta I = \frac{I_S - I_P}{I_{PN}} \cdot 100 \, [\%] \, , \tag{2.34}$$

where I_{PN} is the rated primary current of the transducer.

The deviation ΔI is demonstrated in Fig. 2.8. An offset level of –0.6 % of the rated current before turning on the power supply was detected. After the measurements an offset level of –0.5 % was present. In Fig. 2.8, two offset levels can be detected; one for the rising current and the other for the falling current. Therefore, the transducer has saturated and has a hysteresis-like transfer function, which represents a non-linearity in the transducer. The error of the transfer function has its maximum value at the highest absolute value of the current in the linear region and minimum value near the zero level. This is typical for a gain error.
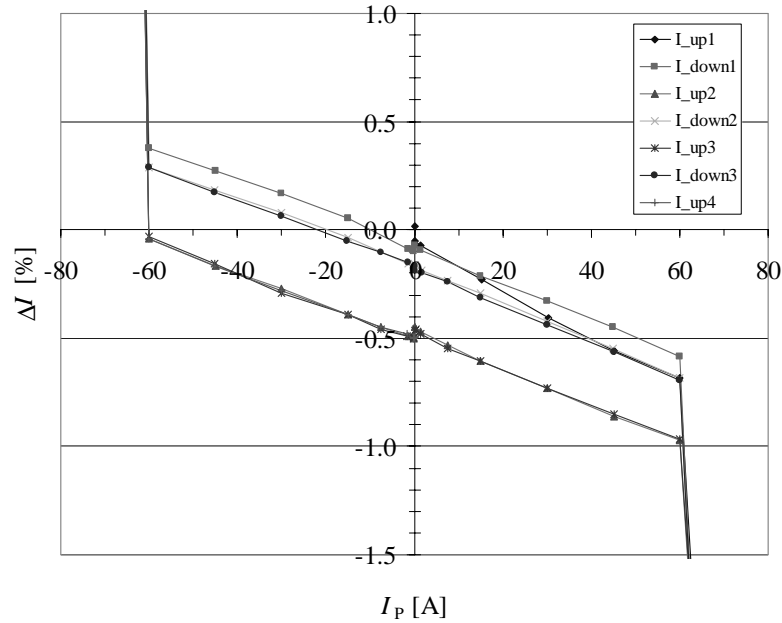
Figure 2.8   Percentage error of the output current in the measured range. The measured current was a DC current, repeatedly increased gradually to positive saturation level and decreased to negative saturation level. The secondary current was transformed to a voltage across an accurate resistor.

The output from the current sensor is the balancing current, which is an image of the primary current reduced by the number of secondary turns (typically 1000). This current was expressed as a voltage passing it through a resistor (nominal value 133 Ω, measured value 132.57 Ω). To eliminate the possible effect of the resistance inaccuracy on the gain error, a similar measurement was repeated without the external resistor. The secondary current was measured straight with a mA to μA –level multimeter. This time the saturation starts at higher current level and causes hysteresis, Fig. 2.9. Offset and gain errors are again present.
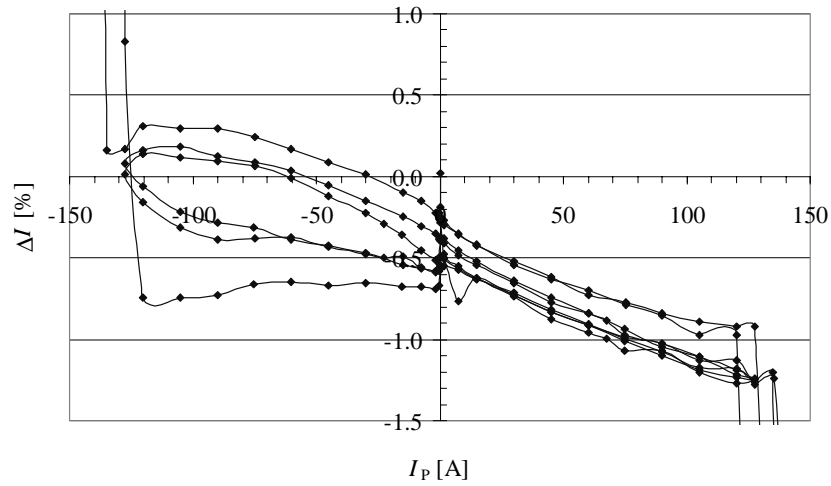
Figure 2.9   Percentage error of the output current in the measured range. The measured current was a DC current, repeatedly increased gradually to positive saturation level and decreased to negative saturation level. The secondary current was measured with a mA to μA-level multimeter.

2.2.3   AC measurements

Another experimental setup was arranged to explore the non-linearity of the transducer when a 50 Hz AC primary current was measured. In the primary circuit of the transducer 15 turns were again used. As the AC power supply, an Agilent 6812B AC power source/analyzer was used. The primary and the secondary currents were measured using FLUKE 89 IV true rms multimeters. Fig. 2.10 shows the percentage error of the output current as a function of the primary current I_P. The measured primary current was an AC current, repeatedly increased gradually to a peak level 90 A and decreased to zero level for two cycles. Fig. 2.11 presents current deviation from the instantaneous primary current value in the measurement range of the primary current I_P.
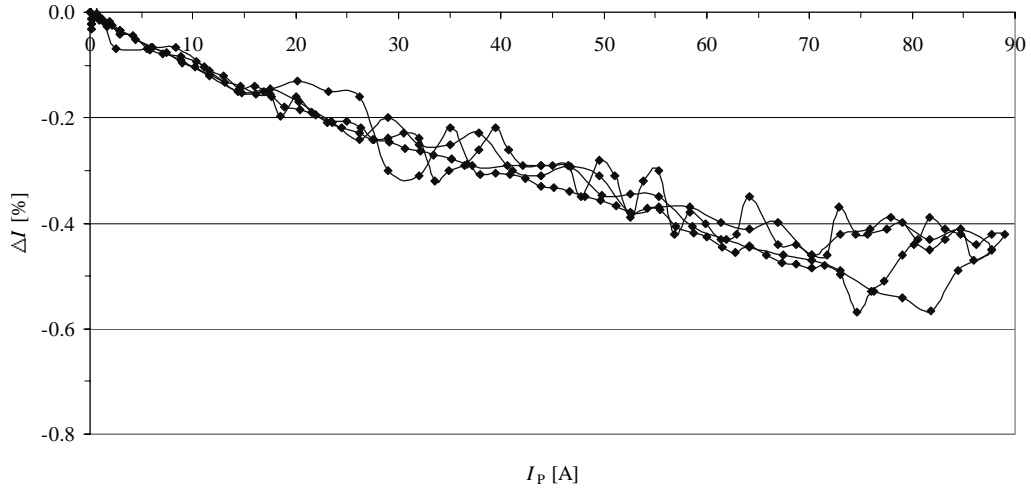
Figure 2.10 Percentage error of the output current as a function of the primary current I_P. The measured primary current was a 50 Hz AC current repeatedly increased gradually to peak level and decreased to zero level.
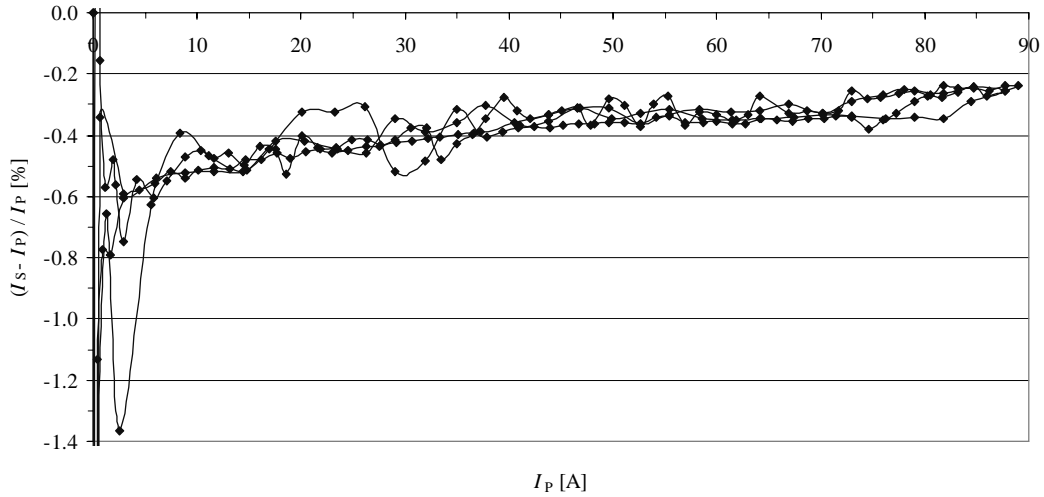

Figure 2.11 Current deviation from the instantaneous primary current value in the measurement range of the primary current I_P. The measured primary current was a 50 Hz AC current repeatedly increased gradually to positive peak level and decreased to zero level.

The experimental setup may not have been the most accurate one, but it still shows certain phenomena which may have an effect on the performance of the electric drive. From Fig. 2.10 it can be seen that a gain error appears, as in DC measurements. By comparing the current deviation against instantaneous primary current to be measured, as in Fig. 2.11, it can be seen that the percentage error increases when the measured current decreases. This may disturb the perform-

ance of drives when the motor's rated current is much smaller than the rated current of the inverter.

The experiments on the current measurement non-linearity illustrate the existence of the offset and gain errors of a current transducer. Moreover, a hysteresis-like error appears. The existence of the hysteresis-like error in practice would apparently be limited to continuous overload situations, where the measured current is close to the maximum value of the sensor range or exceeds it. Undersized current transducers would end in the same result.

Measurement results on the effect of offset and gain errors on torque ripple were easily arranged on the experimental equipment system consisting of a laboratory version of an ACS-600 frequency converter, a PMSM and a DC motor as the load (Laurila 2002a). Verifying the simulation results on non-linear current measurement errors was, however, infeasible on the existing setup.

2.3   Voltage measurement errors

In addition to stator currents, stator voltages are of interest in estimating stator flux, as in Eq. (1.12). The measurement of stator voltages is usually accomplished by measuring the DC-link voltage and by estimating the voltage according to the known switching states of the converter. Since the Hall effect voltage transducers used for the DC voltage measurement are based on the same principle as their current transducer counterpart, similar errors are possible. Typical accuracy of Hall effect closed loop voltage transducers is ± 1 % and for linearity ± 1 %. The measurement bandwidth of Hall effect voltage transducers is typically several kHz and the response time varies between 10 … 100 µs. The response time of the Hall effect voltage transducers is longer than the response time of the Hall effect currents transducers, because the primary circuit of the voltage transducers is made with a winding having a high number of turns. The response time depends on the L/R time constant of the primary circuit (primary winding inductance and primary resistance). This response time is rather slow if it is compared, e.g., to the minimum pulse length of typical DTC-inverters, 25 µs. The DC intermediate circuit voltage is measured in typical inverters and in those applications this bandwidth seems to be large enough. A resistive divider is also a common method to measure the DC-link voltage. With the resistive di-

vider, the accuracy is defined by the accuracy of the resistances and their temperature dependencies.

2.4   Non-ideal power electronic switches

In addition to the voltage measurement error due to the voltage transducer, another source of error is present in the voltage estimation due to the non-idealities of power electronic switches. In the ideal case the voltage vector u_s in (1.12) is formed by the DC-link voltage U_{DC} and the switching states S_A, S_B and S_C. The switching state can be either 1 or 0. State 1 means connection to the positive potential and state 0 means connection to negative potential. The voltage vector can be written as

$$
u_s(S_A, S_B, S_C) = \frac{2}{3} U_{DC}\left(S_A e^{j0} + S_B e^{j\frac{2\pi}{3}} + S_C e^{j\frac{4\pi}{3}}\right) - \\
\frac{2}{3}\left(u_{a,loss} e^{j0} + u_{b,loss} e^{j\frac{2\pi}{3}} + u_{c,loss} e^{j\frac{4\pi}{3}}\right)
$$
, (2.35)

where $u_{a,loss}$, $u_{b,loss}$ and $u_{c,loss}$ take into consideration the threshold voltage, the conducting state voltage losses and the switching delay during switch commutation (Kaukonen 1999). In order to avoid short-circuit of two power switches of a leg, a dead-time during the switch commutation has to be used. This dead-time generally has little effect on the performance of the system. However, in low speed region, it can cause system unstability (Li 1997).

Two different types of behaviour are observed, when there is an error in the measured DC-link voltage. The first is a constant stable error in the stator flux linkage magnitude and the second is an alternating unstable drifting of the stator flux linkage. The measured DC-link voltage is expressed as

$$
U_{DCmeas} = (1 - k_{gain})U_{DC} + \Delta U_{DCoffset} = U_{DC} + \Delta U_{DC},
$$
 (2.36)

where U_{DC} is the actual DC-link voltage, k_{gain} is the gain coefficient and $\Delta U_{DCoffset}$ is the offset voltage. ΔU_{DC} is the total measuring error at a certain time instant.

At low speed, the voltage drop in the converter can be higher than the emf voltage, constituting a dominant disturbance. Typical voltage drop in a modern 1200 V IGBT switch may be e.g. 3 V. When the current is running through at least two transistors a 6 V voltage drop in the power switches may be present. In a 400 V 50 Hz motor drive the line-to-line back emf of an induction motor rotor circuit is 6 V at about 0.75 Hz rotor rotating frequency. It is easy to see that the converter voltage drop may be significant at low speeds.

2.4.1   Dead-time

In an ideal situation, the states of two switches in an inverter leg are allowed to change simultaneously from on to off and vice versa. In practice, any type of power electronic switch has finite turn-on and turn-off times. The turn-on of the other switch in the inverter leg has to be delayed by a dead-time (blanking time, lock-out time) to avoid a shoot through (short circuit) through the leg (Mohan 1995). The dead-time counts from the time instant at which one semiconductor switch in a leg turns off and terminates when the opposite switch is turned on. The dead-time is determined as the maximum value of storage time plus an additional safety time interval. (Bose 1997.) The relatively long turn-off time of IGBTs is dominated by the time taken to sweep out the minority charge carriers in the n⁻ layer.

Due to the presence of the dead-time, the amplitude of the output voltages of the inverter will be reduced and distorted. Since both switches in each leg are in the off-state during the dead-time duration, the output voltage is dependent on the direction of the output current. For example, if in an inverter leg, as in Fig. 2.12, the upper switch (S1) and lower switch (S2) are not conducting, then either diode D1 (across S1) or diode D2 (across S2) conducts, depending on the sign of the stator phase current. The voltage deviation due to the dead-time opposes the current flow in either direction.
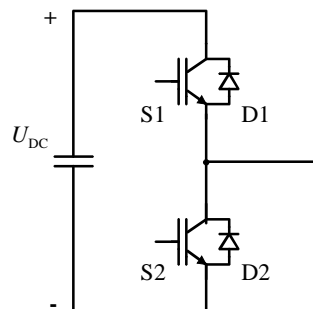

Figure 2.12 Basic configuration of one phase leg of an inverter.

The voltage error in the output voltage of one phase due to the dead-time and the voltage drops of the switching devices is

$$U_{a,dead} = U_{dead} \cdot \text{sgn}(i_a) \,, \tag{2.37}$$

where

$$\text{sgn}(i_a) = \begin{cases} 1 & : \ i_a > 0 \\ -1 & : \ i_a < 0 \end{cases} \quad \text{and} \tag{2.38}$$

$$U_{dead} = \frac{t_{dead} + t_{on} - t_{off}}{T_s} \cdot (U_{DC} - U_{sat} + U_d) + \frac{U_{sat} + U_d}{2} \,. \tag{2.39}$$

U_{sat}, U_d, t_{dead}, t_{on}, t_{off} denote the saturation voltage drop of the active switch, forward voltage drop of the freewheeling diode, dead-time, turn-on time and turn-off time, respectively. Similar output voltage errors can be defined for the other two phases. The amplitude of the disturbance voltages in the rotor reference frame is a function of U_{dead} in (2.37), which can be considered as a time varying value depending on the operating conditions. The switching times of the switching devices vary with operating conditions such as the DC link voltage and currents. The voltage drops of the devices also vary with the operating conditions. (Kim 2003.)

The distortion of the inverter output voltage affects stator currents, which result in torque pulsations. The deviation of the output voltage has a square wave waveform after low-pass filtering (Murai 1987). The square wave is known to have 5th and 7th harmonics. If the fundamental flux wave rotates counter-clockwise the magnetomotive force (mmf) of the 5th current harmonic rotates clockwise, while the 7th current harmonic mmf rotates counterclockwise at the same speed (Antić 1994). As a result a torque ripple at the 6th harmonic of the fundamental frequency appears (Choi 2000; Chen 2000). The result is similar as with the traditional six-step inverter, which has a hexagon shaped stator flux linkage plot. The DTC also results in a hexagon shaped stator flux linkage with wide hysteresis bandwidths of flux and torque.

2.5   Time delays

The DSP-based controller reads in the torque and flux references, the DC link voltage and two line currents at the beginning of each sampling period. The DSP needs a certain amount of time to execute the entire control algorithm. This time, together with the time required for over-current protection, determines the minimum value of the sampling period. Owing to the computational time required, a time delay period is present between the sampling instant and the commutation of the inverter switches. As a consequence, the instantaneous values of the stator flux magnitude and torque may exceed the upper and lower band limits of the prefixed hysteresis bands. On account of these considerations it appears that, even with a zero band width, the stator flux and torque will be affected by a ripple. (Idris 2000.)

2.6   A/D conversion

One contributor to the sensor inaccuracy is the quantization error. During the A/D conversion process, when the analogue signal from the sensor is changed into digital bits, an amplitude quantization error occurs (Cheok 2002). The total number of analogue combinations is 2^n for an n-bit A/D -converter. A one bit error means a current measurement error of

$$\Delta i_{AD} = 100 - \frac{2^n - 1}{2^n} \cdot 100 \ [\%] \quad . \tag{2.40}$$

Quantization errors for some n-bit A/D -converters are presented in table 2.1. Typical usage is 10-bit in the current measurement of adjustable speed drives.

Table 2.1 Quantization errors for some n-bit A/D -converters.

n	Δi_{AD} [%]
8	0.391
10	0.098
12	0.024
16	0.0015

2.7 Stator resistance estimation error

Stator resistance linearly depends on the stator temperature (Andreescu 2002). The actual value of the stator resistance varies due to the winding temperature (Holtz 2002). The influence of the resistive voltage drop becomes more dominant as the temperature increases. In DTC-drives the stator flux linkage estimate gets wrong values, but the error created this way is stable and no torque ripple is generated (Kaukonen 1999).

2.8 Reflected waves and cable length

Reflected wave transient voltages that result from fast IGBT voltage source inverters and long cable length have a consequence on currents to be sensed. According to the transmission theory, a wave (called e) that travels along a cable will behave at certain ways at the end of the cable, dependent on the match (or mismatch) of the cable intrinsic impedance Z as compared with the impedance closing the cable at its end R_0. In the case of a mismatch, a reflection will take place. The reflected wave is here e'. The resulting total voltage at the end of the cable is

$$e_0 = e + e' \; , \tag{2.41}$$

where

$$e' = \frac{R_0 - Z}{R_0 + Z} e \;\; \text{and} \tag{2.42}$$

$$e_0 = \frac{2R_0}{R_0 + Z} e \; . \tag{2.43}$$

The reflected wave magnitude e' and total voltage e_0 as function of R_0/Z are presented in Fig. 2.13. Three cases deserve to be mentioned: shorted cable, matching R_0 and open circuit, as in Table 2.2. (Persson 1992.)
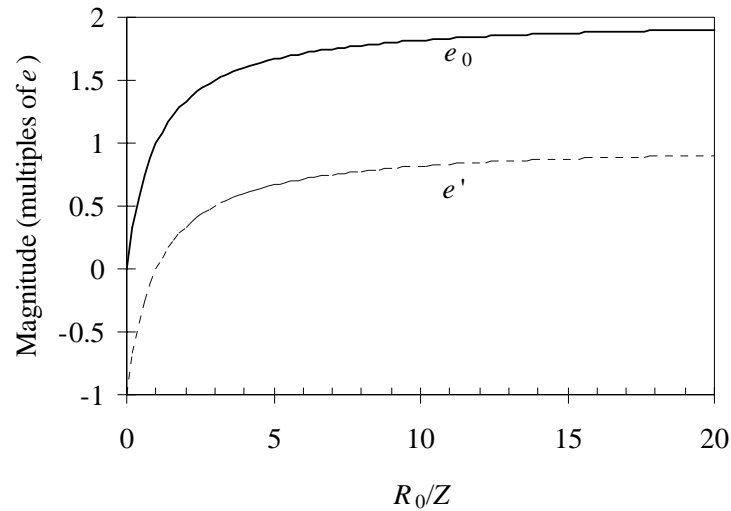
Figure 2.13 Reflected wave e' and resulting total voltage at the end of the cable e_0 as function of R_0/Z. R_0 is the impedance closing the cable and Z is the cable impedance.

Table 2.2 Three cases and corresponding reflected waves e' and total voltages e_0 at the end of the cable, (Persson 1992).

	E	e'	e_0
shorted cable	1	-1	0
matching R_0	1	0	1
open circuit	1	1	2

The resulting high frequency voltages oscillate heavily at the motor input, whereas current oscillation is higher at the inverter output. The current wave is in relation to the voltage wave by the cable impedance. The current transducers are normally located at the inverter output. The control algorithm of the drive makes control decisions based on the current and voltage measurements. With long cables the current oscillation may last longer than the time between control decisions, so that the current oscillation may disturb the drive control. (Tarkiainen 1999.)

Pankau (1999) claimed that the cable oscillation frequency periodically disturbs the null condition of the current transducer core, which momentarily saturates the push-pull amplifier. The control circuitry then has difficulties to null the core when the dwell time between PWM pulses becomes less than the relaxation time of the sensor. Although the transient damps out, a more complex excitation, such as a double pulse condition (Kerkman 1997), presents a condition

where the sensor's flux is not nulled. Under these conditions the feedback current signal may become distorted and drift (Leggate 1998). Kerkman (2003) listed the distortion from traveling wave currents as one of the errors of current sensor and its feedback. The other listed errors were ground bounce, signal range limitations, A/D quantization, polarity discrimination and phase delay. The accumulation of these effects often exhibits itself as a varying offset.

The high frequency component of the reflected current waveform could result in excessive core loss and therefore excessive heating of open-loop Hall effect current sensors (Persson 2002). Since the Hall element is rather small and the Hall voltage is temperature dependent, heating may cause offset voltage variation.

2.9   Summary

In this chapter an analysis of the effect of the frequency converter's non-idealities on the torque ripple is given. The chapter gives a view on the wide variety of speed and torque ripple producing factors. Errors in the measured stator current and estimated voltage signals cause an error in the estimated stator flux linkage and torque estimates and, further on according to the characteristic properties of the control system, an error in the torque control. The effect of current measurement errors on the torque ripple is analysed in more detail than some other factors, as the current measurement forms a significant information source in the control of modern speed sensorless drives. The effect of offset and gain errors in the current measurement on the torque ripple are analysed. Even some experimental results to define the shape of the non-linearity are given, according to which, an hysteresis-like error is found. The inaccuracy of the current measurement may increase due to the reflected wave transient voltages that result from voltage source inverters and long cable length.

3 TORQUE RIPPLE SIMULATION MODEL

The simulation model of the direct torque controlled PMSM drive is created in MATLAB[®] 6.5/Simulink[®]. The simulation model consists of an inverter block, including speed control and optimum switching table (DTC), PMSM and load blocks, Fig. 3.1. To emphasize the torque ripple producing elements of the converter an ideal model for the permanent magnet synchronous motor was used. The equations of the model were described in chapter 1.5. Also the load and power electronic switches are considered as ideal, whereas the current measurement of the inverter is considered less ideal.
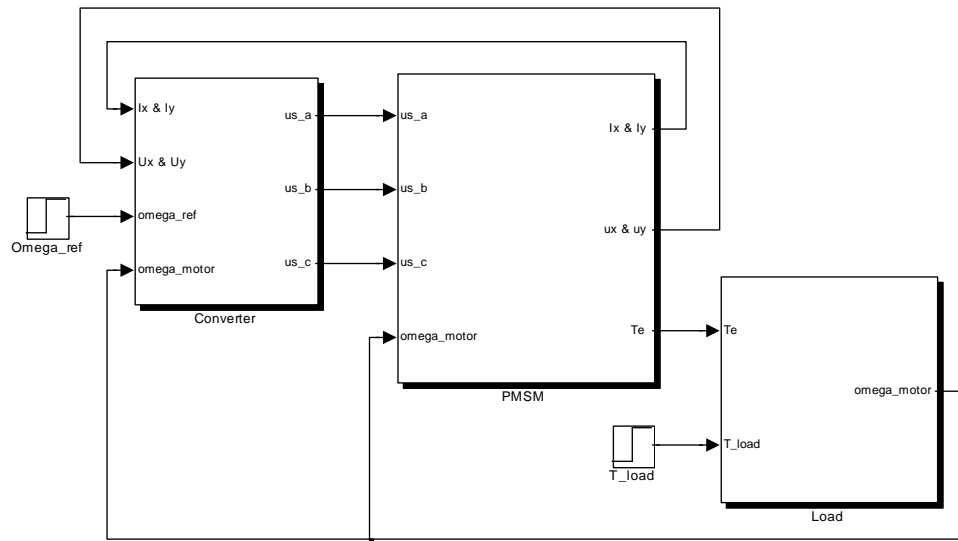
Figure 3.1 Inverter, control system and PMSM are modeled in MATLAB[®] 6.5/Simulink[®].

3.1 Offset and gain errors

Current measurement errors can cause torque ripple mainly in two ways. If the current measurement error type is an offset error, a torque ripple component at the fundamental frequency f_1 appears, Fig. 3.2. The other current measurement error type is the gain (scaling) error, which produces a torque ripple component at twice the fundamental frequency ($2 \cdot f_1$), Fig. 3.3. These low order harmonics can be harmful if they lie at the mechanical resonances of the system.
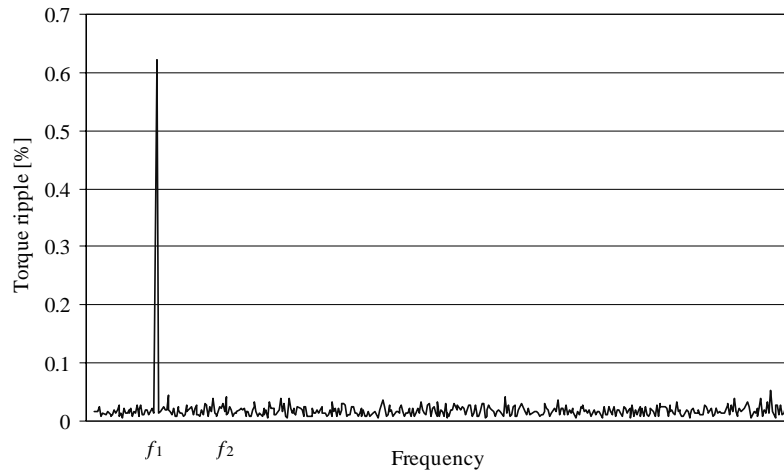
Figure 3.2   Simulated torque ripple due to 0.5 % offset error in current measurement of phase a. Torque ripple appears at the fundamental frequency f_1.
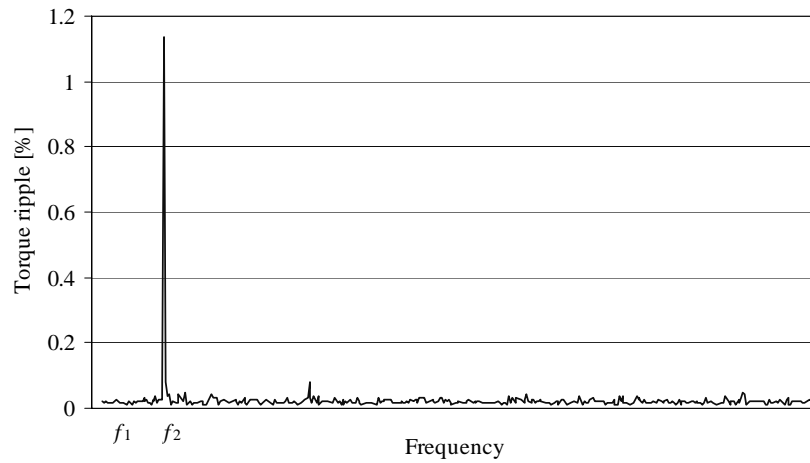
Figure 3.3   Simulated torque ripple due to 2 % gain error in current measurement of phase a. Torque ripple appears at $2 \cdot f_1$.

3.2 Non-linearity

In the following simulations, four different shapes of non-linearities have been used at the current measurement of two motor phase currents (Laurila 2003), Fig. 3.4. The non-linearities are magnified for visibility in Fig. 3.4. Case 1 presents a non-linearity shape similar to the curve presented in Fig. 2.1 c). Fig. 3.5. illustrates the simulated torque in case 1 and the resulting

torque ripple spectrum is shown in Fig. 3.6. In case 2 the non-linearity is similar to case 1 on positive side, but the negative side of the transfer function is mirrored on the other side of the ideal curve. The simulated torque and torque ripple spectrum in case 2 are shown in Fig. 3.7 and Fig. 3.8, respectively. In case 3, the non-linearity error based on (Cristaldi 2001) has a hysteresis-like error with most significant error values near the zero crossing point. The simulated torque is shown in Fig. 3.9 and the corresponding torque ripple in Fig. 3.10. In case 4, a hysteresis error of ±1 % is used. The simulated torque is given in Fig. 3.11 and the corresponding torque ripple in Fig. 3.12. The simulation data of the current non-linearities are given in Appendix D.
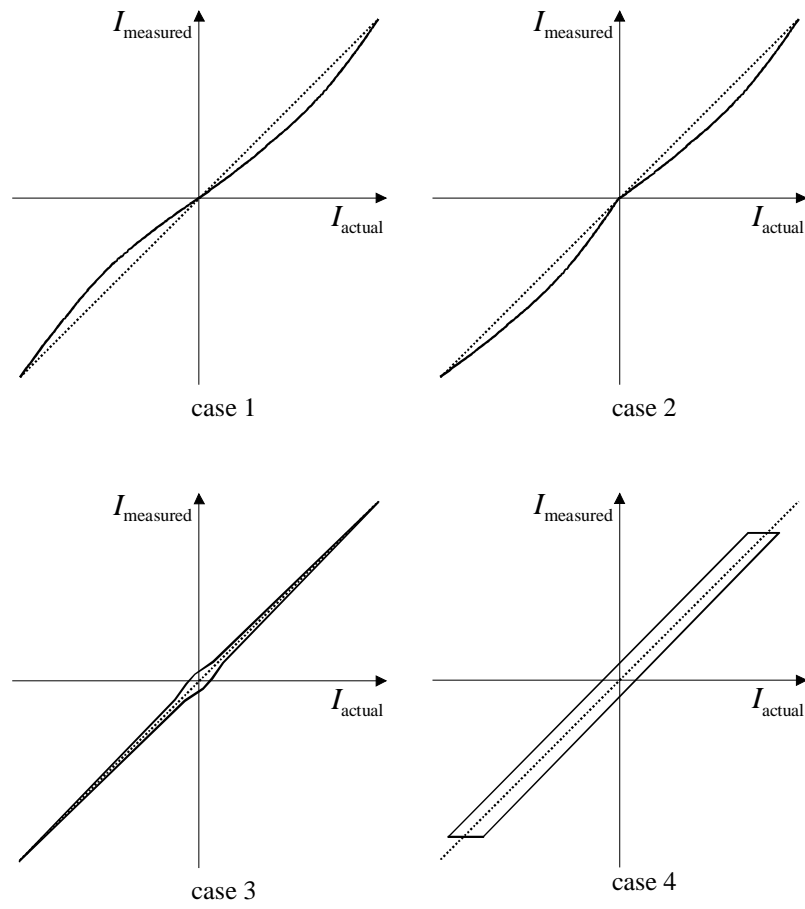
Figure 3.4 Four different shapes of non-linearity used at the current measurement simulations.
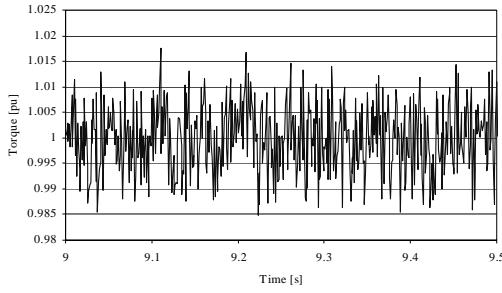
Figure 3.5 Simulated torque. Non-linearity (case 1) <1% is used in the current measurement of two phases.
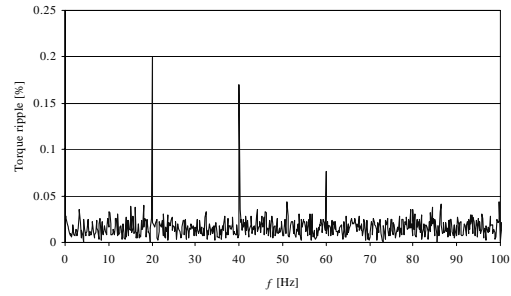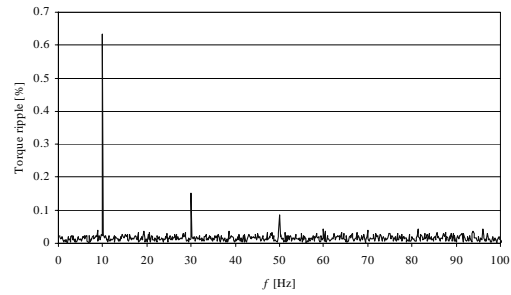

Figure 3.6 Torque ripple. Harmonic components appear at 2nd, 4th and 6th harmonic frequencies. $f_1 = 10$ Hz.

The torque ripple generated in case 1 contains even harmonics of the order 2nd, 4th and 6th, Fig. 3.6. The non-linearity waveform in case 1 is in some degree similar to the gain error waveform, except at the maximum ends of the range. The 2nd harmonic results as the dominating one as with the gain error.
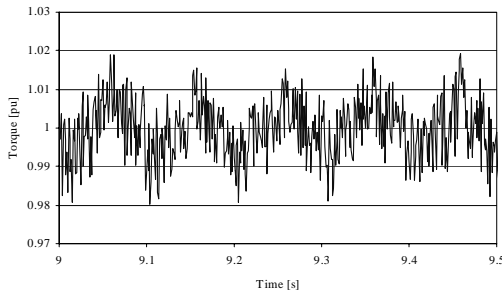
Figure 3.7 Simulated torque. Non-linearity (case 2) <1% is used in the current measurement of two phases.

Figure 3.8 Torque ripple. Harmonic components appear at 1st, 3rd and 5th harmonic frequencies. $f_1 = 10$ Hz.

In case 2 the torque ripple contains odd harmonics of the order 1st, 3rd and 5th, Fig. 3.8. The non-linearity waveform in case 2 is similar to the offset error waveform, except at the origin. The 1st harmonic is the dominating one as with the offset error.
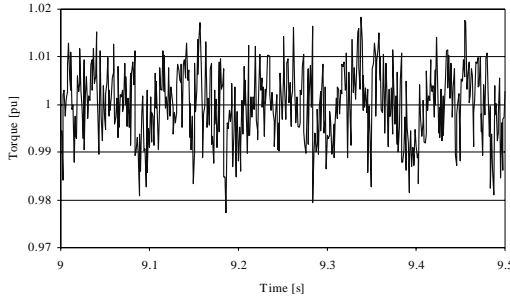
Figure 3.9 Simulated torque. Hysteresis-like non-linearity (case 3) <1% is used in the current measurement of two phases.
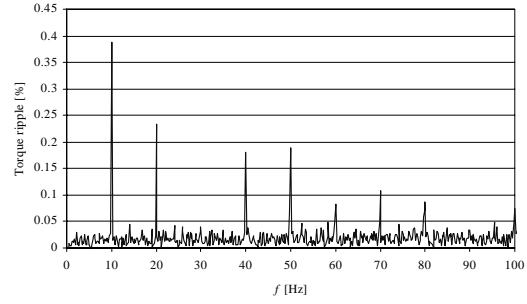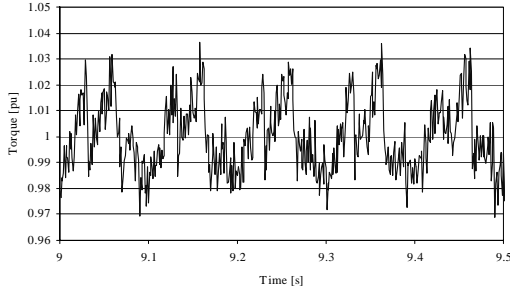
Figure 3.10 Torque ripple. Harmonic components appear at 1st, 2nd, 4th, 5th, 6th, 7th and 8th harmonic frequency. $f_1 = 10$ Hz.

The non-linearity in case 3 results in torque ripple at 1st, 2nd, 4th, 5th, 6th, 7th and 8th harmonic frequency, Fig. 3.10. The non-linearity in case 4 results in torque ripple at the first ten harmonics of the fundamental frequency 10 Hz in the considered frequency domain below 100 Hz, Fig. 3.12.

Figure 3.11 Simulated torque. A hysteresis error of 1% is used in the current measurement of two phases.
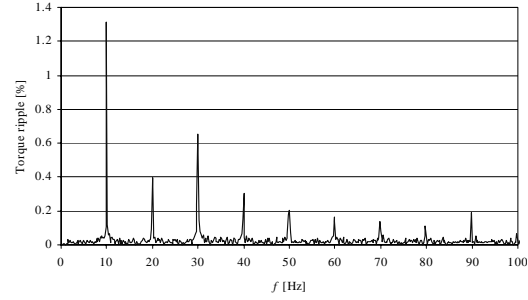
Figure 3.12 Torque ripple. Harmonic components appear at integer multiples of the fundamental frequency $f_1 = 10$ Hz.

In practice all of the cases discussed above are not present. According to our experiments, the non-linearity case 4 (the hysteresis error) appears to be the most relevant one. The case 4 was repeated with different hysteresis values between the range 0.1 … 1.0 %. The torque ripple at ten first harmonics due to different hysteresis error values in the current measurement of two phases is shown in Fig. 3.13. The hysteresis error produces torque ripple at integer multiples of the fundamental frequency. The most significant harmonics are the 1st and the 3rd harmonic torques.
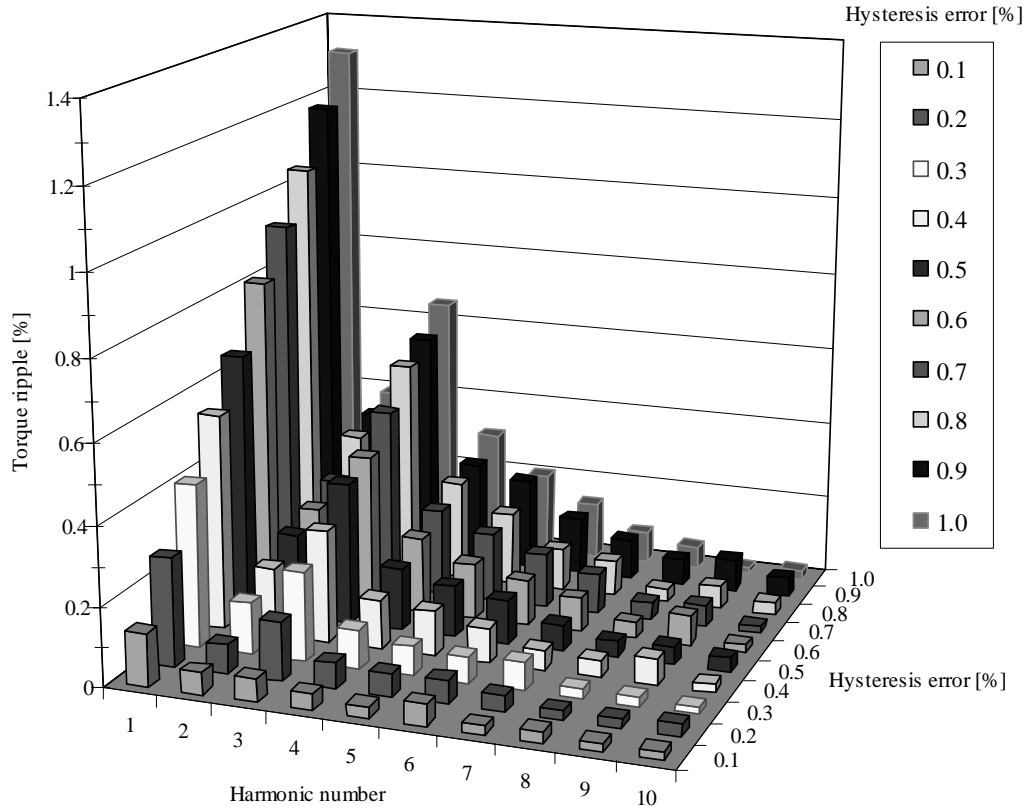
Figure 3.13 Torque ripple at the ten first harmonics due to different hysteresis error values in the current measurement of two phases. The first and the third harmonic torque ripples have the most significant magnitudes.

3.3   Coupling of the simulation models of the electric drive and the mechanical load

The Simulink models of the converter and PMSM were coupled to the simulation model of the mechanical load created in a multi-body simulation software ADAMS, which provides functional virtual prototyping tools for building, testing, reviewing, and improving mechanical systems before committing to physical prototypes. The advantage of ADAMS vs. Matlab is that dynamic mechanical systems are described geometrically, so the derivation of complex equations of motion is eliminated (Hirvonen 2003).

The procedure, how to couple converter and motor models from Simulink to the mechanical load model in ADAMS, is presented in Fig. 3.14. The Simulink model is first compiled to C

language by the Real Time Workshop Embedded Coder. Then the code is manually edited to be compatible with ADAMS. ADAMS, being the main program, uses the C language model as a subroutine. In this simulation method the user interface is in ADAMS and the converter and the motor models can be parametric for user convenience.
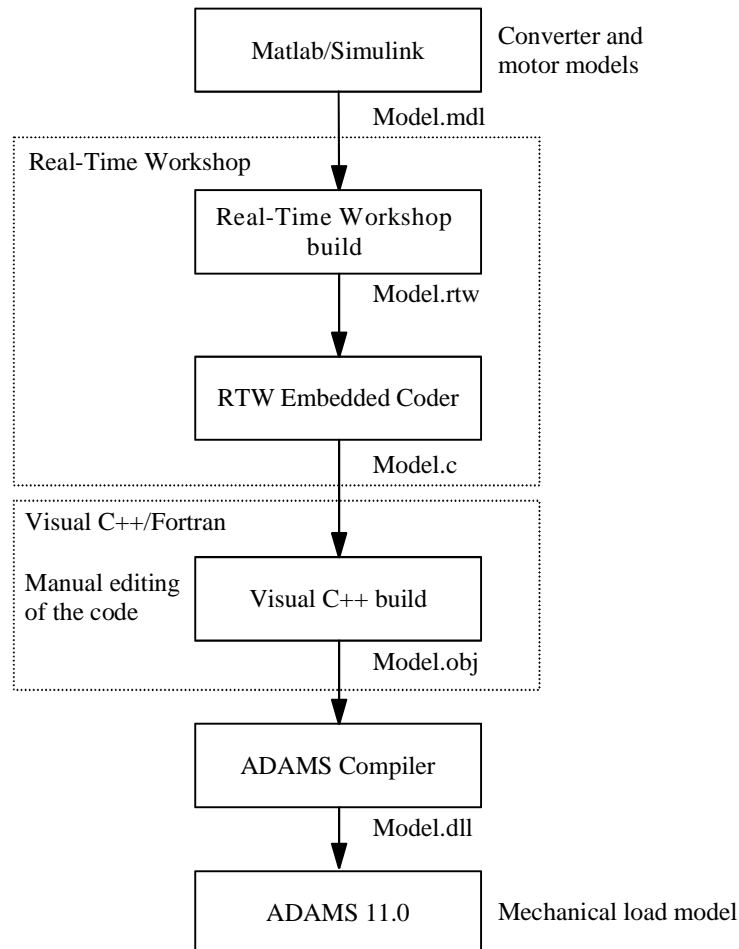

Figure 3.14 Procedure to couple the converter and the motor models from Simulink to the mechanical load model in ADAMS. After compiling the Simulink model to C language model, ADAMS uses the C language model as a subroutine.

A comparison of the simulated torques in Simulink and ADAMS is shown in Fig. 3.15. The mechanical load modelled is a simple cylindrically shaped inertia mass.
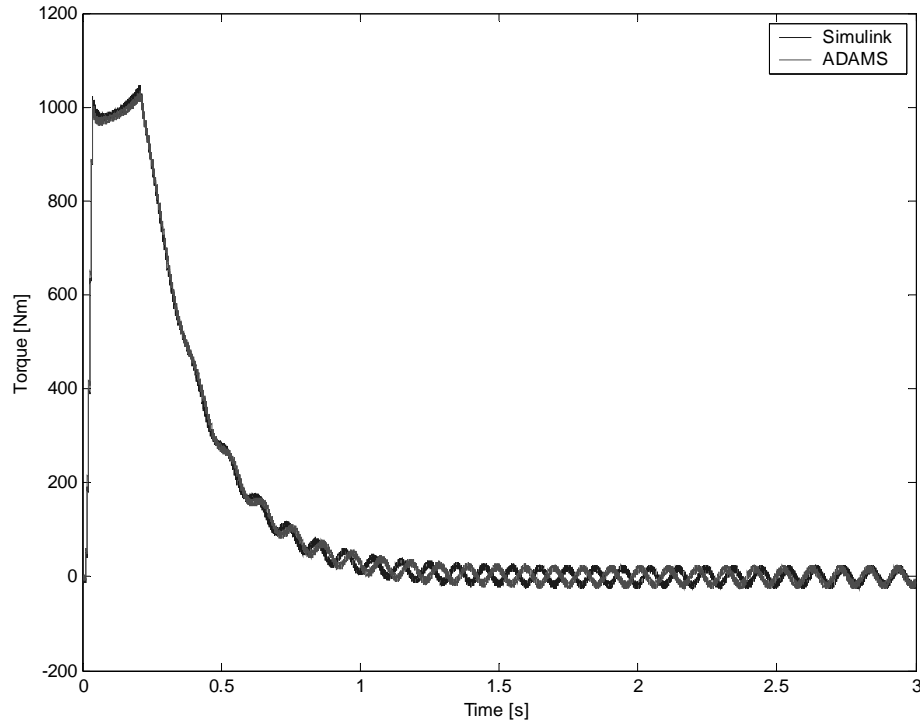
Figure 3.15 Comparison of simulated torques calculated in Simulink and in ADAMS. The stator reference frequency is 10 Hz and the current measurement offset is –2 % in one phase.

The amplitudes and overall waveforms of the torque ripple are similar in both Simulink and ADAMS simulations, but slight difference is observed in the frequency of the ripple during the settling of the torque. The time taken on the simulation of Fig 3.15 in ADAMS was 4 min. 45 s on a PENTIUM IV, (1.8 GHz, 1 GB RAM) with a 12.5 µs time step and 3 s as the simulated time. This time taken on the coupled simulation can be seen acceptably short, but it has to be remembered that the model of the mechanical load was quite simple. With more complex mechanical load models the time taken on the simulation easily extends to several hours. This limits comfortable usability of the coupled simulation model for rapid simulations on complex mechanical loads, the modelling of which actually is the advantage of ADAMS vs. Matlab. The cause of the long simulation time is the shortest time step of the model (12.5 µs) that is constrained to be used also for the mechanical load. Such a short time step is informatively needless for the analysis of the mechanical load. Further development of the time stepping is needed to reduce the simulation time of the coupled simulation in ADAMS.

3.4 Summary

In this chapter a torque ripple simulation model of the direct torque controlled permanent magnet synchronous motor drive was introduced. The simulation model of the frequency converter included non-idealities, such as the offset, gain and non-linearity errors in the current measurement. Simulation results of the torque ripple were given. The offset error produced torque ripple at the fundamental frequency and the gain error produced torque ripple at the 2nd harmonic frequency. The non-linearity of the current measurement produced torque ripple at various harmonic frequencies, which were dependent on the shape of the non-linearity. Selected four shapes of non-linearity produced torque ripple at the different cases as follows: case 1) 2nd, 4th, 6th , case 2) 1st, 3rd and 5th, case 3) 1st, 2nd, 4th, 5th, 6th, 7th and 8th, case 4) 1st to 10th harmonic frequencies.

A procedure to create a coupled simulation model of the electric drive and the mechanical load was introduced. The frequency converter and motor parts of the Simulink model described earlier were coupled to a multi-body simulation software ADAMS. A comparison of the simulated torques in Simulink and ADAMS was given. The coupled electromechanical simulation model was found to work satisfactorily with a simple cylindrically shaped inertia mass. The coupled simulation model can be used with more complex mechanical models, such as cardan shafts, at the expense of longer simulation times.

4 DETECTION AND COMPENSATION OF CURRENT MEASUREMENT ERRORS

The speed and torque ripple at the first and second harmonics of supplying frequency have been proven to result from the offset and gain errors in the current measurement. The detection of the speed and torque ripple is of primary importance for defining a suitable compensation for the current measurement errors. Modern PMSM drives do not necessarily need a speed sensor and a torque meter is even more rarely used. A method to reduce the speed and torque ripple caused by the current measurement errors is proposed in the following. The compensation method can be implemented by detecting the speed ripple from measured or estimated speed.

4.1 Speed feedback

Although the trend of modern electric drives is towards speed sensorless drives, a speed feedback is still used in applications such as elevators, rolling mills and master drives of paper machines. In the case of speed feedback from a speed measurement is used, the detection of speed ripple is simple. The amplitude of a selected harmonic component of the speed signal is calculated by discrete Fourier transform (DFT) as a function of time, Fig. 4.1. In the case of the offset error, the amplitude of the first harmonic component of the supplying frequency is calculated from the speed signal $\omega(t)$. The calculation procedure is executed continuously in almost real-time. The output is delayed for one period of the fundamental frequency.
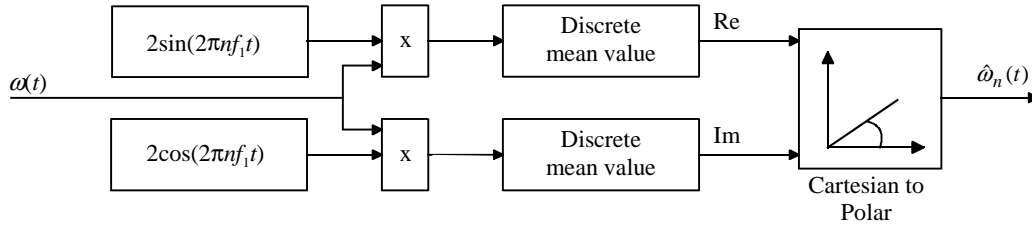

Figure 4.1   The calculation of the amplitude $\hat{\omega}_n(t)$ of the selected harmonic component of the speed signal $\omega(t)$ as a function of time. n is the number of the selected harmonic ($n = 1$ for offset error and $n = 2$ for gain error) and f_1 is the fundamental frequency.

4.1.1 Offset error compensation

The method to compensate offset errors in current measurement is introduced in Fig. 4.2. If the amplitude of the first harmonic component of the speed ripple $\hat{\omega}_1$ is greater than a threshold

value ω_{max}, a compensation routine is started. In practice only two currents are measured and probably no information is available about their offset error levels or signs. The compensation routine has to find suitable positive or negative corrections for two phases. This is implemented by running through a series of compensation alternatives, which is listed in Table 4.1. After the first harmonic speed ripple $\hat{\omega}_1$ is under the pre-defined threshold level ω_{max}, the compensation routine is halted and the last alternative remains valid. For both positive and negative corrections a look-up table defines the amount of correction for certain speed ripple levels.
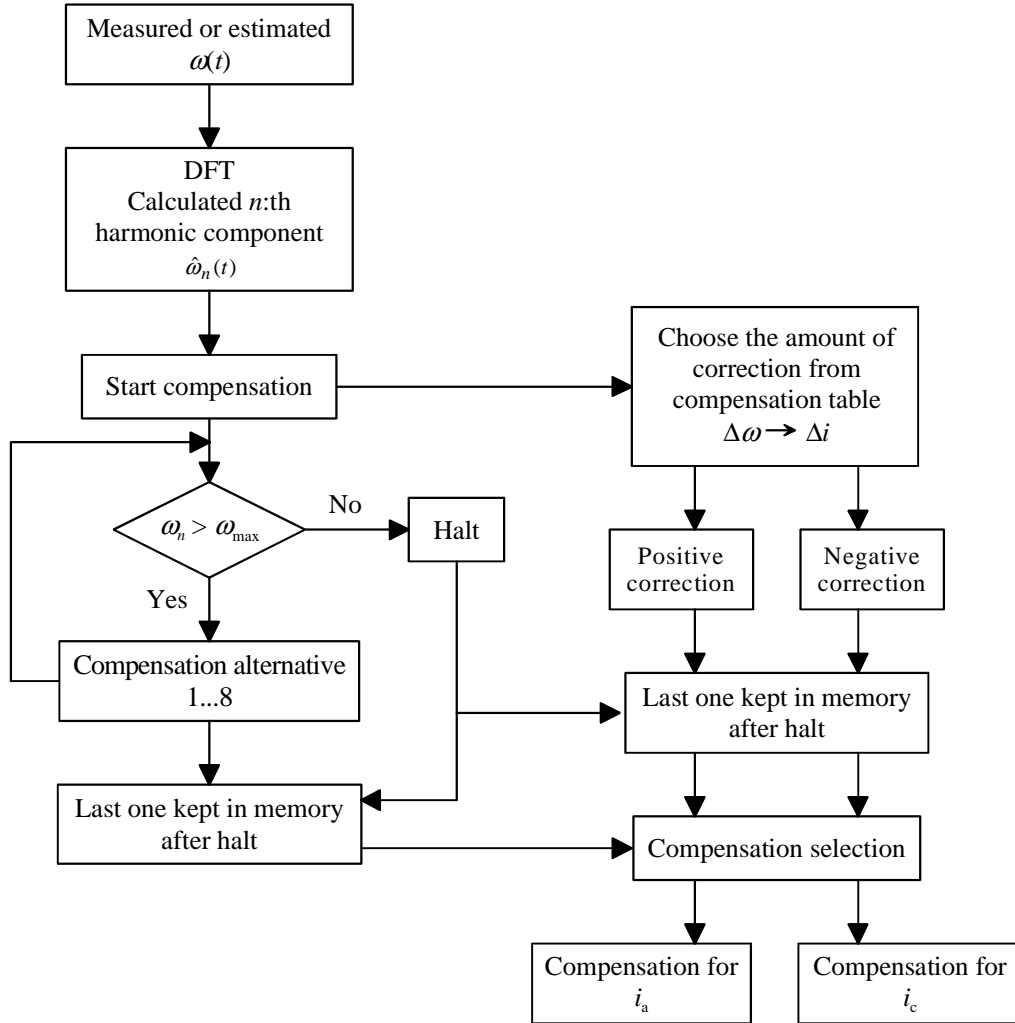

Figure 4.2   Compensation procedure of the offset errors in current measurement. The amplitude of the 1st harmonic component of speed ripple is calculated from the measured speed. A series of compensation alternatives is run through to find a suitable current compensation solution and limit the speed ripple under the desired level ω_{max}.

Finding the right compensation is implemented by running through a series of compensation alternatives. In the case of an offset error in the current measurement the number of compensation alternatives is nine, if two stator currents are measured, Table 4.1.

Table 4.1   Compensation alternatives $I_{a,corr}$ and $I_{c,corr}$ if two stator currents are measured. "-1" means correction to the negative direction, "0" means no correction, "+1" means correction to the positive direction.

$I_{a,corr}$	$I_{c,corr}$
-1	-1
-1	0
-1	+1
0	-1
0	0
0	+1
+1	-1
+1	0
+1	+1

The speed ripple compensation method presented is suitable not only for the direct torque control method and PMSM used herein, but also for other control methods and motor types. Moreover, this method can be implemented by modifying only the software.

Gain error compensation can be executed with nearly the same algorithm as with the offset error compensation in Fig. 4.2. Only slight modifications are needed. With gain error, the second harmonic component of the speed ripple is calculated ($n = 2$ in Fig. 4.1). A second look-up table is needed to define the amount of correction for the speed ripple levels at the 2nd harmonic frequency.

4.2   Speed sensorless drive

From the practical point of view the speed sensorless drive is, of course, the most important case. When no torque or speed sensors are used, the torque harmonic reduction by compensating the current measurement errors is based on knowledge extracted from the estimated speed.

It is obvious, that in DTC the stator flux linkage angular speed is somehow distorted by the current measurement errors when real torque ripple is established. A closed form for the stator flux linkage angular speed distortion is difficult to give but the drive simulations indicate clearly that the stator flux linkage vector angular speed is distorted when current measurement errors are present. If, say, the motor is producing torque in positive direction and the current error vector is pointing towards the co-ordinate system real axis, the control system is slowing down the stator flux linkage vector when it approaches the positive imaginary axis and vice versa when the stator flux linkage estimate is approaching the negative imaginary axis. These corrective actions are erroneous and caused by the current measurement error. Thus the angular speed variations can be obtained by utilizing the angular speed of the estimated stator flux linkage space vector. The amplitude knowledge of the estimated flux linkage speed may be used to indicate the presence of the errors caused by the current measurement. The estimated stator flux linkages ψ_{sx} and ψ_{sy} are thus used for the estimation of the speed,

$$\omega_{est} = \frac{d\left(\arctan\left(\frac{\psi_{sy}}{\psi_{sx}}\right)\right)}{dt} .$$

(4.1)

This is the derivative of the stator flux angle and gives an unfiltered speed signal, which is an input to a low-pass filter on the output of which the filtered speed signal is present. The estimated and filtered speed signal is then compared to the speed reference.

The amplitude of the speed ripple extracted from the estimated speed may differ from the speed ripple extracted from the measured speed. This depends on the filtering of the estimated speed. The phase difference due to filtering in the estimated speed signal is not a major factor, but the amplitude is of concern. Too much filtering will give smaller speed ripple amplitude than the actual measured one is. This will lead to insufficient compensation of the current measurement offset errors.

4.3   Torque feedback

In the special case of torque feedback from a torque meter, the same method as with the speed measurement can be used to compensate the current measurement errors. Again, from the meas-

measured torque the amplitudes of the first and second harmonic components of torque ripple are calculated by the DFT. If the amplitude of the first harmonic component of torque ripple is greater than a threshold value, the compensation routine is started. This time the look-up table for both positive and negative corrections of the current measurement error defines the amount of correction for certain torque ripple levels.

4.4 Calculation capacity

The compensation method needs calculation capacity for the discrete Fourier transform and the selection of the compensation alternative. The introduced method is tested with 1–2 ms time step for the speed signal input and is run with a 400 MHz PPC processor. The same processor is used for controlling the inverter with the DTC and for the current and voltage measurements. The duration of a time delay, t_{delay}, in the calculation of the discrete mean value is defined by the fundamental frequency f_1 and results in a number of samples

$$N = \frac{t_{delay}}{\Delta t} = \frac{1}{f_1 \Delta t} \, , \qquad (4.2)$$

where Δt is the sampling time. For example, a fundamental frequency of 5 Hz with 2 ms sampling time results in $N = 100$ samples.

In order to decrease the calculation capacity needed for the DFT in Fig. 4.1, some development of the calculation procedure could be prospective. For example, $\sin(x)$ and $\cos(x)$ functions generally require about ten times longer to calculate than a single addition or multiplication. Despite the fact that the calculation of $\sin(x)$ and $\cos(x)$ functions is needed, the compensation method is not found to limit the calculation capacity of the test equipment exhaustively.

4.5 Summary

In this chapter a method to detect and compensate current measurement errors was introduced. Detection of the current measurement error is based on the analysis of speed signal, which can be either measured or estimated. The amplitude of a selected harmonic component of the speed signal is calculated by discrete Fourier transform as a function of time. In the case of the offset error, the amplitude of the 1st harmonic component of the speed signal is monitored. If the am-

plitude of the 1st harmonic component of the speed ripple is greater than a threshold value, a compensation routine is started. The compensation method selects suitable positive or negative corrections for two phases. For both positive and negative corrections a look-up table defines the amount of correction. The compensation method is stopped after the amplitude of the first harmonic component of speed ripple is reduced under the required level. Compensation of the gain error can be implemented with similar procedure by monitoring the 2nd harmonic component of the speed ripple.

5   EXPERIMENTAL RESULTS ON TORQUE AND SPEED RIPPLE

The experimental results on electric drives are attained with the following setups. The first setup consisted of a commercial frequency converter with standard software, a permanent magnet axial flux synchronous motor and a DC motor as the load. The second setup consisted of another commercial frequency converter with the author made control algorithm, a permanent magnet synchronous motor and a DC motor as the load. Only offset and gain errors are approached since, in practice, these error types are the most common and important current measurement errors with respect to the drive torque quality. The test results also show that good drive performance will be found by compensating these two types of errors. The more complicated error types studied in the preceding chapters remain in theoretical level in this study.

5.1   Experimental setup 1

The first experimental equipment consisted of an ACS-600 frequency converter, an axial flux permanent magnet synchronous motor and a DC motor as the load, Fig. 5.1. The AFPMSM was driven without any speed or angle feedback with the ACS 600. The load was a DC motor driven by DCS 500 and coupled to the AFPMSM with two tangentially stiff clutches. The torque transducer was attached between the two clutches. Torque signals from the torque transducer were amplified (VibroMeter) and fed to a computer as analogue signals.
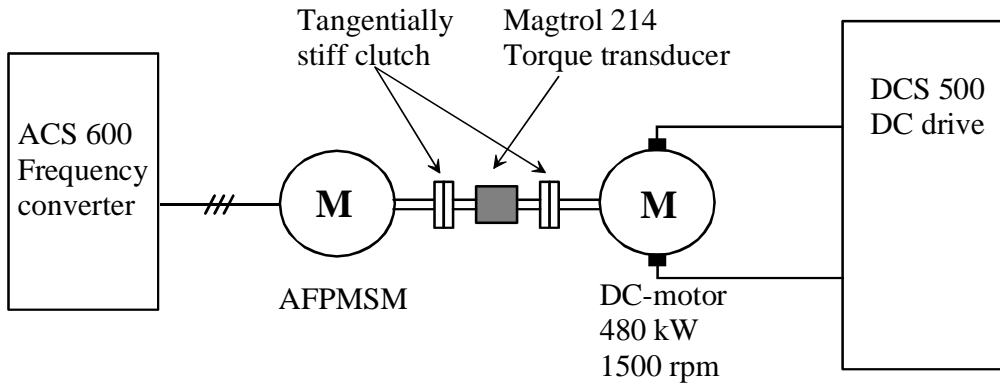

Figure 5.1   Experimental setup 1: ACS 600 frequency converter, AFPMSM as the test motor and a DC-motor as the load. Torque signals from the torque transducer (Magtrol 214, 200 Nm) were amplified (VibroMeter) and fed to a computer as analogue signals.

In the ACS 600 software the offset and gain parameters of the current measurement have been varied in one phase in order to obtain their effect on torque ripple. The experiments showed that

after normal identification run, the offset and gain corrections were not optimal. Torque ripple was found at certain frequencies, indicating that the offset and gain errors were still present. Therefore, the correction parameters were adjusted manually in order to find the minimum torque ripple at the first and second harmonic frequencies.

5.1.1   Offset error

The torque was measured with different offset parameters of current measurement in one phase. Fig. 5.2 illustrates measured torque behaviour with an offset error 0.5 % in the current measurement of phase A. The magnitude of torque ripple with 0.5 % offset error is given in Fig. 5.3. A significant torque ripple appears at the fundamental frequency f_1. The effect of different offset values on the first harmonic component of torque is shown in Fig 5.4.
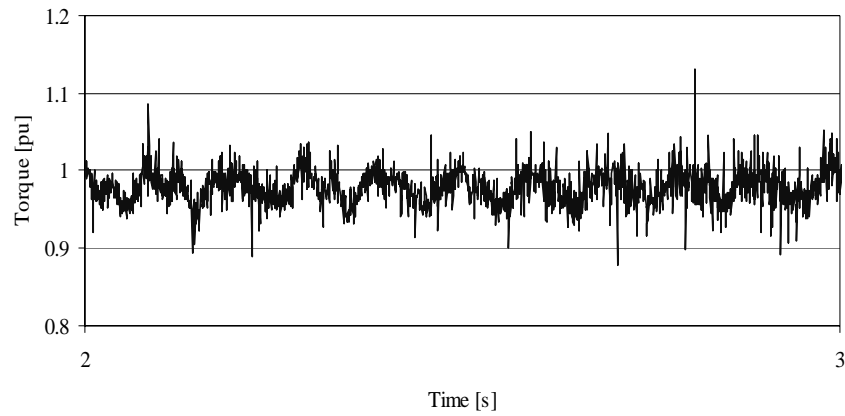
Figure 5.2 Measured torque. The offset error is 0.5 % in current measurement of phase a.
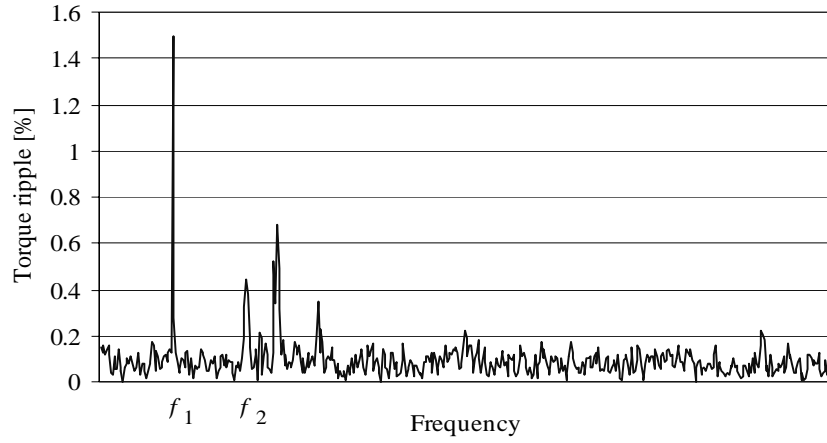
Figure 5.3 Torque ripple due to 0.5 % offset error in the current measurement of phase a. The highest torque ripple component appears at the fundamental frequency f_1.
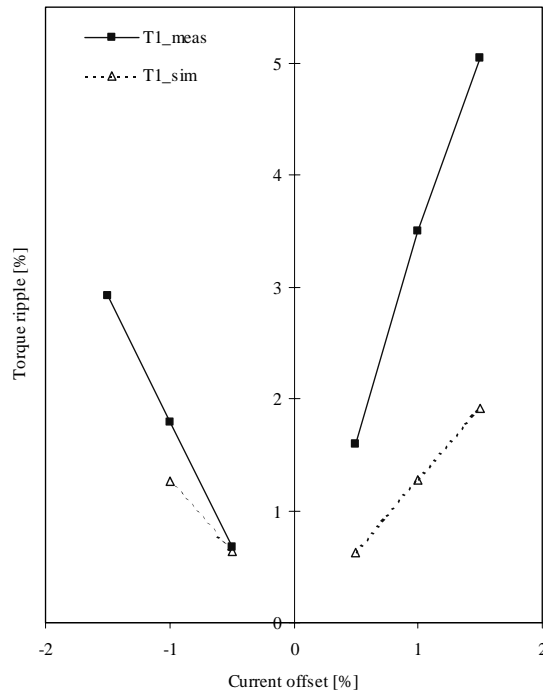

Figure 5.4 Torque ripple due to offset error in the current measurement of phase a. The values of measured and simulated first harmonic components of torque are given.

The difference between the measured and simulated values is quite large. The measured values are larger than they should theoretically be. The differences are, most likely, dependent on the mechanical resonance frequencies of the experimental setup. The same statement is apparently valid for the results of Fig. 5.7, too.

5.1.2 Gain error

The torque was measured with different gain parameters of current measurement in one phase. Fig. 5.5 shows the measured torque with a gain error of 2 % in current measurement of phase A. The magnitude of the torque ripple with 2 % gain error is given in Fig. 5.6. The most significant torque ripple appears at f_2, twice the fundamental frequency f_1. The effect of different gain values on the 2nd harmonic component of torque (T2) is illustrated in Fig 5.7.
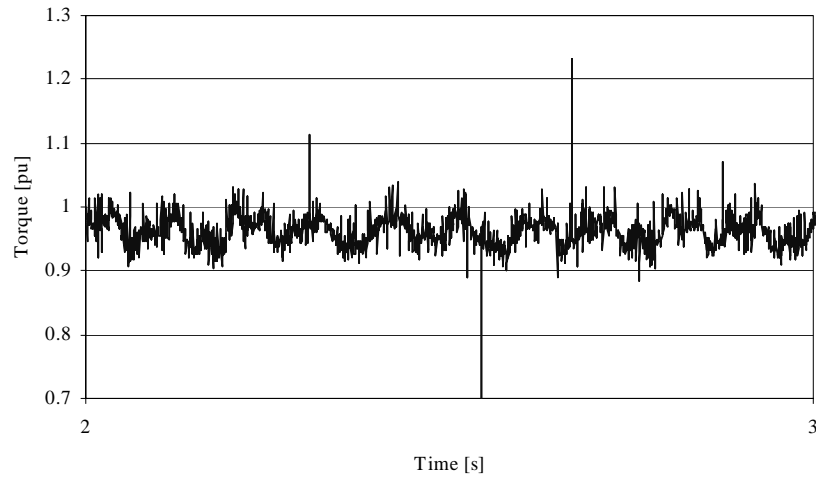
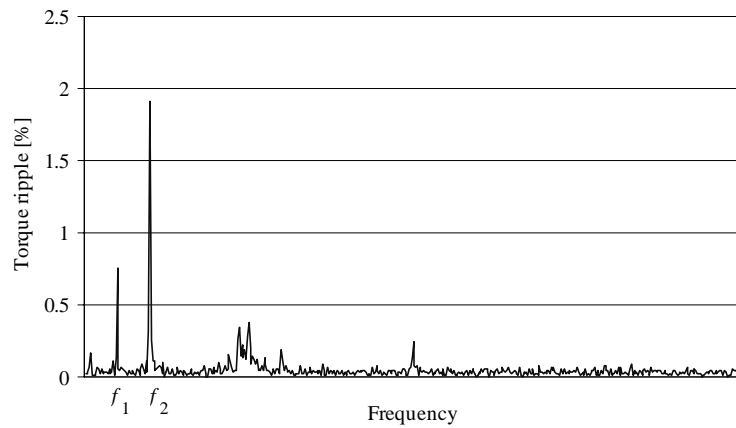Figure 5.5 Measured torque. Gain error is 2 % in current measurement of phase a.

Figure 5.6 Torque ripple due to 2 % gain error in current measurement of phase a. The highest torque ripple component appears at f_2, twice the fundamental frequency f_1.
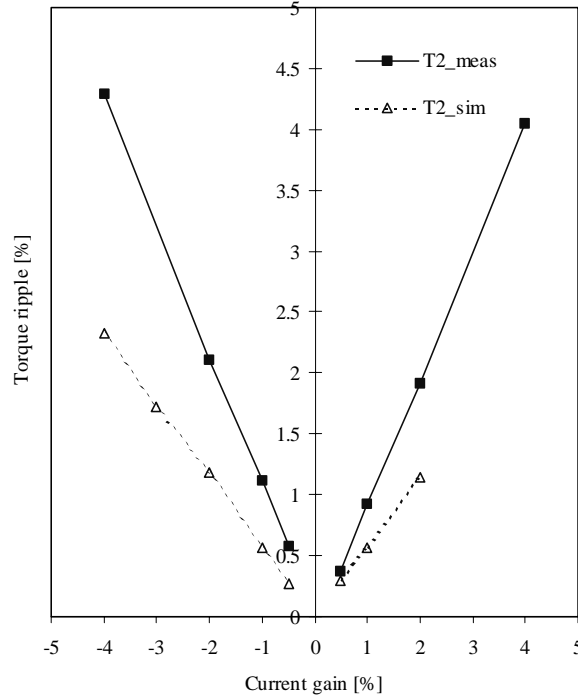
Figure 5.7   Torque ripple due to gain error in current measurement of phase a. The values of measured and simulated 2nd harmonic components of the torque are given.

5.2   Experimental setup 2

The second experimental equipment consisted of a Danfoss VLT 5027 frequency converter with the author self made control algorithm, a permanent magnet synchronous motor and a DC motor as the load. The software to hardware development environment is illustrated in Fig. 5.8. The setup 2 is further divided into two categories: a) PMSM not connected to the load, Fig. 5.9 and b) PMSM connected to the load, Fig. 5.10.

The standard control card of the VLT 5027 was replaced by another card that provides external control over the IGBT's gate drivers. The replacement card included protections against short-circuit overcurrent, DC overvoltage, shoot-through and overtemperature. The external control is provided by a dSPACE DS1103 PPC mixed RISC/DSP digital controller. The control algorithm is mainly based on the same Simulink model that was used in the simulation results part of this work. Matlab/Simulink is used as the base environment for designing the control algorithm. The Real Time Interface (RTI) connects the Simulink model to the physical world. The Real Time

Workshop (RTW) converts the Simulink model to C language, which is then compiled to the assembly language of the target processors. This development environment was found to be convenient and flexible for the purposes of this research.
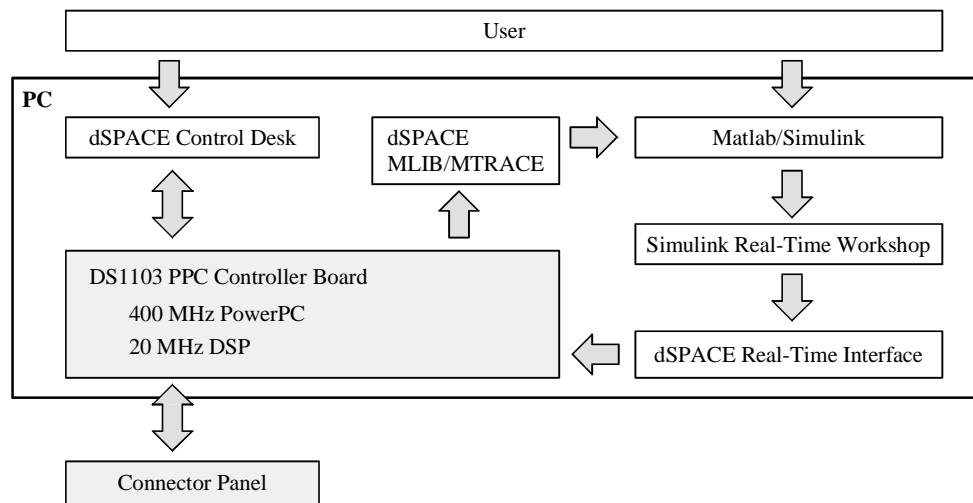

Figure 5.8 Software to hardware development environment of the experimental setup 2.
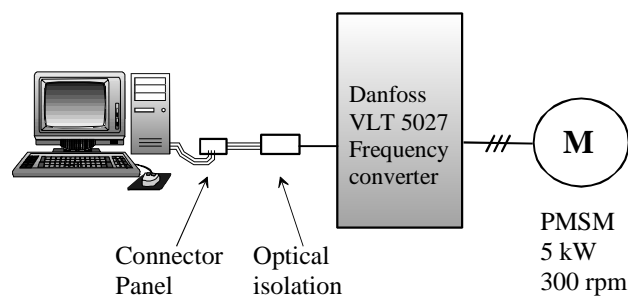

Figure 5.9 Experimental setup 2a: PMSM not connected to the load. DC-voltage and inverter output currents are measured. The speed signal used for control is either measured or estimated.
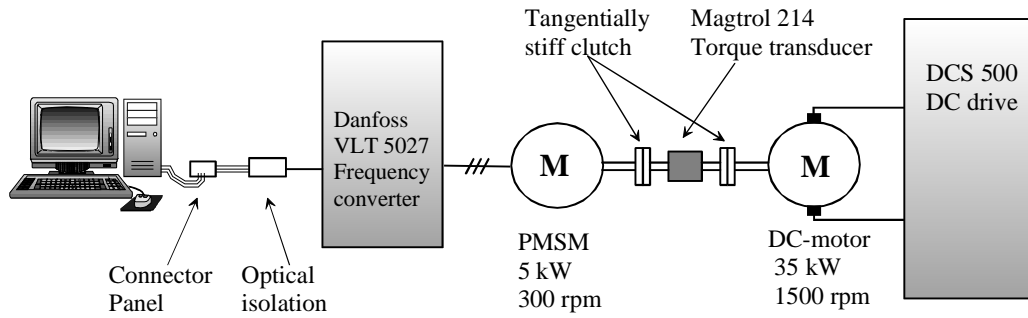
Figure 5.10 Experimental setup 2b: PMSM connected to the load (DC motor). DC-voltage, inverter output currents and torque are measured. The speed signal used for the control is either measured or estimated.

The offset and gain parameters of current measurement have been varied in order to obtain their effect on the torque ripple. The current transducer used was a closed loop current transducer (LA 55-P) using the Hall effect (LEM 1998). The overall accuracy of the transducer was reported by the manufacturer as ±0.65 % at the primary nominal current (50 A). The reported offset current was ±0.4 % of the nominal secondary current of the transducer, which is equivalent to ±2.5 % of the rated motor current of the experimental setup 2.

5.2.1   Offset error

The effect of the offset error on the speed ripple was measured with different offset values of the current measurement system in one phase. The motor was running without load (setup 2a). Figures 5.11-5.15 show the frequency spectrum of speed as a function of the offset error. The speed was measured with an incremental encoder. The reference stator frequency was varied between 5…25 Hz and the offset error in one phase was varied between –2…2 % of the rated motor current.
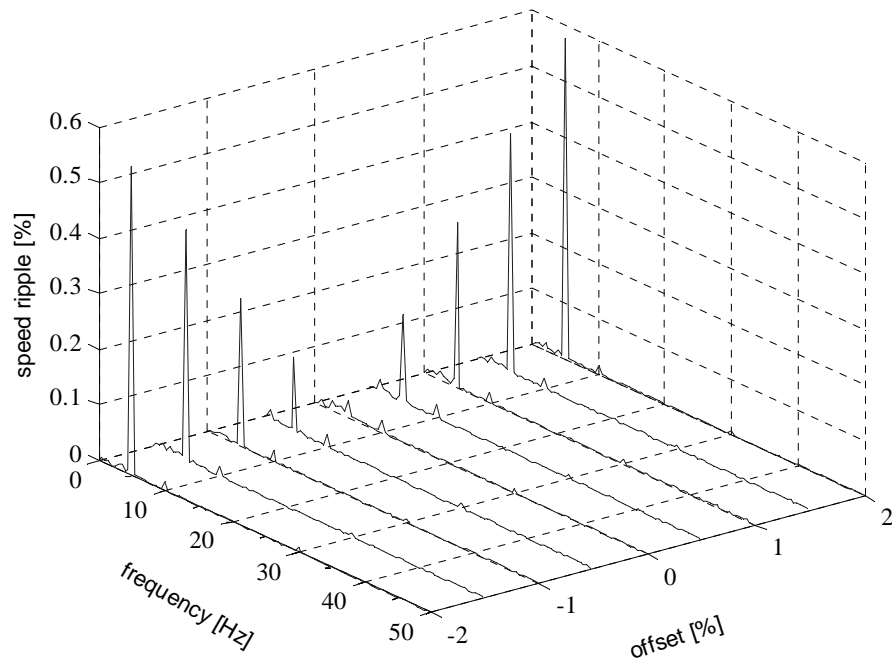
Figure 5.11 The frequency spectra of measured speed: offset error as parameter. The reference stator frequency is 5 Hz. No load is connected to the motor (setup 2a).

Figure 5.12 The frequency spectra of measured speed: offset error as parameter. Reference stator frequency is 10 Hz. No load is connected to the motor (setup 2a).
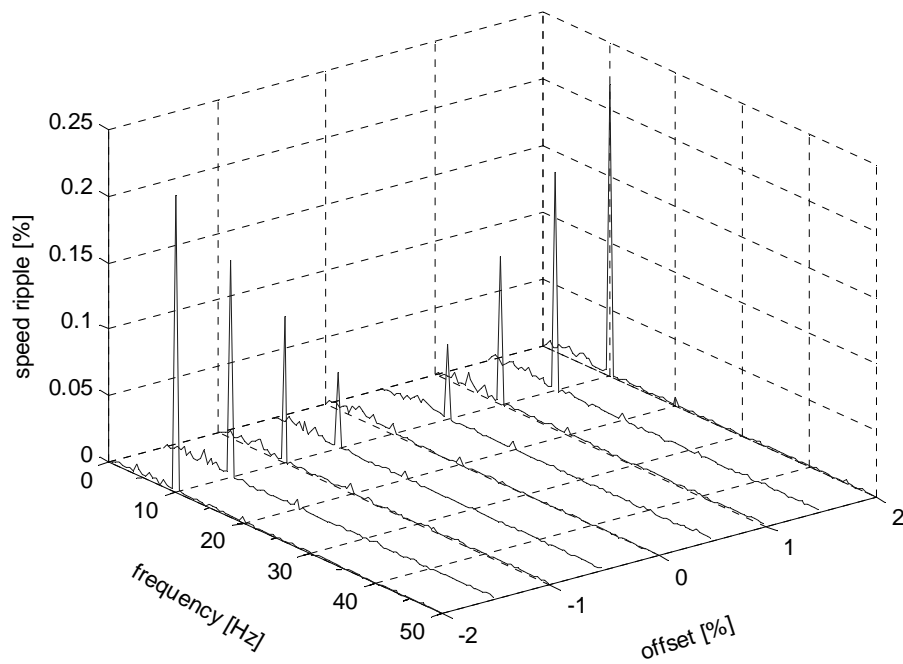
Figure 5.13 The frequency spectra of measured speed: offset error as parameter. Reference stator frequency is 15 Hz. No load is connected to the motor (setup 2a).

Figure 5.14 The frequency spectra of measured speed: offset error as parameter. Reference stator frequency is 20 Hz. No load is connected to the motor (setup 2a).
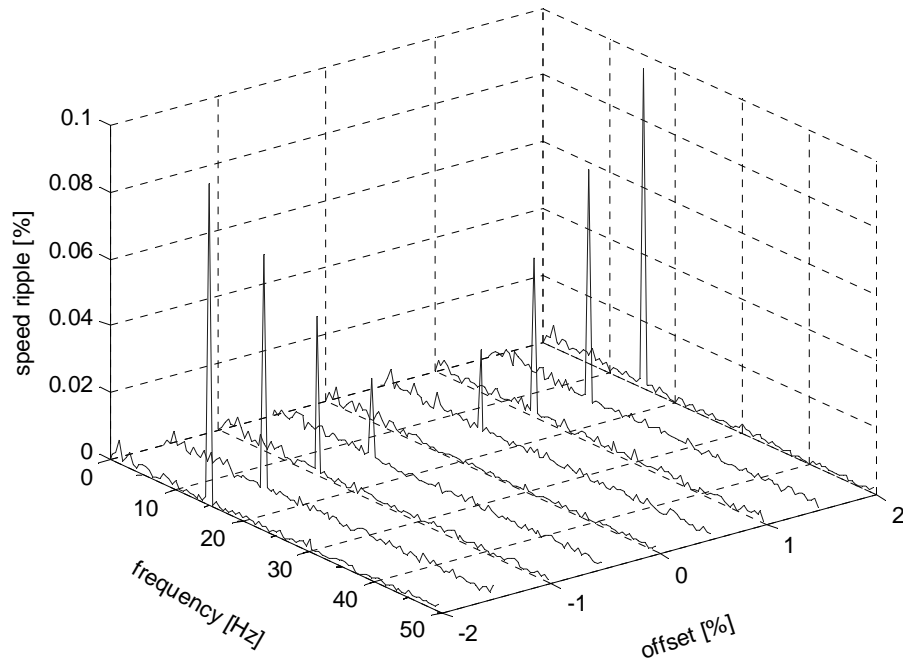
Figure 5.15 The frequency spectra of measured speed: offset error as parameter. Reference stator frequency is 25 Hz. No load is connected to the motor (setup 2a).
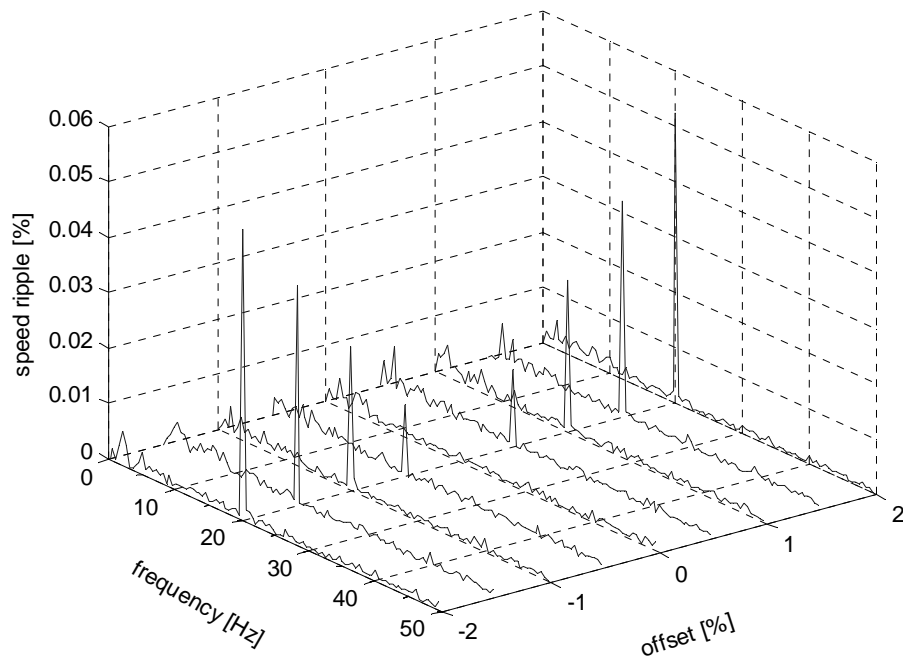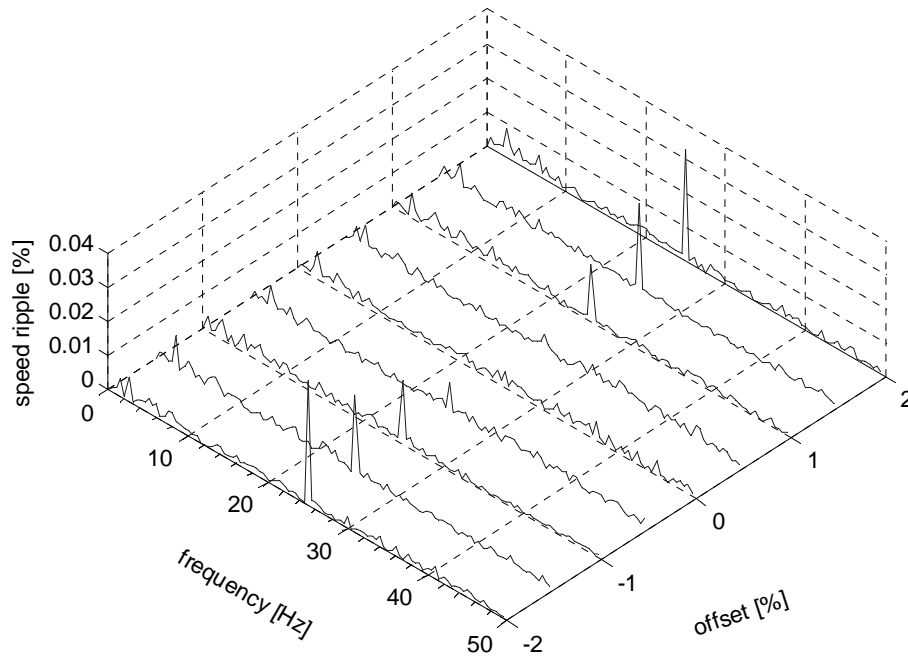
Figures 5.11-5.15 show that the offset error produces speed ripple at the fundamental stator frequency. The amplitude of the ripple decreases with increasing motor speed. This phenomenon is summarized in Fig. 5.16, where the speed ripple values are given as the amplitudes of the 1st harmonic component of speed as a function of stator frequency. Offset error values of 0…2 % have been used in the current measurement of one phase. Speed ripple as a function of offset error at different speeds (stator frequency) is shown in Fig. 5.17.
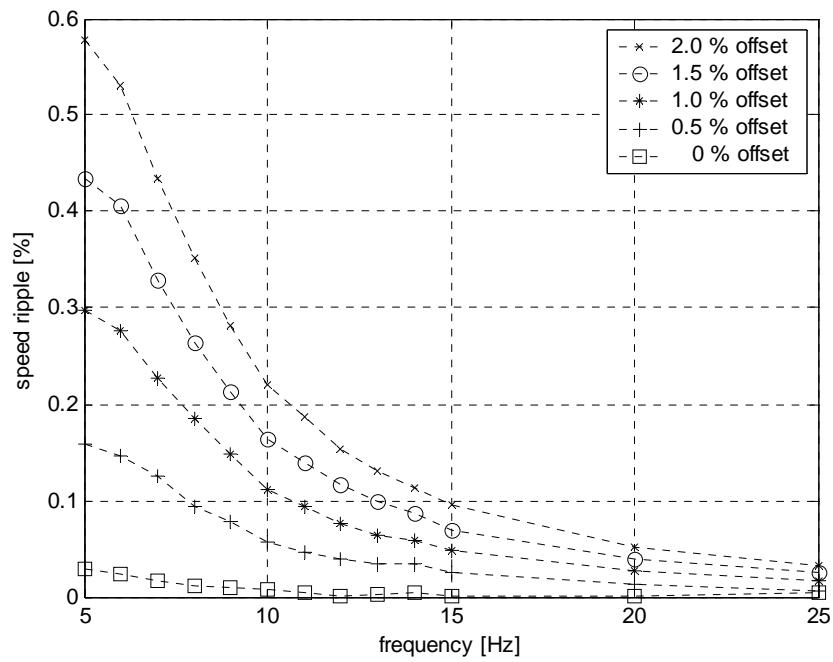
Figure 5.16 Speed ripple (the peak values of the 1st harmonic component of speed) as a function of stator frequency. The offset error as a parameter is varied between 0 % to 2 % of the motor rated current. No load is connected to the motor (setup 2a).
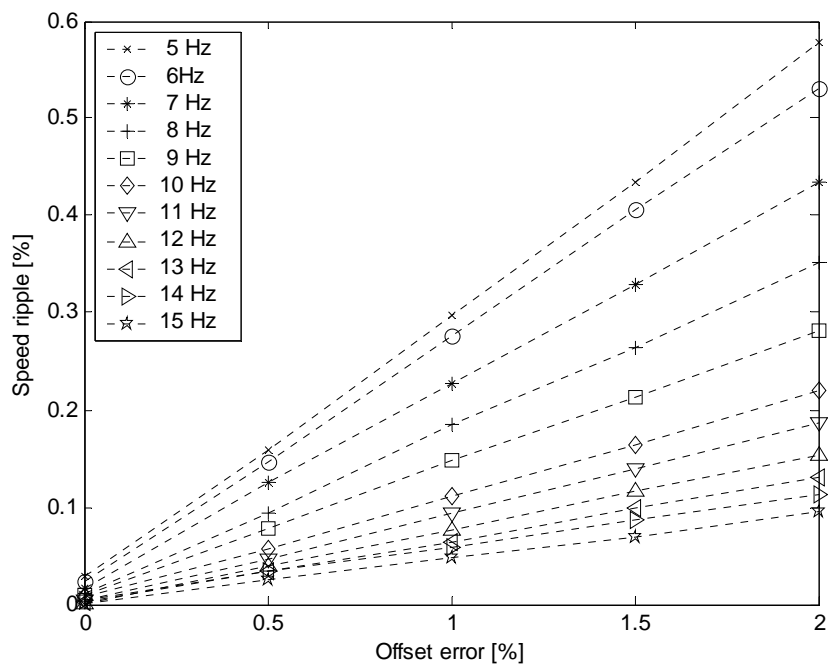

Figure 5.17 Speed ripple as a function of offset error at different speeds. No load is connected to the motor (setup 2a).

Fig. 5.17 shows that the speed ripple increases linearly as a function of offset error at different speeds. It is observed that, even if there is not a consciously induced offset error present (at 0 % offset error), the speed ripple is not zero at the fundamental frequency of the stator current. The offset error may not have been exactly zero after the starting of the motor or this ripple is due to other factors, e.g. motor construction and transducer misalignment.

Experimental setup 2b consists of the PMSM loaded with a DC motor and a torque meter between them. Speed and torque ripple as a function of offset error at different speeds (stator frequency) at 20 % and 80 % load situations are illustrated in Figures 5.18, 5.19 and 5.20, 5.21, respectively.

Figure 5.18 Speed ripple (the peak values of the 1st harmonic component of speed) as a function of stator frequency. The offset error is varied between 0 % to 2 % of the motor rated current. Load torque is 20 % of the rated value. (Setup 2b).
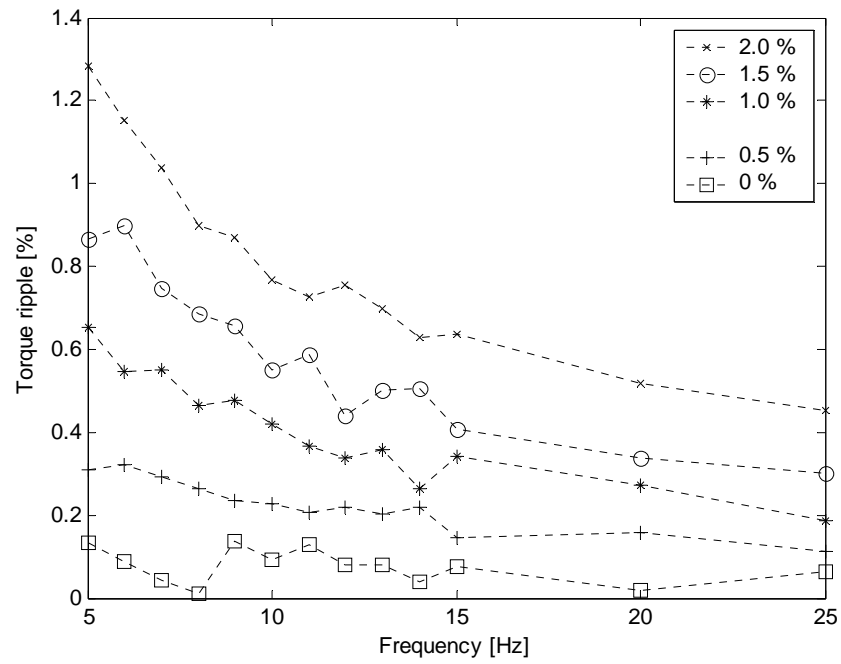
Figure 5.19 Torque ripple (the peak values of the 1st harmonic component of speed) as a function of stator frequency. The offset error is varied between 0 % to 2 % of the motor rated current. Load torque is 20 % of the rated value. (Setup 2b).
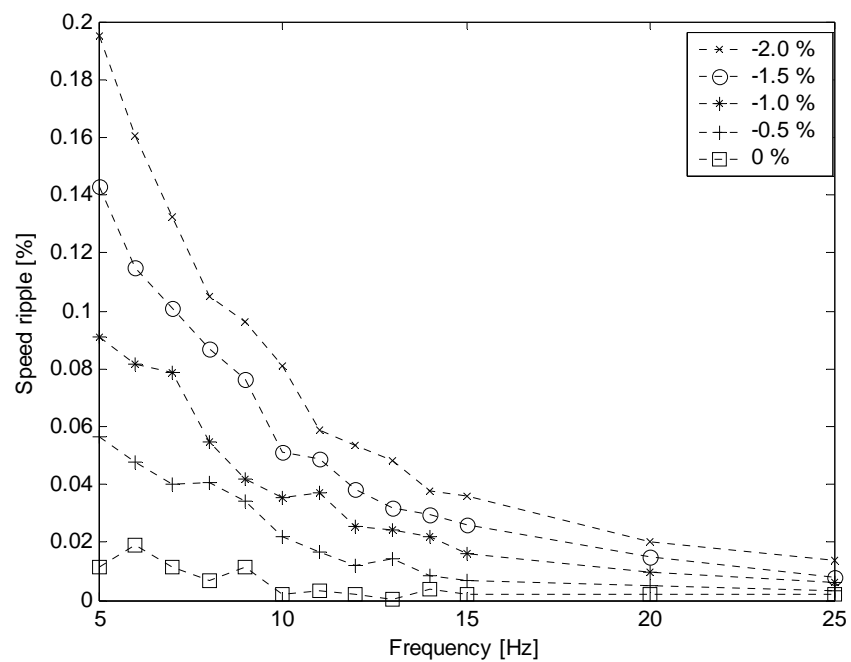
Figure 5.20 Speed ripple (the peak values of the 1st harmonic component of speed) as a function of stator frequency. The offset error is varied between 0 % to 2 % of the motor rated current. Load torque is 80 % of the rated value. (Setup 2b).
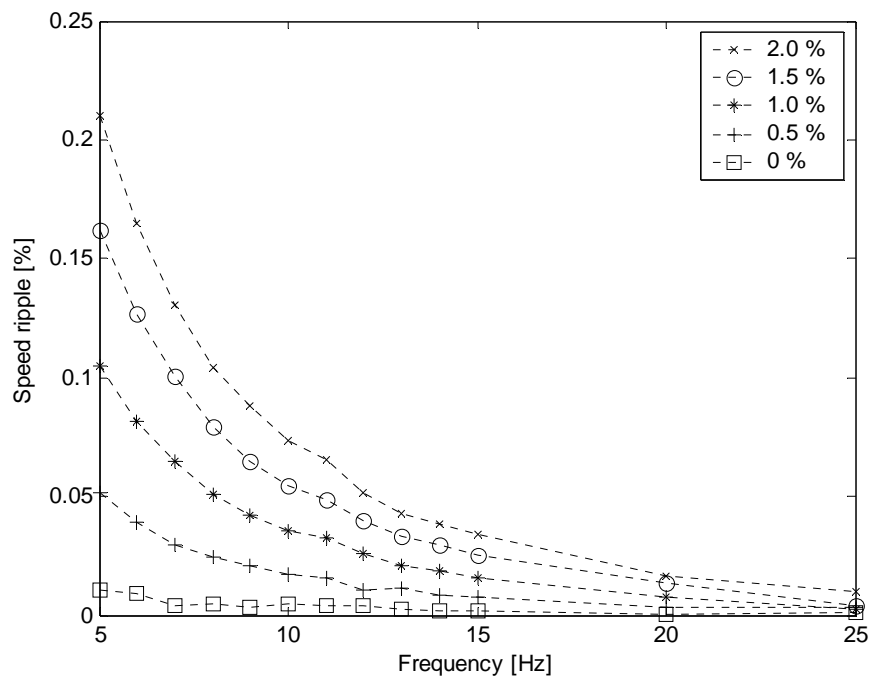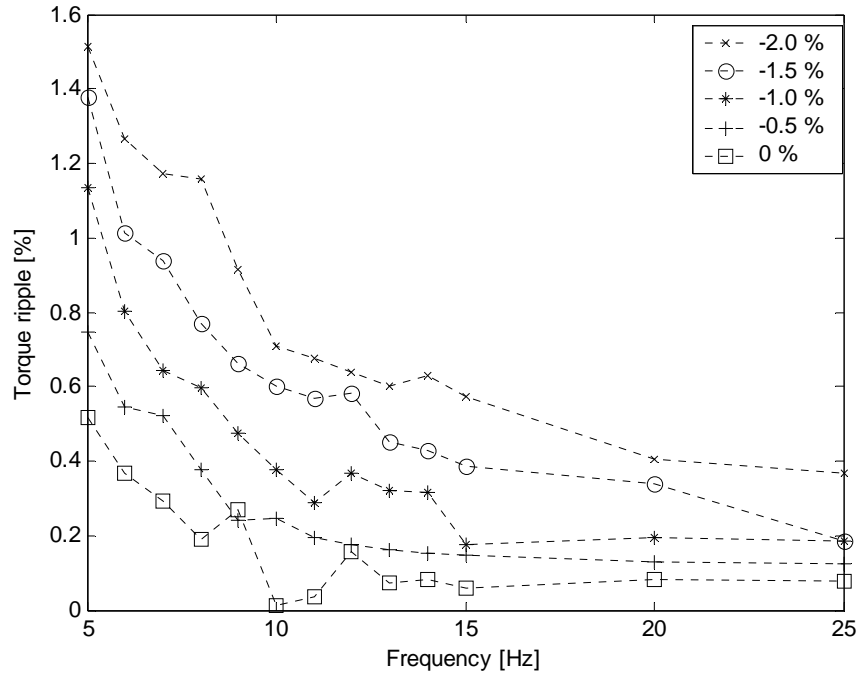
Figure 5.21 Torque ripple (the peak values of the 1st harmonic component of speed) as a function of stator frequency. The offset error is varied between 0 % to 2 % of the motor rated current. Load torque is 80 % of the rated value. (Setup 2b).

Figures 5.22 and 5.23 give the speed and torque ripples (1st harmonic amplitude) as a function of load torque, respectively. The current offset error is varied between –2.0 % to 2.0 %.

Figure 5.22 Speed ripple (1st harmonic amplitude) as a function of load torque at 6.28 rad/s. The offset error is varied between –2 % to 2 % of the motor rated current.
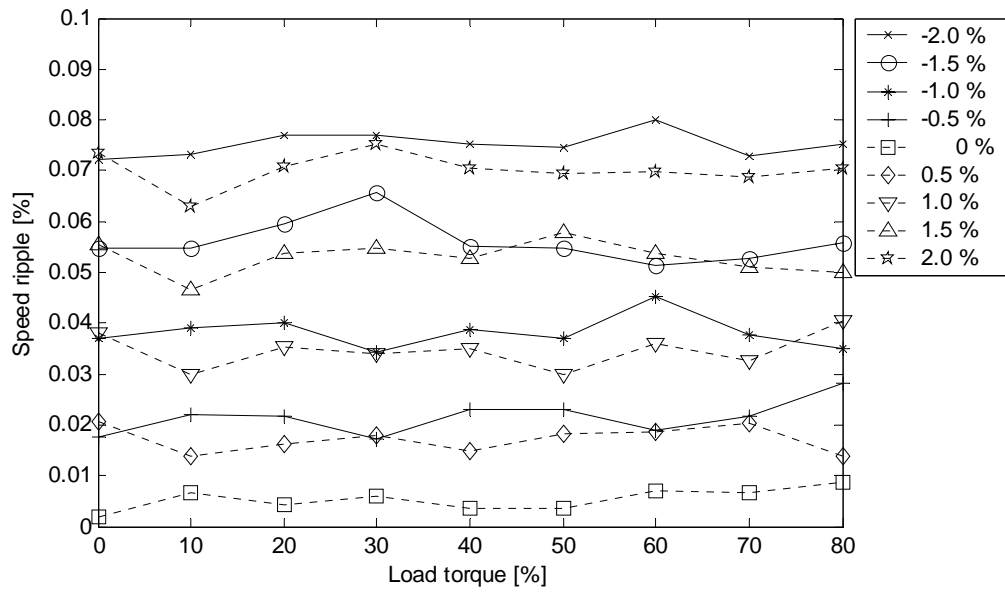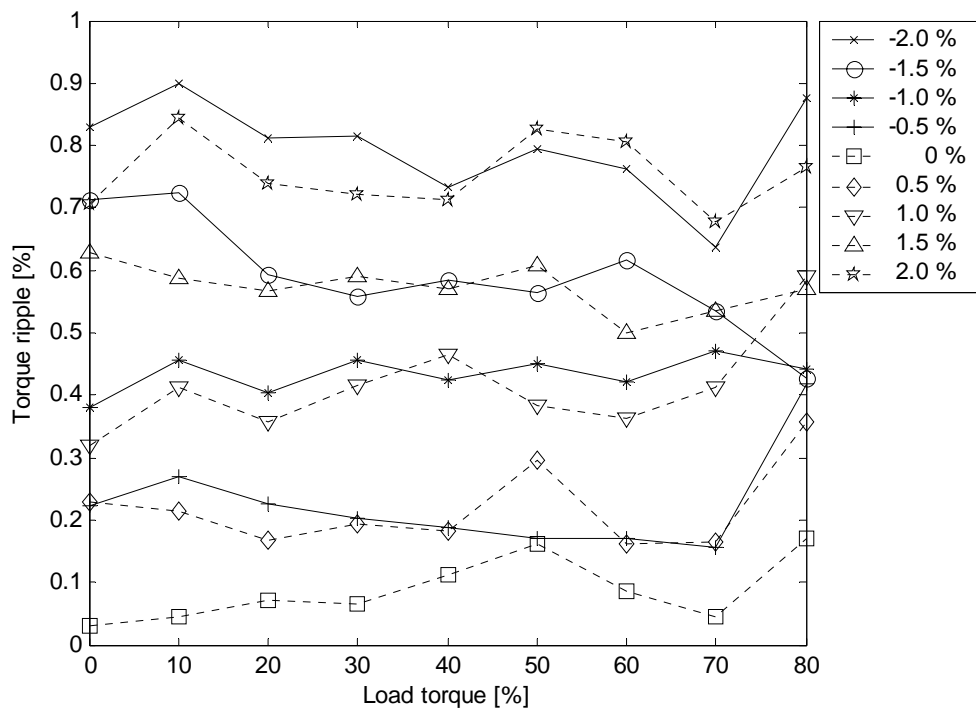

Figure 5.23 Torque ripple (1st harmonic amplitude) as a function of load torque at 6.28 rad/s.

Figures 5.22 and 5.23 indicate that the speed and torque ripple at the 1st harmonic, caused by an offset error in the current measurement, are independent of the load torque. The offset error level stays constant and is concluded to be independent of the load torque.

5.2.2   Compensation of the offset error

The current measurement error compensation algorithm presented in Fig. 4.2 was applied to reduce the speed and torque ripple in the experimental setup 2. Fig. 5.24 shows the measured speed and speed ripple before and after compensation. The speed ripple was due to a 2 % offset error in the current measurement of one phase. No load was connected to the motor (setup2a).
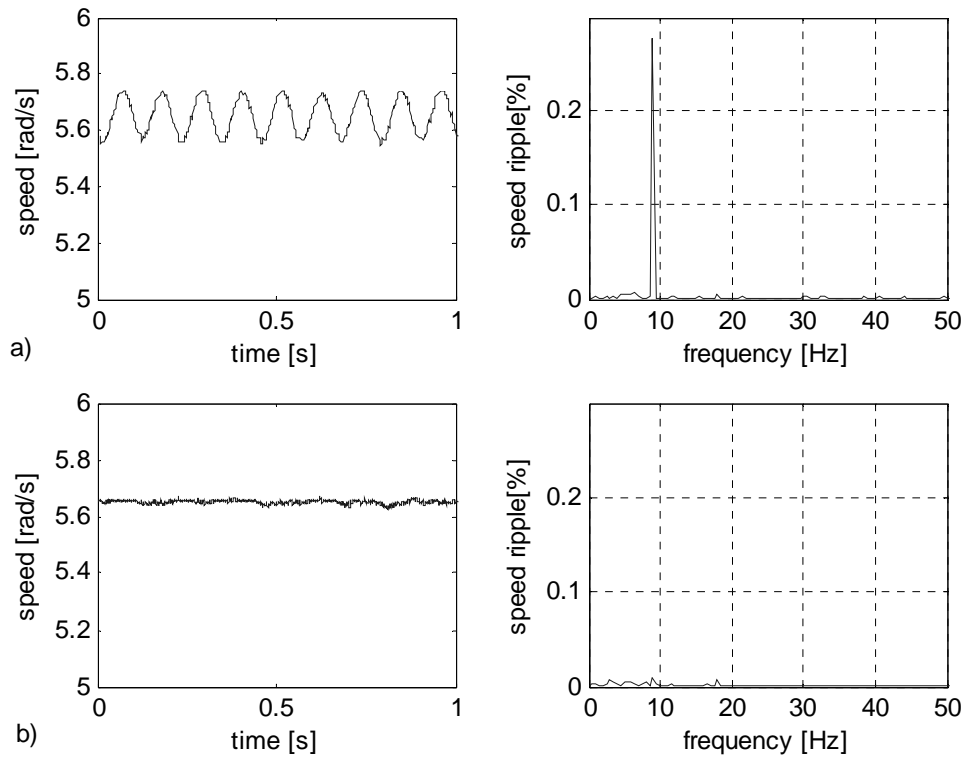
Figure 5.24 Measured speed and speed ripple due to 2 % offset error in current measurement of one phase: a) before compensation, b) after compensation. Stator reference frequency is 9 Hz. No load is connected.

The compensation method reduces the speed ripple at the fundamental frequency from 0.28 % of the motor rated speed to 0.008 %. Running through the compensation algorithm and finding a compensation alternative for 1.5 % offset error in phase a is shown in Fig. 5.25 for the setup 2b.

Figure 5.25 Running through the compensation algorithm and finding a compensation alternative for +1.5 % offset error in phase a. After five alternatives a suitable compensation is found. The stator reference frequency is 10 Hz.

In Fig. 5.25, the compensation algorithm runs through the compensation alternatives. Phase a has a positive offset error and has to be compensated to the negative direction. During the compensation routine some incorrect alternatives are tested and the speed ripple increases temporarily during them. After five alternatives a suitable compensation is found. The compensation method reduces the speed ripple at the fundamental frequency from 0.05 % of the motor rated speed to less than 0.01 %, which was defined as the required level.

The compensation procedure of two offset errors is shown in Fig. 5.26. Both phases have a positive offset error and have to be corrected to the negative direction. This time after two alternatives a suitable compensation is found. The speed ripple at the fundamental frequency is reduced from 0.065 % of the motor rated speed to less than 0.01 %, which was again defined as the required level.
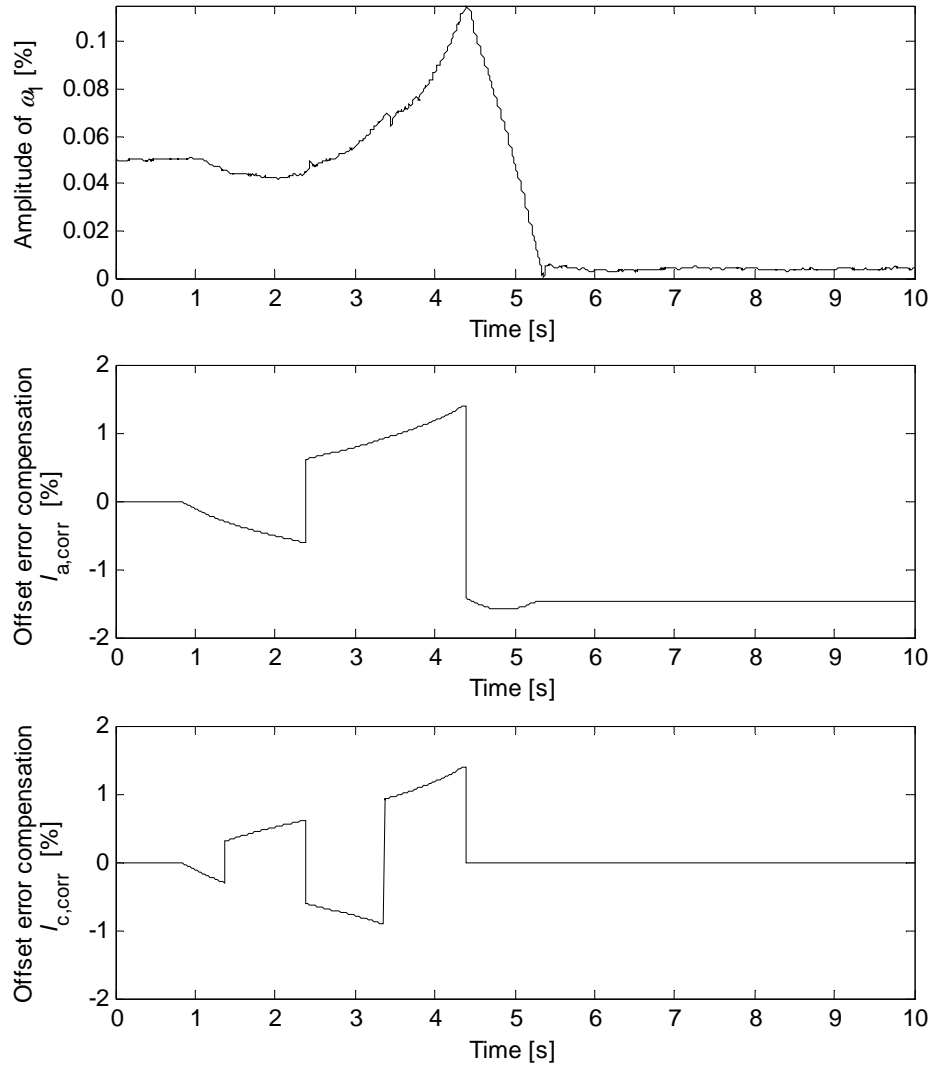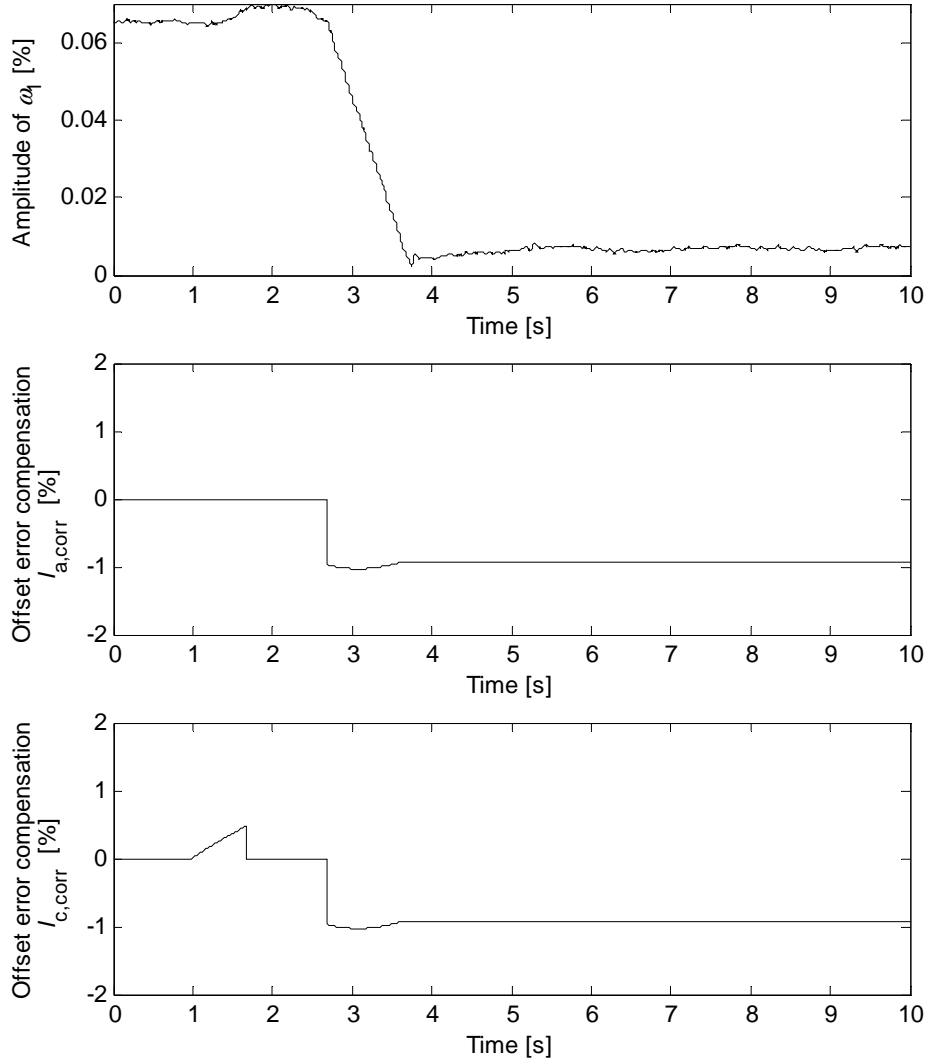

Figure 5.26 Running through the compensation algorithm and finding a compensation alternative for +1.0 % offset error in phase a and +1.0 % offset error in phase c. After two alternatives a suitable compensation is found.

5.2.3 Gain error

Speed and torque ripples (the 2nd harmonic amplitude) due to gain error as a function of stator frequency are shown in Fig. 5.27 and 5.28. Figures 5.29 and 5.30 show the speed and torque ripples (2nd harmonic amplitude) as a function of load torque. The gain error in current measurement of one phase is varied between –5 % to 0 % or 0 % to 5.0 % of the measured current.
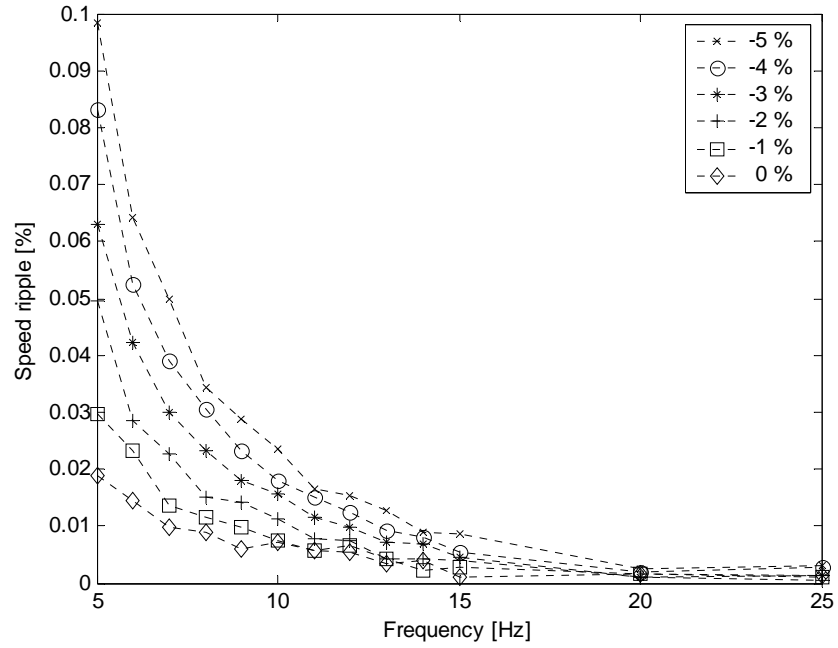
Figure 5.27 Speed ripple (the 2nd harmonic amplitude) due to gain error as a function of stator frequency. The gain error is varied between –5 % to 0 % of the measured current. The load torque is 80 % of the rated torque.
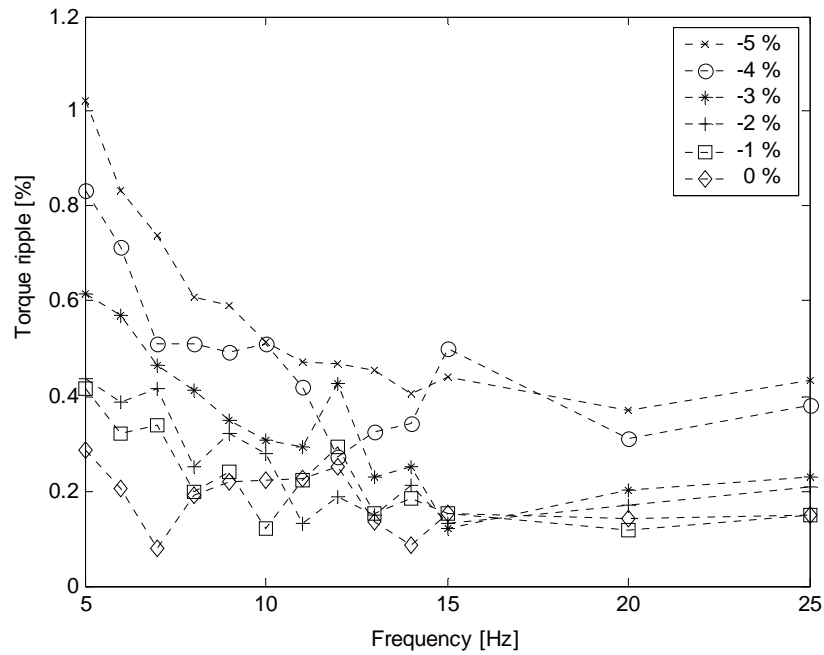
Figure 5.28 Torque ripple (the 2nd harmonic amplitude) due to gain error as a function of stator frequency. The gain error is varied between –5 % to 0 % of the measured current. The load torque is 80 % of the rated torque.
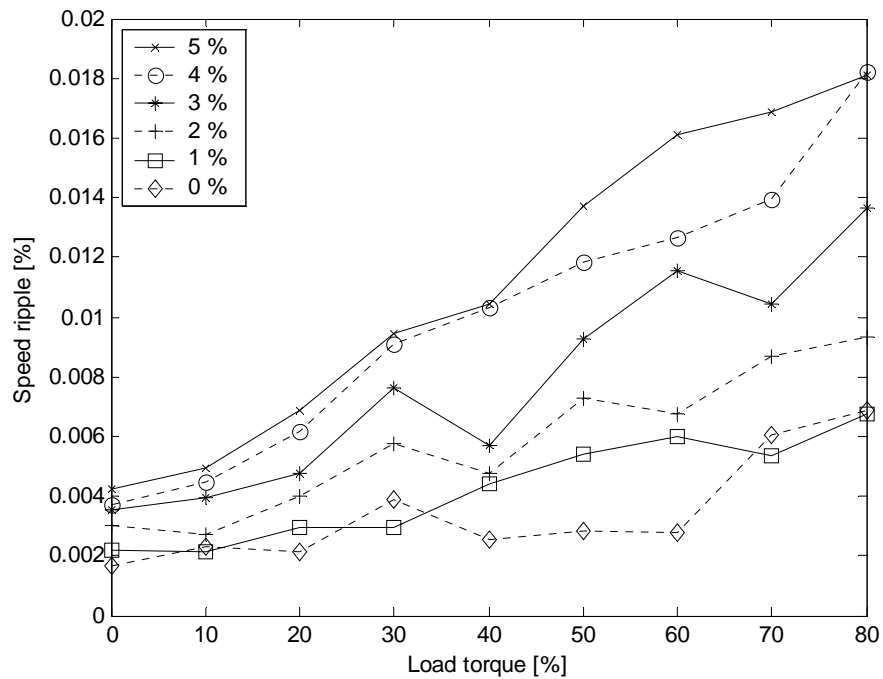
Figure 5.29 Speed ripple (2nd harmonic amplitude) due to gain error as a function of load torque at 6.28 rad/s. The gain error is varied between 0 % to 5 % of the measured current.
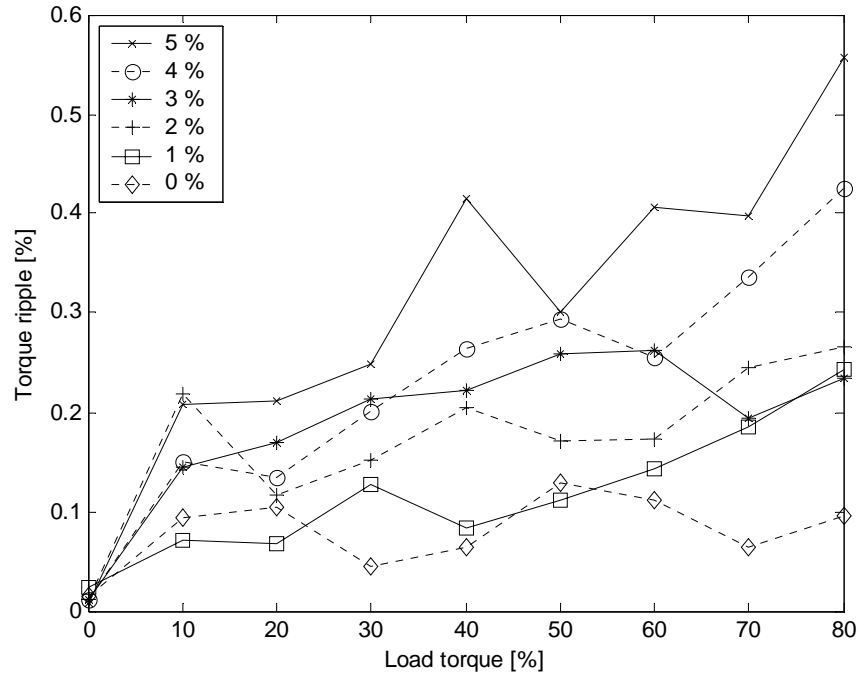
Figure 5.30 Torque ripple (2nd harmonic amplitude) due to gain error as a function of load torque at 6.28 rad/s. The gain error is varied between 0 % to 5 % of the measured current.

Figures 5.29 and 5.30 indicate that the speed and torque ripple at the 2nd harmonic, caused by the gain error in current measurement, increase as the function of the load torque. This is due to the fact that the gain error is related to the measured stator current, which increases as the load torque increases. The amplitude of the 2nd harmonic component caused by the gain error is generally lower than the amplitude of the 1st harmonic component caused by the offset error.

5.2.4   Compensation of the gain error

The compensation method defined in chapter 4.1.1 was used in the experimental setup 2 also for the compensation of the gain error in current measurement. Fig. 5.31 presents the amplitude of the 2nd harmonic component of speed ripple before, during and after the compensation routine.
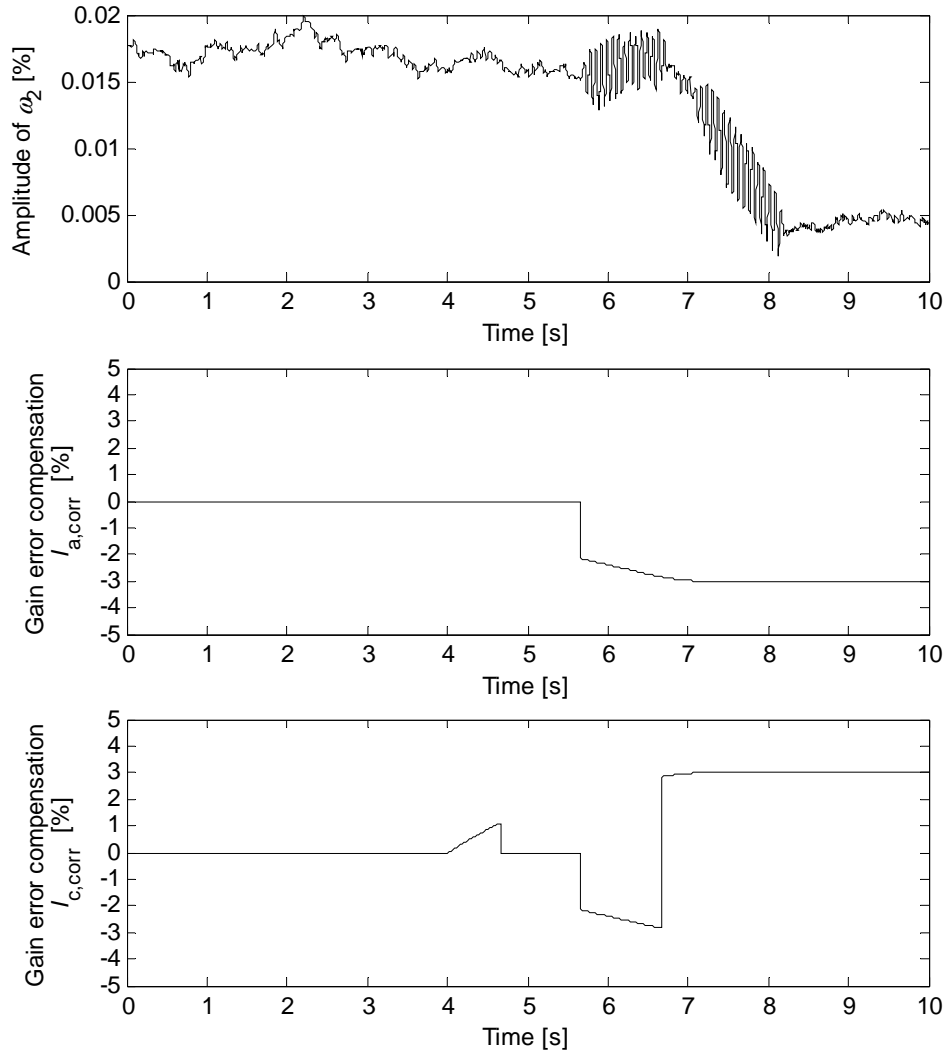
Figure 5.31 Amplitude of the 2nd harmonic component of the speed ripple, and the operation of the compensation routine. Gain error of +3 % is present at the a-phase and –3% at the c-phase. Load torque is 20 % of the rated torque at stator reference frequency 7 Hz.

The speed ripple caused by a 3 % gain error in a- and c-phases is reduced from 0.017% to 0.005%, which was the required level in this case, where the load torque was 20 %.

5.2.5   Features of the compensation method

The introduced current measurement error compensation method reduces the speed and the torque ripples, caused by the offset and gain errors, to an acceptable level. The method is based on analysing the amplitude of one selected harmonic component of the input signal, which in

this case is either speed or torque, at constant speed. This analysis requires knowledge of the error sources that produce the speed and torque ripples and the harmonics at which the ripples appear.

The compensation method is in principle quite simple, but requires computation capacity for the real-time calculation of the discrete Fourier transform (DFT). With the experimental setup this means that only one input signal and one corresponding harmonic can be analysed at the same time. However, this is already limited by the fact, that the operational principle of the compensation method is based on changes in one ripple producing parameter at a time. Adjusting two or more ripple producing parameters at the same time might interfere each other, if they would produce harmonics at same frequencies.

Finding the right compensation is implemented by running through a series of compensation alternatives. In the case of an offset error in the current measurement the number of compensation alternatives is eight, if two stator currents are measured and the alternative $I_{a,corr} = I_{c,corr} = 0$ is left out. The drawback of running straight through the compensation alternatives in numerical order is that before the appropriate alternative is selected, some incorrect alternatives may have been tested. During the short period of the application of an incorrect alternative, more speed or torque ripple might appear, the significance of which remains application specific. One benefit of the compensation method is, that even if the absolutely correct compensation alternative is not found, the speed or torque ripple can be reduced under the required level.

The quality of the compensation method is also dependent of the correlation between the speed ripple and current measurement error. As seen in Fig. 5.16 and 5.18 the speed ripple (amplitude of the 1st harmonic) produced by the offset error in current measurement is dependent of the speed and the load inertia. With the experimental setup 2 only one correlation line between the speed ripple and the current measurement error was used at a time. Further development would be a correlation table, e.g. more correlation lines at different speeds as in Fig. 5.17.

In the experiments with the 5 kW PMSM the compensation method was found to operate reliably in the low speed range down to 5 Hz supply frequency. The operation of the compensation method was not tested at lower supply frequencies than 5 Hz. At lower speeds than this the analyzed time period should be lengthened, which would lead to slower respond of the compensa-

tion. In the higher speed range the amplitude of the speed ripple decreases to virtually insignificant, as the experimental results verify.

The functioning of the compensation method in resonance was not tested. Considering a risk situation, running the compensation method in resonance might temporarily increase the speed ripple amplitude and thus lead to damage. From this point of view the compensation method should not be run on the resonance frequency of the system. On the other hand, the compensation method is intended to run at constant speed operation, and the operation at the resonance frequency is generally to be avoided in electric drives as any other excitation might increase the speed ripple amplitude.

The compensation method introduced needs to be implemented only in the software and needs no hardware modifications. The compensation algorithm does not need to be calculated all the time, but only during the compensation routine. The compensation routine is started when the speed ripple exceeds the required level and is stopped when a suitable compensation alternative is found and the speed ripple has gone under the required level.

5.3   Summary

The experiments given in chapter 5 show the effect of current measurement errors on speed and torque ripple with two experimental setups. The first setup consisted of a laboratory version of an ACS-600 frequency converter with standard software, an axial flux permanent magnet synchronous motor and a DC motor as the load. The effects of offset and gain errors on torque ripple are shown with the comparison of experimental and simulation results. The comparison of the measured and simulated results show that the torque ripple appears at the same frequency, but the amplitude differs as the error increases. This is apparently due to the fact that in the simulations only the current measurement error is taken into account, but in the experimental setup the characteristic properties of the setup, e.g. mechanical resonance frequencies enable to amplify the torque ripple amplitude.

The second experimental setup was applied to test the self-made control algorithm and the proposed compensation method. The setup consisted of a VLT 5027 frequency converter with self-made control algorithm, a permanent magnet synchronous motor and a DC motor as the

load. The control algorithm was based on the simulation model used earlier in this work. At the experiments the speed and torque ripples due to the offset and gain errors were found to increase non-linearly when the speed decreased. The increase of offset error increased the speed ripple linearly. With the offset error the load torque had no clear effect on the speed and torque ripple amplitudes. In the case of the gain error the speed and torque ripples increased with the load torque.

The experimental results show that the proposed current measurement error compensation method has a good performance in the speed and torque ripple reduction of a permanent magnet synchronous motor drive. The compensation method reduces the speed and the torque ripples, caused by the offset and gain errors, under the required level. At no load connected to the PMSM, the speed ripple due to 2 % offset error was reduced from 0.28 % of the motor rated speed to 0.008 %, when the speed signal was measured and the stator reference frequency was 9 Hz. With estimated speed signal, at 10 Hz reference frequency, 0.05 % speed ripple due to 1.5 % offset error was reduced to 0.01 %. Compensation of a ±3 % gain error reduced the speed ripple from 0.017 % to 0.005 % at 7 Hz stator reference frequency and 20 % load torque.

CONCLUSIONS

Frequency converter non-idealities that produce speed and torque ripple in electric drives were analysed on a direct torque controlled permanent magnet synchronous machine drive. Especially, the origin of low order harmonics in speed and torque was examined and possible reasons were detected. It was shown theoretically how different current measurement error types affect the torque.

In addition to the offset and gain errors in current measurement, the non-linearity of Hall-effect current sensors produces torque ripple in DTC PMSM drives. The shape of the non-linearity has an effect on the harmonics of the torque. Hysteresis error in the current sensor produces torque harmonics at integer multiples of the fundamental frequency, the first and the third harmonic being the most significant ones.

A simulation model to analyse the effect of converter non-idealities on the electric drives' performance was created. The model enables to identify potential problems causing torque vibrations and possibly damaging oscillations in electrically driven machine systems. The model can be utilized in the design and troubleshooting of electrically driven machine systems. The model is capable of coupling with simulation software of complex mechanical loads. Furthermore, the simulation model of the converter can be applied to control a real frequency converter.

A method to reduce the speed and torque ripple by compensating the current measurement offset and gain errors was introduced. This current measurement error compensation method reduces the speed and torque ripple, caused by the offset and gain errors, to a required level. The method is based on analysing the amplitude of one selected harmonic component of the input signal, which in this case is either speed or torque. The analysis is executed in real time. Simultaneously, a suitable compensation is chosen from a series of compensation alternatives, where the compensation level and direction is to be determined. The speed can be either measured or estimated, so the compensation method is applicable also for speed sensorless drives.

The proposed compensation method was tested in both simulation and experimental environments. The method was found to reduce speed and torque ripple to an acceptable level. The speed ripple compensation method suggested is suitable not only for the direct torque control

method and PMSM used herein, but also for other control methods and motor types. Moreover, this method can be implemented by modifying only the software.

Future work on the topic of this research could include further development of the coupled simulation models of the electric drive and the mechanical load in ADAMS to reduce the calculation time for complex mechanical loads. This would need modification of the coupled simulation model to have different time steps for the mechanical load and the electric drive. Lengthening the time step for the mechanical load would result in time-saving simulations.

More functions could be added to the current measurement compensation method. As the quality of the compensation method for the current measurement errors is dependent of the correlation between the speed ripple and the current measurement error, further development would be a correlation table, e.g. more correlation lines at different speeds. In the identification run, the load inertia could be determined first and after that the correlation between the load inertia, current measurement error and speed ripple amplitude could be determined in that particular application. Furthermore, adding more logic to the selection of the compensation alternative could hasten the finding of the most adequate ripple limiting compensation alternative.

REFERENCES

Andreescu 2002   Andreescu, G.D., Popa, A., Flux Estimator Based on Integrator with DC-Offset Correction Loop for Sensorless Direct Torque and Flux Control, ICEM 2002, 15th International Conference on Electrical Machines, Conference Record, Aug. 2002, 6 p.

Antić 1994   Antić, D., Klaassens, J.B., Deleroi, W., Side effects in Low-Speed AC Drives, Power Electronics Specialists Conference, PESC '94 Record., 25th Annual IEEE, 1994, pp. 998–1002.

Bar-Lev 1993   Bar-Lev, A., Semiconductor and Electronic Devices, 3rd edition, Prentice Hall, 1993, 469 p., pp. 24, 456.

Barro 1997   Barro, R., Ping, H., Torque ripple compensation of induction motors under field oriented control, Applied Power Electronics Conference and Exposition, 1997. APEC '97 Conference Proceedings, Twelth Annual, Vol. 1, 23-27 Feb. 1997, pp. 527–533.

Beccue 2003   Beccue, P., Pekarek, S., Neely, J., Stutts, D., Design of a closed-loop controller for mitigation of torque ripple in a brushless DC machine, Power Electronics Specialist, 2003, PESC '03, IEEE 34th Annual Conference on, Volume: 4 , 15-19 June 2003, pp. 1664–1670.

Bird 1997   Bird, I.G., Zelaya De La Parra, H., Fuzzy logic torque ripple reduction for DTC based AC drives, Electronics Letters, Vol. 33, No. 17, 1997, pp. 1501–1502.

Borghi 1998   Borghi, C.A., Casadei, D., Fabbri, M. and Serra, G., Reduction of the Torque Ripple in Permanent Magnet Actuators by a Multi-Objective Minimization Technique, IEEE Transactions on Magnetics, Vol. 34, No. 5., September 1998, pp. 2869–2872.

Bose 1997   Bose, B.K., Power Electronics and Variable Frequency Drives, Technology and Applications, IEEE Press, 1997, 640 p., pp. 175–180.

Bürkel 1996   Bürkel, R., Friot, M., Graffert, H., Huber, H.-D. Koss, J., Nemitz, A. and Victor, A., Isolated Current and Voltage Transducers, Chararacteristics–Applications– Calculations. LEM Corporate Communications, LEM Geneva, Switzerland, 1996, 31 p.

Cai 2000   Cai, W., Fulton, D. and Reichert, K., Design of Permanent Magnet Motors with Low Torque Ripples: A Review, in Proc. ICEM 2000, 2000, pp. 1384–1388.

Căruntu 2002   Căruntu, G., Dragomirescu, O., Consideration regarding the offset of the magnetic sensors, Semiconductor Conference, CAS 2002 Proceedings. International, Vol. 1, 2002, pp. 87–90.

Casadei 1994	Casadei, D., Grandi, G., Serra, G., Tani, A., Effects of flux and torque hysteresis band amplitude in direct torque control of induction machines. 20th International Conference on Industrial Electronics, Control and Instrumentation, IECON '94, Vol. 1, 1994 , pp. 299–304.
Chen 2000	Chen, S., Namuduri, C., Mir, S., Controller Induced Parasitic Torque Ripples in a PM Synchronous Motor, Industry Applications Conference, Conference Record of the 2000 IEEE, Vol.1, 2000, pp. 171–178.
Cheok 2002	Cheok, A.D., Chong, T.S., Zhongfang, W., Real-time computer-based torque measurement of switched reluctance motors, International Journal of Electronics, Vol. 89, No. 9, 2002, pp. 693–715.
Chew 2003	Chew, M.-H., Measuring motor drive and inverter currents; easy and economical with isolation amplifier, PCIM Europe, July/August 2003, pp. 56–57.
Cho 1994	Cho, K.-Y., Bae, J.-D., Chung, S.-K., Youn, M.-J., Torque harmonics minimisation in permanent magnet synchronous motor with back EMF estimation, IEE Proc.-Electr. Power Appl., Vol. 141, No. 6, November 1994, pp. 323–330.
Choi 1998	Choi, J.-W., Lee, S.-S., Yu, S.-Y., Jang, S.-J., Novel Periodic Torque Ripple Compensation Scheme in Vector Controlled AC Motor Drives, Applied Power Electronics Conference and Exposition, APEC '98. Conference Proceedings 1998, Thirteenth Annual, Volume: 1, 15-19 Feb. 1998, pp. 81–85.
Choi 2000	Choi, Y.-W., Jung-Ik, H., Sul, S.-K., Chung, D.-W., Kang, J.-K., Lee, G.-H., Kim, H.-J., Lee, J.-P, Suppression of Vibration for Elevator System using Deadtime Compensation with Current Prediction, Advanced Motion Control 2000, Proceedings, 6th International Workshop on , 2000, pp. 439–442.
Choi 2002	Choi, C.-S., Cha, G.-H., Kang, H.-S., Song, C.-S., Design Parameter Optimization for Hall Sensor Application, Proc. 23rd international conference on microelectronics, MIEL 2002, Vol. 1, NIŠ, Yugoslavia, 12.-15. May, 2002, pp. 273–276.
Chung 1998	Chung, D.-W. and Sul, S.-K., Analysis and compensation of current measurement error in vector-controlled ac motor drives. IEEE Transactions on Industry Applications, Vol. 34, No. 2, March/April 1998, pp. 340–345.
Coombs 1995	Coombs, C.F. Jr., Electronic Instrument Handbook, Second edition, McGraw-Hill, 1995, pp. 13.28.

Costa 2001   Costa, F., Poulichet, P., Mazaleyrat, F., Labouré, E., The Current Sensors in Power Electronics, a Review, EPE Journal, Vol. 11, No. 1., February 2001, pp. 7–17.

Cristaldi 2001   Cristaldi, L., Ferrero, A., Lazzaroni, M., Ottoboni, R., A Linearization Method for Commercial Hall-Effect Current Transducers, IEEE Transactions on Instrumentation and Measurement, Vol. 50, No. 5, October 2001, pp. 1149–1153.

Doebelin 1990   Doebelin, E.O., Measurement systems – application and design, 4th edition, McGraw-Hill, 1990, pp. 70.

Emerald 1999   Emerald, P., Expanding the Operative Range of Open-Loop Hall Effect Current Sensing, Sensors, Vol. 16, No. 9, Sept. 1999.

Emerald 1998   Emerald, P., "Non-intrusive" Hall-effect current sensing techniques provide safe, reliable detection and protection for power electronics, Technical paper, Allegro Microsystems Inc., 1998.

Erkkilä 2002   Erkkilä, I., Conversation of the torque vibration problems in Finnish paper machine industry, SaMeKo-project, 2002.

Göpel 1989   Göpel, W., Hesse, J., Zemel, J.N., Sensors – A Comprehensive Survey, VCH, Weinheim, 1989, pp. 20–21.

Hall 1879   Hall, E.H., On a New Action of the Magnet on Electric Currents, American Journal of Mathematics, Vol. 2, 1879, pp. 287–292.

Harnefors 1998   Harnefors, L., Nee, H.-P., Control of Variable-Speed AC Drives, Electrical Machines and Drives, Department of Electric Power Engineering, Royal Institute of Technology, Stockholm, 1998, 124 p.

Hirvonen 2003   Hirvonen, M., Handroos, H., Sopanen, J., Laurila, L., Kurronen, P., Salminen, P., Pyrhönen, J., Analysis and control of vibrations in electrically driven machine systems, TUKEVA, Research Programme on Future Mechanical Engineering, Final Report, Nov. 2003, pp. 88–95.

Holtz 1996   Holtz, J., Springob, L., Identification and Compensation of Torque Ripple in High-Precision Permanent Magnet Motor Drives, IEEE Transactions on Industrial Electronics, Vol. 43, No. 2., April 1996, pp. 309–320.

Holtz 2002   Holtz, J., Quan, J., Sensorless Vector Control of Induction Motors at Very Low Speed Using a Nonlinear Inverter Model and Parameter Identification, IEEE Transactions on Industry Applications, Vol. 38, No. 4., July/August 2002, pp. 1087–1095.

Idris 2000   Idris, N.R.N., Yatim, A.H.M, Reduced Torque Ripple And Constant Torque Switching Frequency Strategy For Direct Torque Control of Induction Machine, Applied Power Electronics Conference and Exposition, APEC 2000, Fifteenth Annual IEEE, Vol. 1, 2000, pp. 154–161.

IEC 61800-4:2002   IEC 61800-4, Adjustable speed electrical power drive systems – Part 4: General requirements – Rating specifications for a.c. power drive systems above 1000 V a.c. and not exceeding 35 kV, 1st edition, 2002-09, 2002, 219 p., pp.73.

Ikäheimo 2002   Ikäheimo, J., Permanent magnet motors eliminate gearboxes, ABB Review, No. 4, 2002, pp. 22–25.

Jahns 1996   Jahns, T. M., Soong, W.L., Pulsating Torque Minimization Techniques for Permanent Magnet AC Motor Drives–A Review, IEEE Transactions on Industrial Electronics, Vol. 43., No. 2., April 1996, pp. 321–330.

Ji 1995   Ji, J.-K., Sul, S.-K., Kalman Filter and LQ Based Speed Controller for Torsional Vibration Suppression in a 2-Mass Motor Drive System, IEEE Transactions on Industrial Electronics, Vol. 42, No. 6, December 1995, pp. 564–571.

Kaukonen 1999   Kaukonen, J., Salient pole synchronous machine modelling in an industrial direct torque controlled drive application, Dissertation, Lappeenranta, Finland, 1999, 138 p., pp. 30–32.

Kerkman 1997   Kerkman, R.J., Leggate, D., Skibinski, G.L., Interaction of drive modulation and cable parameters on ac motor transients, IEEE Transactions on Industry Applications, Vol. 33, No. 3, May/June 1997, pp. 722–731.

Kerkman 2003   Kerkman, R.J., Leggate, D., Schlegel, D.W., Winterhalter, C., Effects of Parasitics on the Control of Voltage Source Inverters, IEEE Transactions on Power Electronics, Vol. 18, No. 1, January 2003, pp. 140–150.

Kim 2003   Kim, H.-S., Youn, M.-J., A New On-line feed-forward dead-time compensation for PM synchronous motor drive, Proceedings of the EPE 2003, 10th European Conference on Power Electronics and Applications, Toulouse, Sept. 2003, 10 p.

Kurronen 2003   Kurronen, P., Torque vibration model of axial-flux surface-mounted permanent magnet synchronous machine, Dissertation, Lappeenranta, Finland, 2003, 123 p.

Lam 2001   Lam, B. H., Panda, S. K., Xu, J. X., Periodic Torque Ripples Minimisation in Permanent Magnet Synchronous Motor Drives using Iterative Learning control, Proceedings of the EPE 2001, Graz, 2001, 12 p.

Laurila 2002a   Laurila, L., Kurronen, P., Niemelä, M. and Pyrhönen, J., Effect of unideal current sensors in direct torque controlled PMSM drives, NORPIE/2002, Nordic Workshop on Power and Industrial Electronics, Aug. 2002, 5 p.

Laurila 2002b   Laurila, L., Sarén, H., Pyrhönen, J., Converter unidealities causing torque ripple in direct torque controlled PMSM drives, ICEM 2002, 15th International Conference on Electrical Machines, Conference Record, Aug. 2002, 5 p.

Laurila 2003   Laurila, L., Pyrhönen, J., Niemelä, M., Torque ripple in DTC PMSM drives due to nonlinearity of current sensors, Proceedings of the EPE 2003, 10th European Conference on Power Electronics and Applications, Toulouse, Sept. 2003, 10 p.

Leggate 1998   Leggate, D., Pankau, J., Schlegel, D., Kerkman, R., Skibinski, G., Reflected waves and their associated current, IEEE IAS Conference Proceedings, St Louis, MO, Oct. 1998, pp. 789–798.

LEM 1998   LEM, Data sheet of the closed loop current transducer LA 55-P, http://www.lemusa.com/lem/LEMPROD.NSF/e1df2b7567b3a6bc862565d8 0054eb73/72ace25be0aa754f8625658e00618b41/$FILE/E132500S.pdf, [cited 14 April 2004], Available from LEM USA, INC., Milwaukee (Wisconsin), 1998.

Li 1997   Li, Y., Shao, J., Si, B., Direct torque control of induction motor for low speed drives considering discrete effects of control and dead-time of inverter. Conference Record of the Thirty-Second IAS Annual Meeting, Industry Applications Conference, IAS '97, Vol. 1, 1997, pp. 781–788.

Locci 2001   Locci, N., Muscas, C., Comparative Analysis Between Active and Passive Current Transducers in Sinusoidal and Distorted Conditions, IEEE Transactions on Instrumentation and Measurement, Vol. 50, No. 1, Feb. 2001, pp. 123–128.

Luukko 1998   Luukko, J. and Pyrhönen, J., Selection of the flux linkage reference in a direct torque controlled permanent magnet synchronous motor drive, Proceedings of the 5th International Workshop on Advanced Motion Control, AMC '98-Coimbra, 1998, pp. 198–203.

Merril 1994a   Merrill, E.F., Dynamics of AC Electrical Machines, IEEE Transactions on Industry Applications, Vol. 30, No. 2., March/April 1994, pp. 277–285.

Merril 1994b   Merrill, E.F., Torsional dynamics of AC electrical machines & systems, Pulp and Paper Industry Technical Conference, Conference Record of 1994 Annual, June 1994, pp. 52–59.

Mohan 1995	Mohan, N., Undeland, T.M., Robbins, W. P., Power Electronics – Converters, Applications, and Design, Second edition, John Wiley & Sons, 1995, 802 p., pp. 415–417.
Murai 1987	Murai, Y., Watanabe, T., Iwasaki, H., Waveform Distortion and Correction Circuit for PWM Inverters with Switching Lag-Times, IEEE Transactions on Industry Applications, Vol. IA-23, No. 5, Sept./Oct. 1987, pp. 881–886.
Monti 1998	Monti, A., Pironi, F., Sartogo, F., Vas, P., A new state observer for sensorless DTC control, Power Electronics and Variable Speed Drives, Sept. 1998, Conference Publication No. 456, pp. 311–317.
Naitoh 1996	Naitoh, H., Suzuki, K., Compensation of a GTO-NPC inverter for the damping of rolling mill torsional vibration by ETC (estimated torque feedback control), Power Electronics Specialists Conference, PESC '96 Record., 27th Annual IEEE, Volume: 1, June 1996, pp. 925–930.
Niemelä 1999	Niemelä, M., Position sensorless electrically excited synchronous motor drive for industrial use based on direct flux linkage and torque control, Dissertation, Lappeenranta, Finland, 1999, 142 p., pp. 92.
Norton 1989	Norton, H.N., Handbook of Transducers, Prentice Hall, 1989, 554 p., pp. 519.
Pankau 1999	Pankau, J., Leggate, D., Schlegel, D., Kerkman, R., Skibiniski, G., High frequency modeling of current sensors, Applied Power Electronics Conference and Exposition, 1999. APEC '99. Fourteenth, Annual, Volume: 2, March 1999, pp. 788–794.
Persson 1992	Persson, E., Transient Effects in Application of PWM Inverters to Induction Motors, IEEE Transactions on Industry Applications, Vol. 28, No. 5, September/October 1992, pp. 1095–1101.
Persson 2002	Persson, E., Motor current measurement using time-modulated signals, Power Conversion Conference, 2002. PCC Osaka 2002. Proceedings of the, Vol. 2, 2-5 April, 2002, pp. 716–720
Popović 1991	Popović, R.S., Hall Effect Devices, Magnetic Sensors and Characterization of Semiconductors, Adam Hilger, 1991, 307 p.
Schott 1997	Schott, C., Blanchard, H., Popović, R.S., Racz, R., Hrejsa, J., High-Accuracy Analog Hall Probe, IEEE Transactions on Instrumentation and Measurement, Vol. 46, No. 2, April 1997, pp. 613–616.
Sheppard 1988	Sheppard, D.J., Torsional Vibration Resulting from Adjustable-Frequency AC Drives, IEEE Transactions on Industry Applications, Vol. 24, No. 5., September/October 1988, pp. 812–817.

Shur 1990   Shur, M., Physics of Semiconductor Devices, Prentice-Hall, 1990, 680 p., pp. 628.

Song 2000   Song, S.-H., Choi, J.-W., Sul, S.-K., Current Measurements in Digitally Controlled AC Drives, IEEE Industry Applications Magazine, July/August 2000, pp. 51–62.

Sopanen 2003   Sopanen, J., Hirvonen, M., Laurila, L., Coupled Electro-Mechanical Analysis of a Double Cardan Shaft Driven by a Direct Torque Controlled PMSM, Research Report, Lappeenranta University of Technology, Nov. 2003, 20 p.

Tarkiainen 1999 Tarkiainen, A., Sähkökäyttöjen kaapelivärähtelyt, diplomityö, Lappeenrannan teknillinen korkeakoulu, 1999, 72 p. (In Finnish).

Tiainen 2003   Tiainen, T., Sähkökäyttöryhmien suorituskyvyn kartoitus paperitehtaassa, diplomityö, Lappeenrannan teknillinen yliopisto, 2003, 49 p., pp. 12. (In Finnish).

Vas 1992   Vas, P., Electrical machines and drives. A space-vector theory approach, Oxford University Press, 1992, 808 p.

Vas 1998   Vas, P., Sensorless vector and direct torque control, Oxford University Press, 1998, 729 p.

Waltzer 2002   Waltzer, I., Technological trends in large permanent magnet motor applications, ICEM 2002, 15th International Conference on Electrical Machines, Conference Record, Aug. 2002, 6 p.

Xu 2000   Xu, L., Zhu, Z.Q., Howe, D., Acoustic noise radiated from direct torque controlled induction motor drives. IEE Proc.-Electr. Power Appl. Vol. 147, No. 6, Nov. 2000, pp. 491–496.

Zeng 2001   Zeng, P.W., Torsional Resonance Analysis in Air Handling Units, Sound and Vibration, May 2001, pp. 18–21.

APPENDIX A. DYNAMIC EQUATIONS OF THE TWO-MASS SYSTEM

The dynamic equations of the two-mass system shown in Fig. 1.2 are

$$\omega_{\mathrm{M}} = \frac{1}{J_{\mathrm{M}}} \int T_{\mathrm{e}} - T_{\mathrm{sh}} \, \mathrm{d}t \,, \tag{A.1}$$

$$\omega_{\mathrm{L}} = \frac{1}{J_{\mathrm{L}}} \int T_{\mathrm{sh}} - T_{\mathrm{e}} \, \mathrm{d}t \,, \tag{A.2}$$

$$T_{\mathrm{sh}} = K_{\mathrm{sh}} \int \omega_{\mathrm{M}} - \omega_{\mathrm{L}} \, \mathrm{d}t \,, \tag{A.3}$$

where T_{e} is the motor torque, J_{M} is the motor inertia, ω_{M} is the motor angular speed, T_{sh} is the shaft torque, K_{sh} is the spring coefficient (stiffness), J_{L} is the load inertia, ω_{L} is the load speed and T_{L} is the load torque. Damping due to the friction is assumed to be zero.

APPENDIX B. CO-ORDINATE TRANSFORMATIONS

B.1 Stator and rotor reference frames

The vector diagram of a permanent magnet synchronous motor in stator (xy) and rotor (dq) reference frames is presented in Fig. B.1.
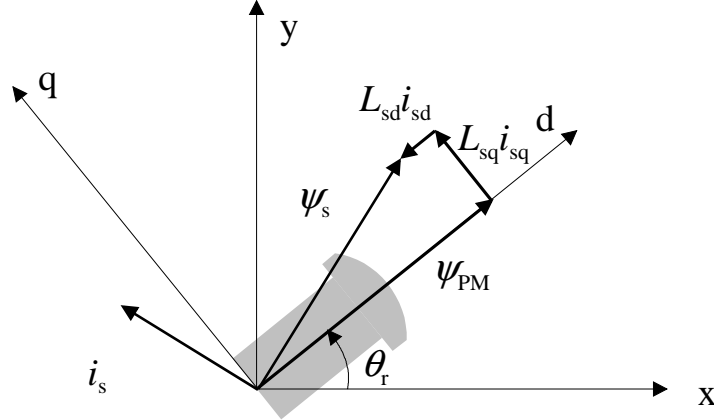

Figure B.1   Stator (xy) and rotor (dq) reference frames of permanent magnet synchronous motor. ψ_s is the stator flux linkage, i_s is the stator current, i_{sd} and i_{sq} are the stator currents in rotor reference frame, L_{sd} and L_{sq} are the direct and quadrature axis stator inductances and ψ_{PM} is the constant flux linkage produced by the permanent magnets and θ_r is the rotor angle.

B.2 Co-ordinate transformations of current vector

The measured stator current vector $\boldsymbol{i}_s$ is determined in the stator reference frame as

$$\boldsymbol{i}_s = \frac{2}{3}\left(i_a e^{j0} + i_b e^{j\frac{2\pi}{3}} + i_c e^{j\frac{4\pi}{3}} \right) . \tag{B.1}$$

When necessary, this current vector may be transformed to the rotor reference frame by multiplying with the co-ordinate system angle difference, Fig B.1.

The current in rotor reference frame is

$$\boldsymbol{i}^r = \left|\boldsymbol{i}\right| e^{j\gamma} \tag{B.2}$$

where γ is the angle between the current vector and d-axis.

The current in the stator reference frame is

$$i^{\text{s}} = |i| e^{j(\gamma + \theta_{\text{r}})} = i^{\text{r}} e^{j\theta_{\text{r}}}$$

(B.3)
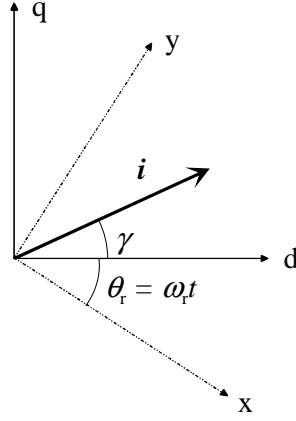
where θ_{r} is the angle between d- and x-axis.

Figure B.2 Current vector i in stator (xy-) and rotor (dq-) co-ordinates.

The co-ordinate transformation of the current vector is thus:

- from the rotor reference frame to the stator reference frame

$$i^{\text{s}} = i^{\text{r}} e^{j\theta_{\text{r}}} \text{ , and}$$

(B.4)

- from the stator reference frame to the rotor reference frame

$$i^{\text{s}} e^{-j\theta_{\text{r}}} = i^{\text{r}} e^{j\theta_{\text{r}}} e^{-j\theta_{\text{r}}} = i^{\text{r}} ,$$

(B.5)

$$i^{\text{r}} = i^{\text{s}} e^{-j\theta_{\text{r}}} .$$

(B.6)

APPENDIX C. CURRENT RIPPLE WAVEFORMS OF TWO AND THREE PHASE MEASUREMENTS

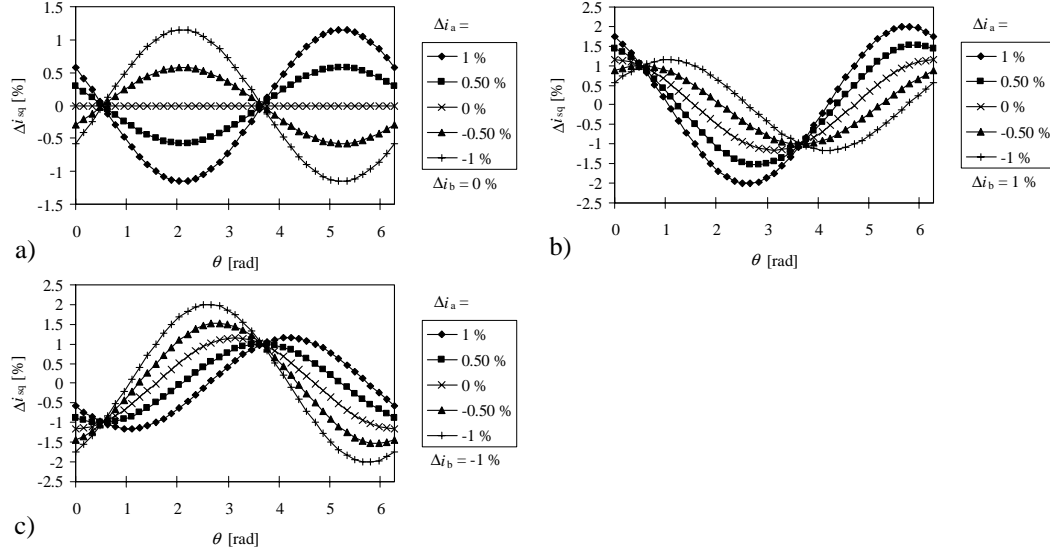## C.1 Two phase current measurement - offset error

Figure C.1 Current ripple waveforms of stator current's quadrature axis component Δi_{sq} due to various offset errors Δi_a and Δi_b in the two measured phase currents.
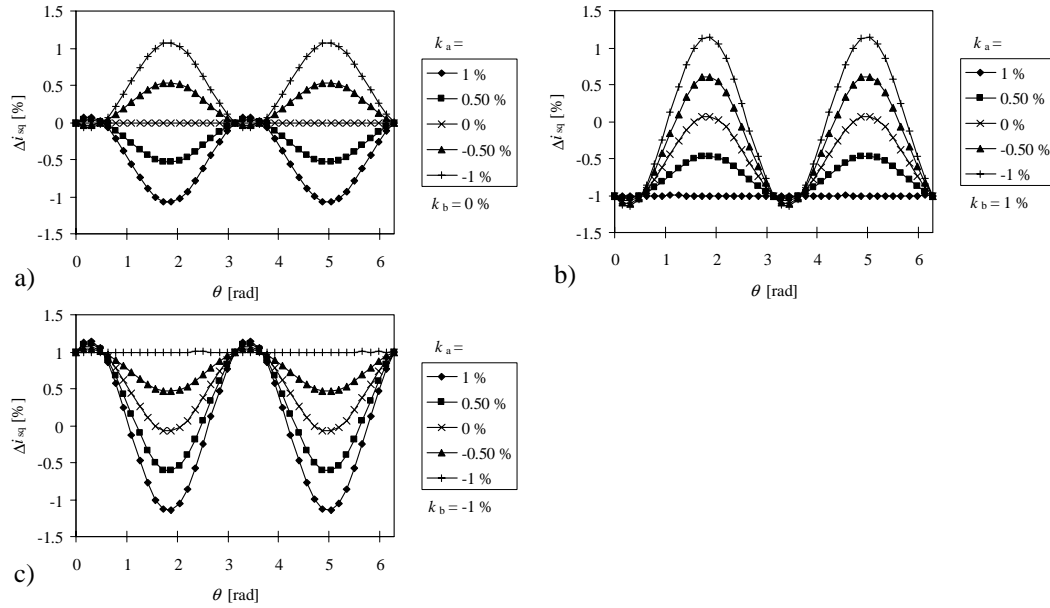
C.2 Two phase current measurement - gain error

Figure C.2 Current ripple waveforms of stator current's quadrature axis component Δi_{sq} due to various gain errors k_a and k_b in the two measured phase currents.
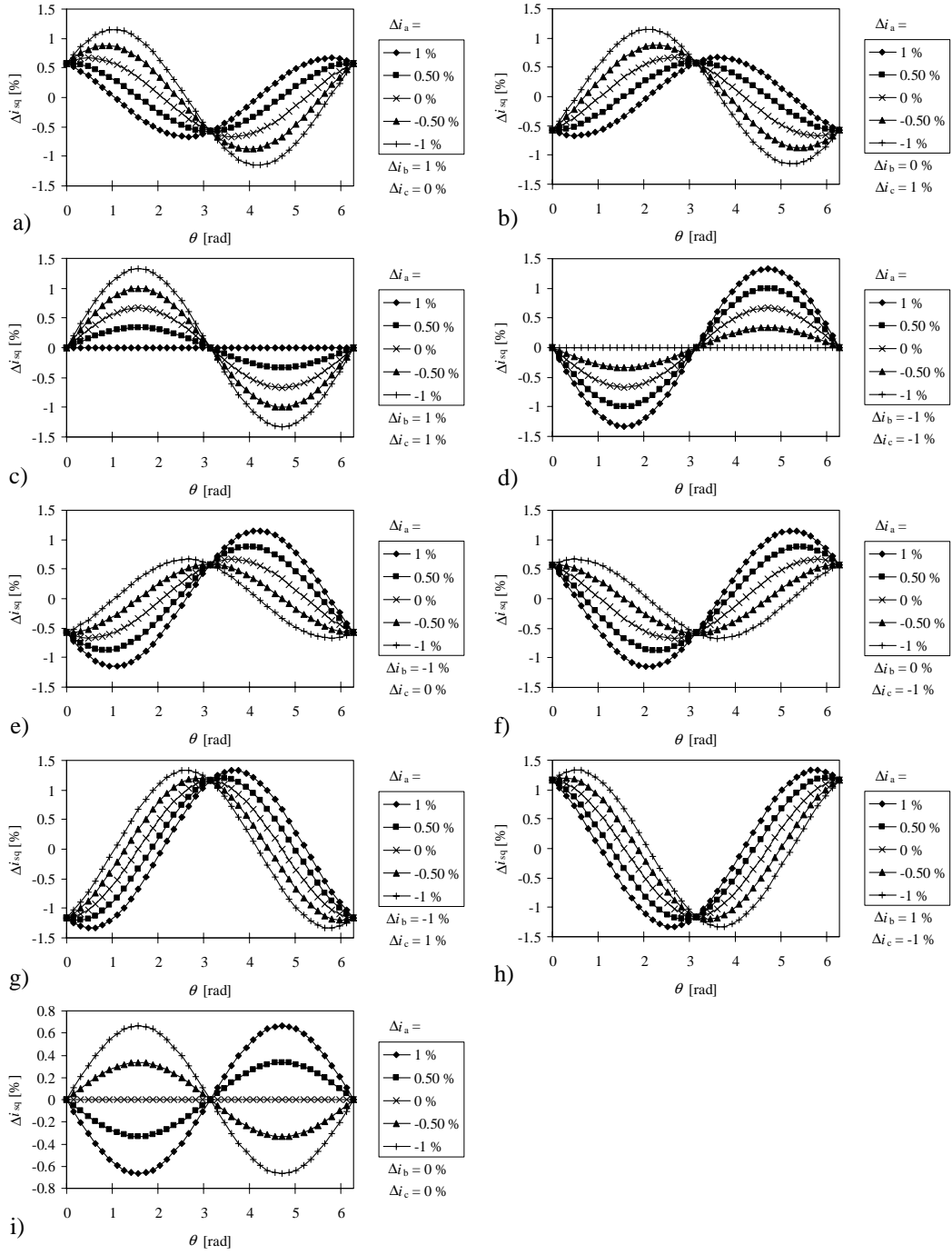
C.3 Three phase current measurement - offset error

Figure C.3   Current ripple waveforms of stator current's quadrature axis component Δi_{sq} due to various offset errors Δi_{a}, Δi_{b} and Δi_{c} in the three measured phase currents.
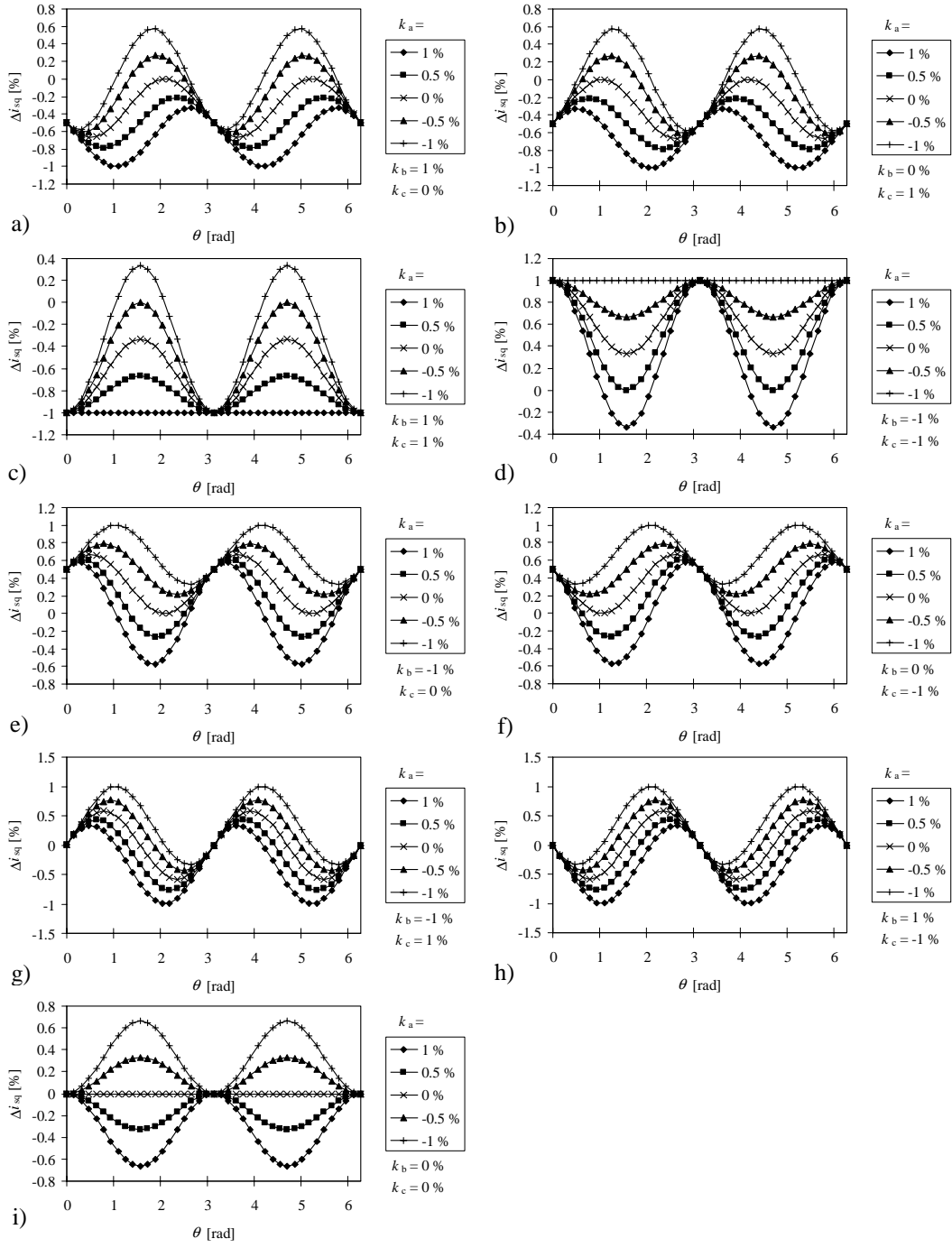
C.4 Three phase current measurement - gain error

Figure C.4 Current ripple waveforms of stator current's quadrature axis component Δi_{sq} due to various gain errors k_a, k_b and k_c in the three measured phase currents.

APPENDIX D. SIMULATION DATA

D. 1 Current measurement non-linearity waveform data

The simulations on current measurement non-linearity in different cases 1-4 were performed with the current vector data given below (extract from a matlab m-file).

% Case 1, current waveform non-linearity
I_vector=[-20 -19 -15 -10 -5 -1 -0.5 0 0.5 1 5 10 15 19 20]; % Actual current
Im_vector=[-20*0.999 -19*0.998 -15*0.997 -10*0.99 -5*0.997 -1*0.998 -0.5*0.999 0 0.5*0.999 1*0.998 5*0.997 10*0.99 15*0.997 19*0.998 20*0.999]; % Measured current

% Case 2, current waveform non-linearity
I_vector=[-20 -19 -15 -10 -5 -1 -0.5 0 0.5 1 5 10 15 19 20];
Im_vector=[-20*1.001 -19*1.002 -15*1.003 -10*1.01 -5*1.003 -1*1.002 -0.5*1.001 0 0.5*0.999 1*0.998 5*0.997 10*0.99 15*0.997 19*0.998 20*0.999];

% Case 3, current waveform non-linearity
I=20;
I_vector=[-20 -19 -15 -10 -5 -1   0   1 5 10 15 19 20];
Im_vector_pos=[-20 -19+0.001*I -15+0.001*I -10+0.001*I -5+0.005*I -1+0.01*I 0.2 1+0.01*I 5+0.005*I 10+0.001*I 15+0.001*I 19+0.001*I 20];
Im_vector_neg=[-20 -19-0.001*I -15-0.001*I -10-0.001*I -5-0.005*I -1-0.01*I -0.2 1-0.01*I 5-0.005*I 10-0.001*I 15-0.001*I 19-0.001*I 20];

% Case 4, current waveform non-linearity
I=20;
I_vector=[-20 -19 -15 -10 -5 -1   0   1 5 10 15 19 20];
Im_vector_pos=[-20+0.001*I -19+0.001*I -15+0.001*I -10+0.001*I -5+0.001*I -1+0.001*I 0.001*I 1+0.001*I 5+0.001*I 10+0.001*I 15+0.001*I 19+0.001*I 20+0.001*I];
 Im_vector_neg=[-20-0.001*I -19-0.001*I -15-0.001*I -10-0.001*I -5-0.001*I -1-0.001*I -0.001*I 1-0.001*I 5-0.001*I 10-0.001*I 15-0.001*I 19-0.001*I 20-0.001*I];

APPENDIX E. DATA OF THE EXPERIMENTAL SETUPS

E.1 Data of the motors used in the experiments

Table E.1 Data of the motor applied in the experimental setup 1.

Nominal power	7 kW
Nominal voltage	400 V
Nominal current	17 A
Nominal frequency	16.7 Hz
Number of polepairs	10
Nominal torque	700 Nm
Direct axis inductance	46 mH
Quadrature axis inductance	46 mH
Stator resistance	1.6 Ω

Table E.2 Data of the motor applied in the experimental setup 2.

Nominal power	5 kW
No-load back EMF	425 V
Nominal current	8 A
Nominal frequency	50 Hz
Number of polepairs	10
Nominal torque	157 Nm
Direct axis inductance	48.7 mH
Quadrature axis inductance	75.8 mH
Stator resistance	1 Ω